Doklady Physics, Vol. 47, No. 3, 2002, pp. 173–175. Translated from Doklady Akademii Nauk, Vol. 383, No. 1, 2002, pp. 34–36.

PHYSICS

Chaplygin Equations and an Infinite Set of Uniformly Divergent Gas-Dynamics Equations

A. I. Rylov

Presented by Academician G.G. Chernyĭ September 19, 2001

Received September 24, 2001

1. We consider two-dimensional potential ideal-gas flows. At the hodograph plane, they are described by the Chaplygin equations

$$\varphi_z + k\psi_\theta = 0, \quad \varphi_\theta - \psi_z = 0 \tag{1}$$

or the Chaplygin equations of the second order for the stream function [1–4]:

$$k\psi_{\theta\theta} + \psi_{zz} = 0, \quad z = \int \frac{\rho}{q} dq, \quad k = \frac{1 - M^2}{\rho^2}. \tag{2}$$

Hereafter, φ is the potential; ψ is the stream function; q, θ, u, and v are the modulus, angle of inclination, and horizontal and vertical components of the velocity vector, respectively; M is the Mach number; p is pressure; and ρ is the density.

Eqs. (1) and (2) have an infinite set of exact solutions [1–4]. In this paper, we show that each solution is associated with a proper set of gas-dynamics equations, one of them being divergent (see Theorem 1). Our detailed analysis of the solutions to system (1), which are found by the method of separation of variables led to one more algorithm for constructing an infinite set of conservation laws (see Theorem 2). The set constructed includes, as a particular case, the set of the conservation laws found in [5, 6]. They can be applied to two-dimensional steady flows (mass, momentum, and angular-momentum conservation laws). It is worth noting that a finite set of the conservation laws was found in [5, 6] for the cases of both steady and unsteady three-dimensional flows.

Theorem 1. *For each solution* $\varphi = f(z, \theta) \neq \text{const}$ *and* $\psi = g(z, \theta) \neq \text{const}$ *to Chaplygin equations* (1), *the introduction of variables* α *and* β *dependent on the functions* $f(z, \theta)$ *and* $g(z, \theta)$, *respectively,* $\alpha = f(z, \theta)$ *and* $\beta = g(z, \theta)$ *yields a system of uniformly divergent gas-dynamics equations in the plane of the potentials* (φ *and* ψ) *and, as a result, a conservation law in the physical plane*:

$$k\beta_\varphi + \alpha_\psi = 0, \quad \beta_\psi - \alpha_\varphi = 0; \tag{3}$$

$$(\alpha\rho u + \beta v)_x + (\alpha\rho v - \beta u)_y = (f\rho u + g v)_x + (f\rho v - g u)_x = 0. \tag{4}$$

Remark. The solutions $\varphi = f = \text{const}$ and $\psi = g = \text{const}$ also allow us to obtain certain conservation laws on the (x, y)-plane. For example, substituting either $f = 1$ and $g = 0$ or $f = 0$ and $g = 1$ into (4), we obtain the conservation law for either mass or circulation, respectively.

2. We consider several tentative examples of exact solutions.

A flow with a source (radial motion). In this case, $g = \theta$ and $f = -\int k\, dz = -K(z)$. Then,

$$k\theta_\varphi - K_\psi = 0, \quad \theta_\psi + K_\varphi = 0;$$

$$(K\rho u - \theta v)_x + (K\rho v + \theta u)_y = 0.$$

A flow similar to a potential vortex. In this case, $f = \theta$ and $g = z$. Then,

$$\begin{gathered} kz_\varphi + \theta_\psi = 0, \quad z_\psi - \theta_\varphi = 0, \\ (\theta\rho u + z v)_z + (\theta\rho v - z u)_y = 0. \end{gathered} \tag{5}$$

It is worth noting that system (5) is well known in gas dynamics [4], but irrespectively of the potential-vortex flow.

The solution $\psi = g = \theta z$ and $\varphi = f = \dfrac{\theta^2}{2} - F(z)$, with $F(z) = \int k\, z dz$, leads to the equations

$$k(\theta z)_\varphi + \left(\frac{\theta^2}{2} - F\right)_\psi = 0, \quad (\theta z)_\psi - \left(\frac{\theta^2}{2} - F\right)_\varphi = 0;$$

Sobolev Institute of Mathematics, Siberian Division, Russian Academy of Sciences, pr. Koptyuga 4, Novosibirsk, 630090 Russia

1028-3358/02/4703-0173$22.00

and

$$\left(\left(\frac{\theta^2}{2} - F\right)\rho u + \theta z v\right)_x + \left(\left(\frac{\theta^2}{2} - F\right)\rho v - \theta z u\right)_y = 0.$$

The solution $\varphi = f = -\theta K(z)$ and $\psi = g = \frac{\theta^2}{2} - G(z)$, with $G(z) = \int K(z)dz$, leads to the equations

$$k\left(\frac{\theta^2}{2} - G\right)_\varphi - (\theta K)_\psi = 0, \quad \left(\frac{\theta^2}{2} - G\right)_\psi + (\theta K)_\varphi = 0;$$

and

$$\left(\theta K\rho u - \left(\frac{\theta^2}{2} - G\right)v\right)_x + \left(\theta K\rho v + \left(\frac{\theta^2}{2} - G\right)u\right)_y = 0.$$

It should be noted that the angle θ of inclination of the velocity vector enters into the conservation laws under consideration as both an explicit argument and the argument of the trigonometric functions. Moreover, the two last solutions depend on the variable θ^2. This fact can be used to carry out certain estimates. For example, using the known asymptotic form of the symmetric flow around a body [7] and the conservation law presented above, we can prove that the following relationships are satisfied at an arbitrary streamline over its entire length:

$$\int_{-\infty}^{+\infty} (G(z) - G(z_\infty))qdl = \int_{-\infty}^{+\infty} \frac{\theta^2}{2} qdl > 0.$$

3. In order to construct new systems of equations and conservation laws, we now consider known solutions to Eqs. (1), which are found by the method of separation of variables. The four independent solutions are of the form

$$\begin{aligned} f_1 &= -\frac{1}{\lambda}h_z^{(1)}\cos\lambda\theta, \quad g_1 = h^{(1)}\sin\lambda\theta; \\ f_2 &= \frac{1}{\lambda}h_z^{(1)}\sin\lambda\theta, \quad g_2 = h^{(1)}\cos\lambda\theta; \\ f_3 &= -\frac{1}{\lambda}h_z^{(2)}\cos\lambda\theta, \quad g_3 = h^{(2)}\sin\lambda\theta; \\ f_4 &= \frac{1}{\lambda}h_z^{(2)}\sin\lambda\theta, \quad g_4 = h^{(2)}\cos\lambda\theta. \end{aligned} \tag{6}$$

Here, λ is an arbitrary constant, and the functions $h^{(1)}(\lambda; z)$ and $h^{(2)}(\lambda; z)$ are two independent solutions to the ordinary differential equation of the second order: $h_{zz}(z) = \lambda^2 kh(z)$. The subscript z stands for differentiation with respect to z.

Since the solutions depend on the arbitrary constant λ, it is possible to construct an infinite set of the functions (f_i, g_i). Therefore, according to Theorem 1, we can find an infinite set of gas-dynamics equations (3) with the variables ($\alpha = f_i$, $\beta = g_i$) dependent on corresponding functions and an infinite set of conservation laws acquiring the following form:

$$(f_i)_\varphi - (g_i)_\psi = 0,$$
$$(f_i\rho u + g_i v)_x + (f_i\rho v - g_i u)_y = 0.$$

In the general case, the functions $h^{(1)}$ and $h^{(2)}$ are expressed in terms of the hypergeometric functions [1–4]. In the case of $\lambda = 1$, they take the known explicit form:

$$h^{(1)}(1; z) = \frac{1}{q}, \quad h_z^{(1)}(1; z) = -\frac{1}{\rho q},$$

$$h^{(2)}(1; z) = \frac{p}{q}, \quad h_z^{(2)}(1; z) = -\frac{p + \rho q^2}{\rho q}.$$

The functions $h^{(1)}$ correspond to the Ringleb flow [1, 3, 8]. The streamline pattern for the flow corresponding to the function $h^{(2)}$ is very similar to that for the Ringleb flow [1]. We now present the relations that describe such flows, the systems of gas-dynamics equations in the form of Eqs. (3), and the corresponding conservation laws in the physical plane.

Ringleb flow. (a):

$$\varphi = f_1 = \frac{\cos\theta}{\rho q}, \quad \psi = q_1 = \frac{\sin\theta}{q};$$

$$k\left(\frac{\sin\theta}{q}\right)_\varphi + \left(\frac{\cos\theta}{\rho q}\right)_\psi = 0, \quad \left(\frac{\sin\theta}{q}\right)_\psi - \left(\frac{\cos\theta}{\rho q}\right)_\varphi = 0;$$

$$\left(\frac{\cos\theta}{\rho q}\rho u + \frac{\sin\theta}{q}v\right)_x + \left(\frac{\cos\theta}{pq}\rho v - \frac{\sin\theta}{q}u\right)_y = 1_x + 0_y = 0.$$

Ringleb flow. (b):

$$\varphi = f_2 = -\frac{\sin\theta}{\rho q}, \quad \psi = g_2 = \frac{\cos\theta}{q};$$

$$k\left(\frac{\cos\theta}{q}\right)_\varphi - \left(\frac{\sin\theta}{\rho q}\right)_\psi = 0, \quad \left(\frac{\cos\theta}{q}\right)_\psi + \left(\frac{\sin\theta}{p\rho}\right)_\varphi = 0;$$

$$\left(-\frac{\sin\theta}{\rho q}\rho u + \frac{\cos\theta}{q}v\right)_x - \left(\frac{\sin\theta}{\rho q}\rho v + \frac{\cos\theta}{q}u\right)_y = 0_x - 1_y = 0.$$

Modified Ringleb flow. (a):

$$\varphi = f_3 = \frac{p + \rho q^2}{\rho q}\cos\theta, \quad \psi = g_3 = \frac{p}{q}\sin\theta;$$

$$k\left(\frac{p}{q}\sin\theta\right)_\varphi + \left(\frac{p + \rho q^2}{\rho q}\cos\theta\right)_\psi = 0,$$

$$\left(\frac{p}{q}\sin\theta\right)_\psi - \left(\frac{p + \rho q^2}{\rho q}\cos\theta\right)_\varphi = 0;$$

$$(p + \rho u^2)_x + (\rho u v)_y = 0.$$

Modified Ringleb flow. (b):

$$\varphi = f_4 = -\frac{p + \rho q^2}{\rho q}\sin\theta, \quad \psi = g_4 = \frac{p}{q}\cos\theta;$$

$$k\left(\frac{p}{q}\cos\theta\right)_\varphi - \left(\frac{p + \rho q^2}{\rho q}\sin\theta\right)_\psi = 0,$$

$$\left(\frac{p}{q}\cos\theta\right)_\psi + \left(\frac{p + \rho q^2}{\rho q}\sin\theta\right)_\varphi = 0;$$

$$(puv)_x + (p + \rho v^2)_y = 0.$$

The Ringleb flow was comprehensively discussed in the literature [1, 3, 8]. It represents one of a few exact solutions to the problem on a flow with a local supersonic area. However, the Ringleb flow leads to no instructive conservation law in the (x, y)-plane. At the same time, the modified Ringleb flow was only briefly mentioned in the literature [1], not being discussed in detail. However, as was shown above, this is the flow that is associated with the momentum conservation law. Nevertheless, we prove below that a combination of the functions describing the Ringleb flows of both types enters into the known angular-momentum conservation law.

It is evident that Theorem 1 does not exhaust all possible conservation laws, in particular, the angular-momentum conservation law. The following theorem, which to a large extent generalizes the conservation law mentioned above, is of interest.

Theorem 2. *For arbitrary values of* λ*, the following conservation laws hold*:

$$(f_3 R(1, \lambda) + f_4 R(2, \lambda))_\varphi - (g_3 R(1, \lambda) + g_4 R(2, \lambda))_\psi = 0, \quad (7)$$

$$(f_1 R(3, \lambda) + f_2 R(4, \lambda))_\varphi - (g_1 R(3, \lambda) + g_2 R(4, \lambda))_\psi = 0. \quad (8)$$

Here, f_i *and* g_i *are the functions given by Eqs.* (6)*, and the function* $R(i, \lambda)$ *is defined by its derivatives*: $R_\varphi(i, \lambda) = g_i$ *and* $R_\psi(i, \lambda) = f_i$.

Remark. In contrast to Theorem 1, the expressions in the parentheses in (7) and (8) do not satisfy system (1).

Corollary. *For* $\lambda = 1$*, the function R can be written out in the explicit form*

$$R(1, 1) = y, \quad R(2, 1) = x, \quad R(3, 1) = X = \int p dy,$$

$$R(4, 1) = Y = \int p dx,$$

with the integrals taken along streamlines.

In the case of $\lambda = 1$, in the potential plane and the physical plane, conservation law (7) takes the following forms, respectively:

$$\left(\frac{p + \rho q^2}{\rho q}\cos\theta y - \frac{p + \rho q^2}{\rho q}\sin\theta x\right)_\varphi - \left(\frac{p}{q}\sin\theta y + \frac{p}{q}\cos\theta x\right)_\psi = 0,$$

$$((p + \rho u^2)y - \rho u v x)_x + (\rho u v y - (p + p v^2)x)_y = 0.$$

This is simply the angular-momentum conservation law.

For $\lambda = 1$, the functions f and g entering into (7) correspond to the modified Ringleb flow, while the function R corresponds to the Ringleb flow. At the same time, these flows interchange in conservation law (8). As a result, we have

$$\left(\frac{\cos\theta}{\rho q}X - \frac{\sin\theta}{\rho q}Y\right)_\varphi - \left(\frac{\sin\theta}{q}X + \frac{\cos\theta}{q}Y\right)_\psi = 0,$$

$$X_x - Y_y = 0.$$

As is seen, for $\lambda = 1$ in the physical plane, conservation law (8) has an extremely simple form.

ACKNOWLEDGMENTS

This work was supported in part by the Russian Foundation for Basic Research, project no. 01-01-00851.

REFERENCES

1. R. von Mises, *Mathematical Theory of Compressible Fluid Flow* (Acad. Press, New York, 1958; Inostrannaya Literatura, Moscow, 1961).
2. L. I. Sedov, *Plane Problems of Hydrodynamics and Aerodynamics* (Nauka, Moscow, 1966, 2 ed.; Academic Press, New York, 1959).
3. G. G. Chernyĭ, *Gas Dynamics* (Nauka, Moscow, 1988).
4. L. V. Ovsyannikov, *Lectures on Basic Principles of Gas Dynamics* (Nauka, Moscow, 1981).
5. N. Kh. Ibragimov, Dokl. Akad. Nauk SSSR **210**, 1307 (1973).
6. E. D. Terent'ev and Yu. D. Shmyglevskiĭ, Zh. Vych. Mat. Mat. Fiz. **15**, 1535 (1975).
7. A. I. Rylov, Prikl. Mat. Mekh. **63**, 405 (1999).
8. F. Ringleb, Z. Angew. Math. Mech. **20**, 85 (1940).

Translated by V. Chechin

Doklady Physics, Vol. 47, No. 3, 2002, pp. 176–180. Translated from Doklady Akademii Nauk, Vol. 383, No. 2, 2002, pp. 184–188.

PHYSICS

Behavior of the Parameters of the Thermal Surface Decomposition of Polymers near the Temperature Boundary of Thermodynamic Stability

O. F. Shlensky and A. S. Lyapin

Presented by Academician V.V. Osiko September 20, 2001

Received October 11, 2001

The upper temperature phase-state boundary (PSB), below which substances in their condensed state are thermodynamically stable, can be reached by both high-intensity heating and a sharp decrease in pressure (see, e.g., [1–4]). Thermal processes accompanying the decomposition of materials under one-sided heating of their surface layers are of the most interest for practice, in particular, from the standpoint of both the stability of heat-resistant coatings and burning [5]. A new method of contact thermal analysis, described in [6, 7], makes it possible to record the kinetics of thermal decomposition with a duration from several seconds to several tens of microseconds and to determine kinetic parameters in the immediate vicinity of the PSB of materials.

In this study, we propose a mathematical model for describing the results of kinetic investigations and simulating processes at the front of polymer decomposition under high-intensity thermal attacks on surface layers for temperatures up to the PSB.

The position of the PSB is thermodynamically determined from the condition that the second variation of one of the thermodynamic potentials is zero; e.g., $\delta^2 G = 0$, where G is the Gibbs free energy [1]. At the stability boundary, the derivatives $\frac{\partial p}{\partial V}$ and $\frac{\partial \mathrm{T}}{\partial V}$ vanish, and, therefore, the PSB can be calculated from the equation of state. The wide-range equations of state proposed recently in [8, 9] allow accurate calculations of the parameters of both polymers and other materials. Experimental methods enable us to determine the kinetic analogs of the temperatures at the PSB, the attainable superheating temperatures T_l [2–4, 6, 7], which are only slightly (2–5°C) lower than corresponding temperatures on the PSB at a given pressure. Figure 1 shows the simplified block diagram of a setup for contact thermal analysis and signal recording from a photodetector for three linear polymers being examined. These are (*1*) polymethylmethacrylate (PMMA), (*2*) high-density polyethylene (LPP), and (*3*) polyethylene glycol (PEG-40000) with a molecular mass of 40000 amu. The plots clearly demonstrate that the thermal decomposition of the first two polymers is a multistage process that can be treated with allowance for the evaporation of the resulting products of complex chemical composition [11, 12]. To develop a mathematical model for processes occurring at the thermal-decomposition front under intense heating, it is sufficient to determine by recording photodetector signals the thermal-decomposition duration at a certain temperature. In other words, we need to measure the time interval t_d between the first dip (the moment when a sample is set onto a substrate) and the moment when the t_d line becomes horizontal. Figure 2 shows the time t_d in the semilogarithmic scale as a function of the reciprocal absolute temperature attained when testing samples. The lower branches of the plots have a shape close to inclined straight lines and can be described by the Arrhenius equation. The left upper branches are bent upward and asymptotically approach vertical straight lines with abscissas $\frac{1}{T_l}$. This behavior is inconsistent with Arrhenius kinetics.

To describe the experimental results, various modified Arrhenius equations were proposed in [10, 11], whose additional multiplier takes into account the peculiar behavior of systems near the PSB. We use the following equation to obtain this multiplier in the analytical form:

$$k(T) = \exp\left(\frac{T}{T_l}\right)^n B\exp\left(-\frac{E}{RT}\right), \qquad (1)$$

where T_l, E, and B are the problem parameters and the exponent n lies within the range from 3 to 20, depending on the substance properties. Equation (1) for $n = 0$ transforms into the ordinary Arrhenius equation. The preexponential factor is responsible for the accelerated

Mendeleev University of Chemical Technology, Miusskaya pl. 9, Moscow, 125190 Russia

1028-3358/02/4703-0176$22.00

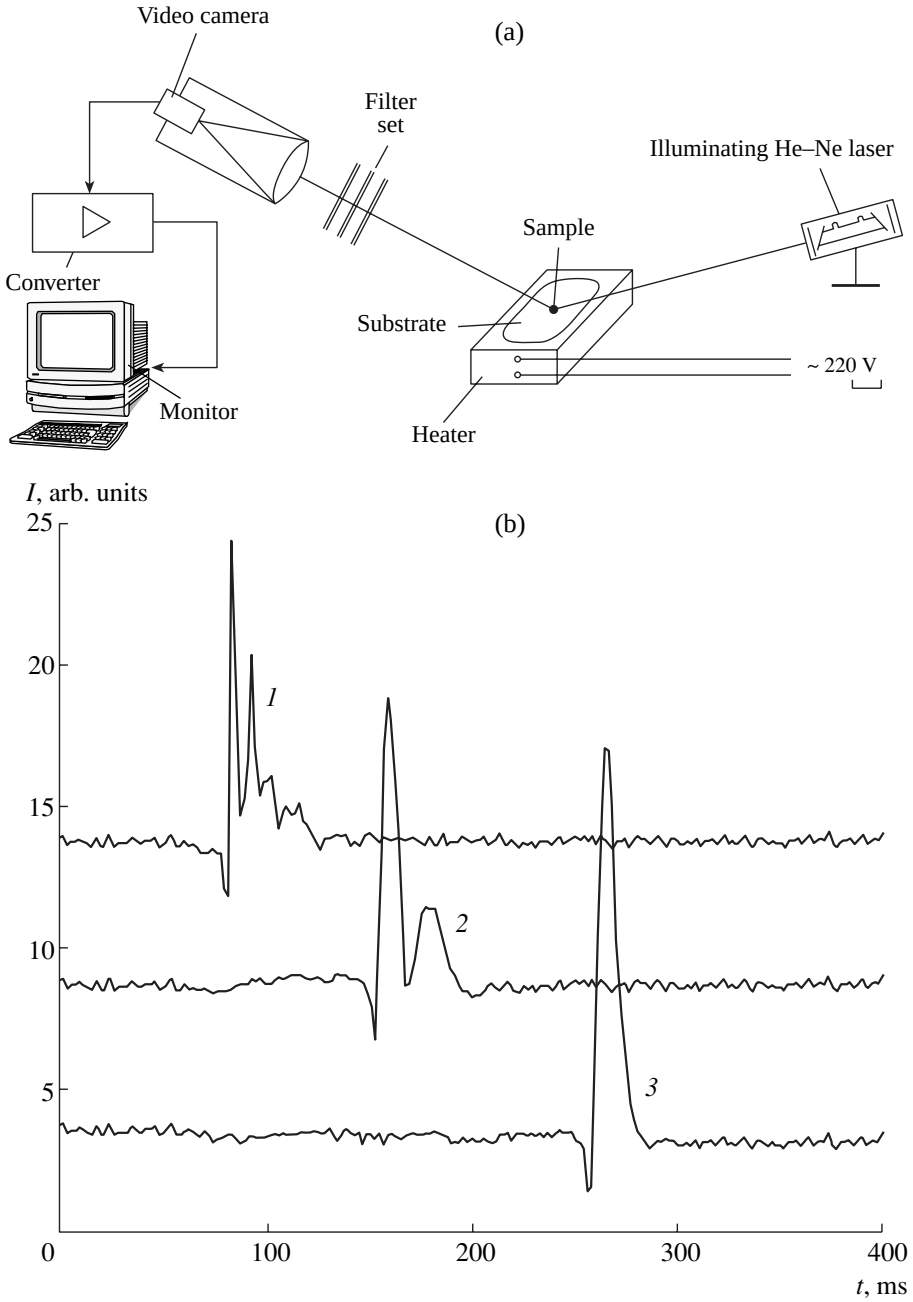

Fig. 1. Determination of the parameters for the upper temperature boundary of thermodynamic stability of polymeric materials: (a) block diagram of the experimental setup; (b) recording signals from a photodetector for (*1*) polymethylmethacrylate, (*2*) low-density polyethylene, and (*3*) polyethylene glycol.

decomposition of polymers due to weakening the intermolecular interaction and the intensification of homogeneous nucleation near the PSB [2–4, 6, 10].

We consider the thermal decomposition of a material half-space, which is described by the heat-conduction equation

$$\frac{d}{dx}\lambda\frac{dT}{dx} - F(T) + \rho C_p u - \frac{dT}{dx} = 0, \qquad (2)$$

where u is the decomposition-front velocity, $F(T)$ is the heat-absorption function usually taken in the form $F(T) = \rho_0 Q k(T)$ [5] under the assumption that thermolysis is a zero-order reaction, Q is the thermal effect of the reaction with the rate constant $k(T)$, and ρ is the density. For these reactions, we have $k(T) = \frac{1}{t_d}$, which allows the use of Eq. (1).

The last term on the left-hand side of Eq. (2) is usually ignored because of its smallness [5]. Integrating Eq. (2) with allowance for the boundary condition

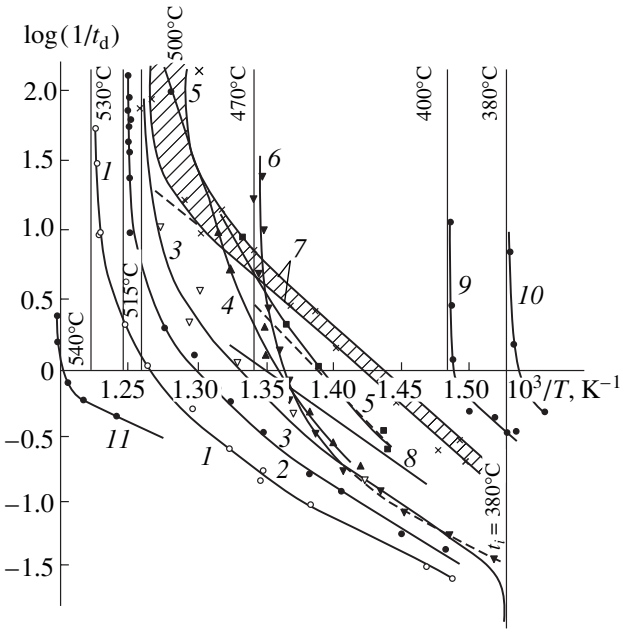

Fig. 2. Results of studying the kinetics of polymer thermal decomposition near the PSB: (*1*) high-impact polystyrene, (*2*) block polystyrene, (*3*) high-density polyethylene, (*4*) lavsan (dacron), (*5*) low-density polyethylene, (*6*) polyvinyl chloride, (*7*) polymethylmethacrylate, (*8*) polycaprolactam, (*9*) polyethylene glycol, (*10*) borax, (*11*) Alaninskoe-deposit oil.

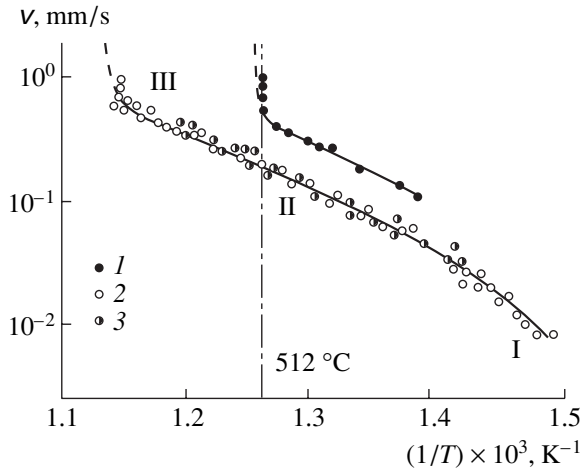

Fig. 3. (*1*, *2*) Decomposition-front velocity and (*3*) burning rate as a function of the reciprocal temperature for (*1*) polymethylmethacrylate and (*2*, *3*) polymethylmethacrylate + triethylene glycol; I–III are regimes of thermal decomposition. Experimental points are obtained by linear pyrolysis, and dashed lines are calculated by Eqs. (5) and (7) with $n = 48$ for heating regimes II and III. For $n = 100$, the dashed lines merge with the vertical dashed-dotted straight line.

$T = T_0$ as $x \longrightarrow \infty$ and taking into account variations of the thermal conductivity $\lambda(T) = \dfrac{\lambda_0 \rho(T)}{\rho_0}$ caused by the appearance of secondary porosity [6], we obtain

$$\frac{dT}{dx} = -D(J(T))^{1/2}. \quad (3)$$

Here, $J(T) = \int_{T_0}^{T} k(T)dT$, $D = \left(\dfrac{2\rho_0 Q}{\lambda_0}\right)^{1/2}$, and ρ_0 and λ_0 are the original values of ρ and λ, respectively.

Furthermore, we equate the heat flow q_w arriving at the surface to the general heat spent for heating and decomposing the material:

$$q_w = -\lambda_w \left(\frac{dT}{dx}\right)_{x=0} = u\rho[C_p(T_w - T_0) + \xi Q], \quad (4)$$

where $\lambda_w = \lambda(T_w) = \chi\lambda_0$, $\chi \simeq \dfrac{\rho(T_w)}{\rho_0}$, and ξ is the fraction of the reacted substance. Substituting the temperature gradient from Eq. (3) into Eq. (4), taking into account Eq. (1), and approximately calculating the integral $J(T_w)$ for $n < 55$ with an accuracy of 5% (see Appendix), we arrive at the equation

$$u = \frac{D\lambda_w \exp(-E/2RT_w)\exp(T_w/T_l)^{n/2}B^{1/2}}{\rho_0[C_p(T_w - T_0) + \xi Q][n(T_w^{n-1}/T_l^n) + E/RT_w^2]}. \quad (5)$$

For $n = 0$ and $T < T_l$, Eq. (5) goes over into the well-known Merzhanov–Dubovitskiĭ formula [12] that describes the linear dependence of $\log u$ on T_w:

$$u_1 = \sqrt{\frac{aRT_w^2 B\exp(-E/RT_w)}{E[(T_w - T_0) + Q/2C_p]}}, \quad (6)$$

where a is the thermal diffusivity, $\lambda_w = \lambda_0$, and $\xi = 1$.

We compare the result obtained with available experimental data. Figure 3 shows the rate of thermal decomposition and gasification of linear PMMA and spatially cross-linked polymers produced by the copolymerization of methyl methacrylate and diethyl ether or triethylene glycol (TEG) in the case of burning and linear pyrolysis. The samples were heated by the linear-pyrolysis method through contacting their end surface with a hot metallic plate containing numerous holes for the removal of pyrolysis products.

The lower sections of the plots (Fig. 3, regime I) correspond to low temperatures at which sample cooling by a surrounding medium affects the result. In region II, experimental data are approximated by an inclined straight line [Eq. (6) and Eq. (5) for $T < T_l$]. In this case, the kinetic parameters determined by solving the inverse problem of nonisothermal kinetics agree well with those obtained by the thermal analysis (see Table 1).

Regime III observed for higher temperatures sharply differs from the two other regimes: the thermal-decomposition rate increases abruptly with a minor rise in temperature. Experimental points deviate upward

from the straight sloping Arrhenius line that corresponds to Eq. (6). At the same time, this deviation completely corresponds to Eq. (5), which includes the PSB parameters. For this case, the maximum temperature of the surface for PMMA samples ($T_w \sim 512$°C) corresponds to data shown in Fig. 2, where the temperature T_l of various PMMA trade marks (shaded region) lies within the range 500 to 515°C [12].

The relation of Eqs. (5) and (6) is descriptively represented as the product

$$u = K(T_w)u_1, \quad (7)$$

where

$$K(T_w) = \frac{\exp(T_w/T_l)^{n/2}}{nRT(T_w/T_l)^n/E + 1}.$$

Introducing the coefficient $K(T_w)$ provides the description of the transition from regime II to regime III and a further increase in the thermal-decomposition rate. According to data of [2–4], the frequency of nucleation rises by two–nine orders of magnitude with an increase in temperature near the PSB by only 1°C. This rise can be described by Eq. (1) with n = 20–100. Table 2 presents the values of $K(T_w)$ for PMMA at E = 43.0 kcal/mol and T_l = 773 K for n = 24 and 48 for various ratios $\frac{T}{T_l}$.

This table demonstrates that the coefficient $K(T_w)$ is close to unity for $T < T_l$, and Eq. (5) approximates the linear section of the plots. The dashed line in Fig. 2 shows an increase in the decomposition-front velocity u according to Eqs. (5) and (7) for n = 24. A similar calculation was performed for other polymers of the spatially cross-linked structure, PMMA + TEG (2 and 10%, respectively).

According to Eq. (3), the highest temperature gradients arise near the heated surface. In particular, the thermal-decomposition depth $l \sim \frac{T - T_0}{\left|\frac{dx}{dT}\right|}$ is equal to 1.3×10^{-3} mm for PMMA at $T_w \approx T_l$ and $\left|\frac{dT}{dx}\right| = 3 \times 10^8$ K/m. For this value of l, Eqs. (5) and (7) are applicable for small polymeric particles, polymer granules, and polymeric drops of various shapes with the characteristic size $L \gg l$. The limitation of an increase in surface temperature (stabilization) with q_w is predicted by Eqs. (4) and (7) and is corroborated in experiments with various methods of thermal supply, e.g., heating by an electric arc, radiant and convective heating, diffusion burning in media enriched in an oxidant, laser-beam action, etc. [5, 11–15].

Thus, we may state that theoretical and experimental studies [10, 12, 13] involving microscopic and macroscopic kinetics of polymer thermal decomposition under one-sided heating allow us to make important conclusions. These studies have demonstrated that heterogeneous nucleation changes to homogeneous nucleation near the PSB with an increase in the heating intensity. The Arrhenius equation traditionally applied for mathematically simulating polymer thermal decomposition does not involve information on the PSB parameters and, therefore, cannot allow for a change in the nucleation mechanism near the PSB. The above-proposed modification of the Arrhenius equation, in contrast to other attempts [10, 11], provides not only numerical calculation of the macroscopic kinetics of thermal-decomposition processes for polymers near the PSB but also analytical description of these processes. In particular, this modification makes it possible to derive the expression for the linear rate and the mass rate of the thermal decomposition with the variation in the parameters near the PSB taken into account. The expression obtained is corroborated by the data of previous experimental studies. The above-proposed relations considerably improve the accuracy of calculations for temperature fields and other characteristics of the thermal decomposition under the highly intense heating of polymeric materials.

Table 1. Kinetic parameters of the polymer thermal decomposition for polymethylmethacrylate (PMMA) and methyl methacrylate–triethylene glycol (MMA + TEG), which are determined by methods of thermal analysis (TA) and linear pyrolysis (LP)

Polymer	E, kcal/mol		$\log B$ [s^{-1}]	
	TA	LP	TA	LP
PMMA	42.6 ± 2	43 ± 3	12.47 ± 0.7	13.32 ± 1
MMA + 2% TEG-3	43.5 ± 2	43 ± 3	12.14 ± 0.7	12.51 ± 1
MMA + 10% TEG-3	43.8 ± 2	43 ± 3	12.3 ± 0.7	12.51 ± 1

Table 2. Values of the $K(T_W)$ coefficient for polymethylmethacrylate (PMMA)

$\frac{T}{T_l}$	$K(T_W)$	
	n = 24	n = 48
0.8	1.066	1.004
0.85	1.133	1.013
0.9	1.289	1.071
0.95	1.552	1.159
1.0	1.995	1.575
1.1	5.042	112.5
1.2	249.6	3.06×10^{30}

Appendix. Calculation of the $J(T)$ integral. We approximately calculate the integral $\int \exp F(x)dx$ by the following method. For a linear function $F(x)$, the integral is exactly calculated as

$$\int \exp F(x)dx = \exp F(x)/F'(x) + \text{const}.$$

This expression is used as the first approximation for integrating the nonlinear function $F(x) = k(T)$ with a certain error Δ, whose upper estimate is

$$\Delta_1 = \frac{B(n(n-1)(T/T_l)^n - 2E/RT)}{n(T/T_l)^n + (E/RT)^2} \times \exp\left(\frac{T}{T_l}\right)^n \exp\left(-\frac{E}{RT}\right).$$

The corresponding expression for the desired integral can be written out in the form

$$J(T) = \frac{BT}{n(T/T_l)^n + E/RT} \exp\left(\frac{T}{T_l}\right)^n \exp\left(-\frac{E}{RT}\right),$$

which is used to calculate the gradient $\frac{dT}{dx}$ and the decomposition-front velocity u.

REFERENCES

1. A. Münster, *Chemische Thermodynamik* (Akademie, Berlin, 1970; Mir, Moscow, 1971).
2. V. P. Skripov, E. N. Sinitsyn, P. A. Pavlov, *et al.*, *Thermal and Physical Properties of Liquids in Metastable State* (Atomizdat, Moscow, 1980).
3. V. P. Skripov, *Metastable Liquid* (Nauka, Moscow, 1972).
4. P. A. Pavlov, *Boiling Dynamics for Highly Superheated Liquids* (Izd. Akad. Nauk SSSR, Sverdlovsk, 1988).
5. Yu. V. Polezhaev and F. B. Yurevich, *Thermal Resistance* (Énergiya, Moscow, 1976).
6. O. F. Shlensky, Dokl. Akad. Nauk **378**, 179 (2001) [Dokl. Phys. **46**, 317 (2001)].
7. O. F. Shlensky, Zh. Fiz. Khim. **75**, 636 (2001).
8. I. V. Lomonosov, V. E. Fortov, and K. V. Khishchenko, Khim. Fiz. **14**, 47 (1995).
9. I. V. Lomonosov, K. V. Khishchenko, V. E. Fortov, and O. F. Shlensky, Dokl. Akad. Nauk **349**, 322 (1996) [Phys. Dokl. **41**, 304 (1996)].
10. O. F. Shlensky, N. V. Afanas'ev, and A. G. Shashkov, *Thermal Decomposition of Materials* (Énergoatomizdat, Moscow, 1996).
11. N. A. Zyrichev and O. F. Shlensky, Khim. Vys. Énerg. **34**, 46 (2000).
12. R. M. Aseeva and G. E. Zaĭkov, *Combustion of Polymeric Materials* (Nauka, Moscow, 1981).
13. A. S. Shteĭnberg, Preprint, IKhF RAN (Inst. of Chemical Physics, Russian Academy of Sciences, 1977).
14. A. G. Gal'chenko, N. A. Khalturinskiĭ, and A. A. Berlin, Vysokomol. Soedin. **22**, 125 (1980).
15. A. V. Butenin and B. Ya. Kagan, Zh. Tekh. Fiz. **49**, 870 (1979).

Translated by R. Tyapaev

Doklady Physics, Vol. 47, No. 3, 2002, pp. 181–183. Translated from Doklady Akademii Nauk, Vol. 383, No. 3, 2002, pp. 322–325.

PHYSICS

Universal Scaling Laws of Transients

A. A. Koronovskiĭ, Corresponding Member of the RAS D. I. Trubetskov, A. E. Khramov, and A. E. Khramova

Received September 25, 2001

The intricate behavior of nonlinear dynamical systems currently attracts the attention of researchers. To a large extent, it is associated with the fundamental problem of studying the laws of dynamical chaos. Systems with discrete time (of mapping) are the simplest nonlinear dynamical systems exhibiting many typical phenomena.

However, there are only a few results on analyzing transients, even though dynamical chaos and scenarios of the order–chaos transition are actively studied. It is generally thought that transients are unessential features of the system dynamics and do not carry any particular information. Stable regimes (periodic, quasiperiodic, chaotic) are a major focus of interest, whereas no consideration is given to transients. When transients are prolonged processes, they may be perceived as obstacles to efficient investigations of the system under consideration. At the same time, the role of transients in nonlinear-system dynamics is of great importance. For a number of dynamical systems (systems under an external impulse action, systems with very prolonged transients, systems with multistability, and distributed oscillatory systems), a transient substantially determines their behavior. Thus, an important class of phenomena was actually disregarded. As will be shown below, a number of scaling laws exist for transients, and processes occurring in a system affect the transient-duration dependence on initial conditions under the variation of controlling parameters.

In this paper, transients in a nonlinear discrete-time dynamical system are analyzed in detail for the first time, and mechanisms complicating the transient-duration dependence on initial conditions are disclosed. Fundamentally new scaling laws typical for transients are found.

We study transients by the example of the classic nonlinear-dynamic model, logistic mapping [1]:

$$x_{n+1} = f(x_n) = \lambda x_n(1 - x_n). \quad (1)$$

The dependence of the transient duration on initial conditions is investigated for various values of the controlling parameter λ in the range from 1.0 to 3.57. In other words, the subharmonic-cascade region is considered [1].

Figure 1 illustrates the dependence of the transient duration for λ values corresponding to cases where a fixed stable point exists in the system. It is seen that the dependence of the transient duration K on the initial conditions x_0 is of a complex "jagged" form. The dependence $K(x_0)$ is regularly complicated as the controlling parameter λ increases.

Global minima in the transient-duration dependence correspond to the initial conditions x_0 coinciding with the points of an attractor that exists in the system phase space for a given value of the controlling parameter λ. In other words, for $\lambda = 1$–3, the global minimum of the transient-duration dependence is attained at the fixed stable point $x^0 = \dfrac{\lambda - 1}{\lambda}$, which is an attractor (Fig. 1). As the parameter λ increases and the fixed point x^0 loses its stability, the global minima of the transient duration initially correspond to the elements of the stable 2-cycle $[\lambda = 3–(1 + \sqrt{6})]$, and then to the elements of the stable cycle with a period of 4, etc.

Since logistic mapping (1) is irreversible, two sequences of points $\{x_i^{(0)}\}\big|_{i=1}^{\infty}$ and $\{x_i^{(1)}\}\big|_{i=1}^{\infty}$ exist for $\lambda = 1$–3.[1] These points are mapped into the fixed stable point x_0 in a finite number of iterations:

$$\begin{aligned} x^0 &= f(x_1^{(0)}) = f(f(x_2^{(0)})) = f(f(x_2^{(1)})) \\ &= \ldots = f^{(n)}(x_n^{(0)}) = f^{(n)}(x_n^{(1)}). \end{aligned} \quad (2)$$

The sequence $\{x_i^{(0)}\}\big|_{i=1}^{\infty}$ converges to the boundary of the attraction pool of the mapping attractor $x = 0$ as

$$x_{i+1}^{(0)} = \frac{x_i^{(0)}}{\lambda}, \quad i \longrightarrow \infty. \quad (3)$$

The sequence $\{x_i^{(1)}\}\big|_{i=1}^{\infty}$ converges to the other bound-

Saratov State University,
ul. Universitetskaya 42, Saratov, 410601 Russia

[1] With the exception of the case $\lambda = 2$ for which $x^0 = 0.5$, the condition $f(x) = x^0$ is satisfied only for $x = x^0$.

1028-3358/02/4703-0181$22.00

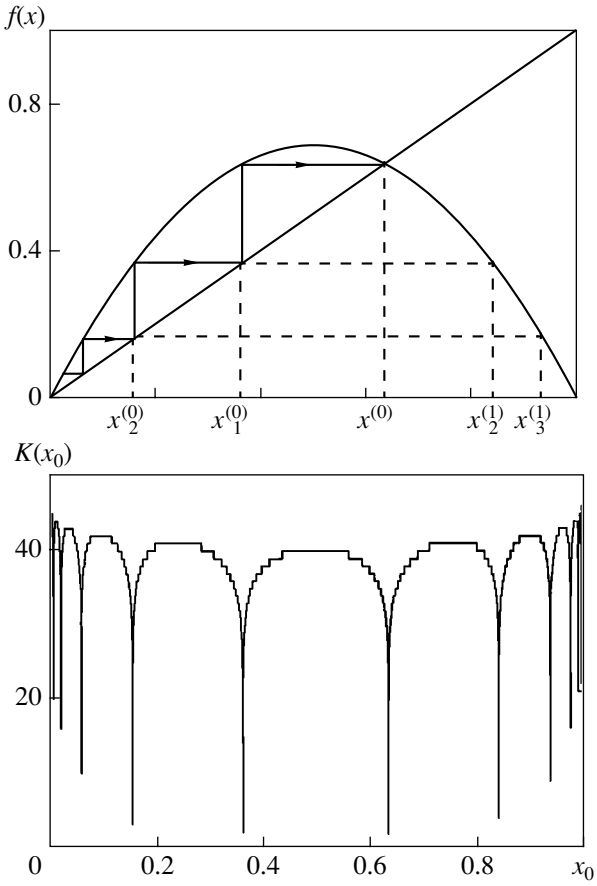

Fig. 1. The Lameray diagram and the transient-duration dependence for the logistic mapping at the controlling parameter λ = 2.75 corresponding to the case where a fixed stable point is realized in the system.

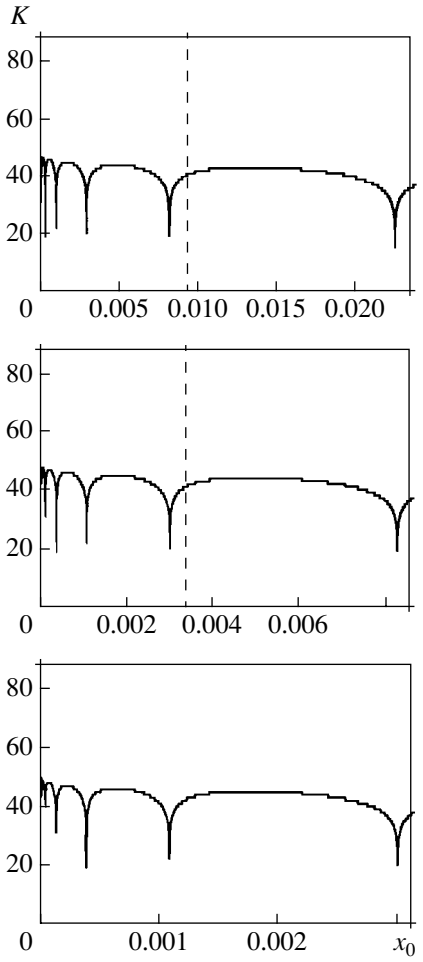

Fig. 2. Scaling for the transient-duration dependence $K(x_0)$ with the scale factor λ with respect to the attraction-pool boundary $x = 0$ of the attractor. The region to the left of the dashed line is exaggerated by a factor of λ. On rescaling, the transient-duration dependence is repeated by shifting to greater values by +1. The results are obtained for the controlling-parameter value λ = 2.75 when a fixed stable point is realized in the system.

ary of the attraction pool of the mapping attractor $x = 1$ as

$$x_{i+1}^{(1)} = 1 - \frac{x_i^{(1)}}{\lambda}, \quad i \longrightarrow \infty. \tag{4}$$

Since the points of the sequences $\{x_i^{(k)}\}\big|_{i=1}^{\infty}$, $k = 0, 1$ are mapped into the fixed stable point x_0 in a finite number of iterations, the minima of the transient durations are also observed at these points (Fig. 1), and $K(x_{i+1}^{(k)}) = K(x_i^{(k)}) + 1$. The maxima of the transient duration behave similarly. Therefore, the dependence of the transient duration K on the initial conditions x_0 in the system under consideration exhibits scaling with the scale factor λ relative to the boundaries $x = 0$ and $x = 1$ of the attraction pool of the attractor (Fig. 2).

As the controlling parameter λ increases, a cascade of period-doubling bifurcations occurs in the system [1], and the dependence of the transient duration K on the initial conditions x_0 is complicated for few reasons. First, unstable cycles appear, and the transient duration is infinite for the initial-condition points x_0 coinciding with the elements of these unstable cycles.[2] Simultaneously, the transient duration is also infinite at the set of points $\{y_i^k\}\big|_{i=1}^{\infty}$, which, by virtue of the irreversibility of mapping (1), are mapped into elements of unstable cycles in a finite number of iterations. Second, the number of sequences $\{x_i^{(k)}\}\big|_{i=1}^{\infty}$ and $\{y_i^k\}\big|_{i=1}^{\infty}$ whose elements are mapped in a finite number of iterations into elements of either stable or unstable cycles increases.[3]

When stable $2n$-cycles, $n = 1, 2, \ldots$, are realized in the system, the transient-duration dependence also

[2] Maxima of the transient durations are of different height and do not turn to infinity in numerical simulation, because the initial conditions x_0 are given with a finite accuracy.

[3] Generally, the number of these sequences is infinite for λ > 3.

exhibits scaling in the vicinity of the attraction-pool boundary points of the attractor. However, after the fixed point x_0 has lost its stability (and a stable cycle with a period of 2 appears), a scaling in the vicinity of this fixed unstable point is observed with the scale factor $\mu = f'(x^0)$, which is a multiplier of this fixed point. To illustrate this behavior, Figure 3 shows the transient-duration dependences near an unstable fixed point for $\lambda = 3.25$.

The existence of the unstable fixed point implies that there are two sequences $\{z_i^{(k)}\}\big|_{i=1}^{\infty}$, $k = 0, 1$, converging from the left and right to the unstable point x_0 as

$$z_{i+1}^{(k)} = x^0 + \frac{z_i^{(k)} - x^0}{\mu}, \quad i \to \infty. \tag{5}$$

A local minimum of the dependence $K(x_0)$ corresponds to every element of the sequences $\{z_i^{(k)}\}\big|_{i=1}^{\infty}$ (Fig. 3). Similar to Eq. (2), every element $z_i^{(k)}$ is mapped into elements of the stable 2-cycle in a finite number of iterations. Moreover, every element of the sequences $\{z_i^{(k)}\}\big|_{i=1}^{\infty}$ generates one or several sequences $\{x_i^{(k)}\}\big|_{i=1}^{\infty}$ converging to the attraction-pool boundary points of the attractors $x = 0$ and $x = 1$. In other words, scaling with respect to the unstable point x_0 is transferred to scaling in the vicinity of the attraction-pool boundaries of the attractor. The exception is the case where the maximum-stability cycle with a period of 2 is realized in the system. In this case, only these two points are mapped into the elements of the stable 2-cycle in a finite number of iterations.

It is apparent that, as the controlling parameter λ increases, similar phenomena will be also observed on the basis of the elements of $2n$-cycles, $n = 0, 1, \ldots$, losing their stability. Thus, the transient-duration dependence $K(x_0)$ is regularly complicated as the parameter λ increases. The elements of unstable $2n$-cycles, which appear due to the cascade of the period-doubling bifurcations, are responsible for this complication.

The scaling of the transient dependence $K(x_0)$ described above is not unique. There is one more type of scaling caused by the behavior of the logistic mapping at the critical point [1]. The renormalization-group analysis [2] demonstrates that the dependences of the duration of transients for maximum-stability cycles exhibit scaling laws with the scaling constants $a = -2.503$ and $b = 2$. When a selected segment is scaled by a factor of a with respect to the point $x = 0.5$ and the transient duration is increased by a factor of b for the $2n$-cycle ($n = 1, 2, \ldots$), the dependence $K(x_0)$ corresponds to the similar dependence for the $(2n - 1)$-cycle.

Thus, in this paper, using a logistic equation as an example, we revealed the reasons complicating the transient-duration dependence on initial conditions when the controlling parameter varies and found universal scaling laws for such a complication.

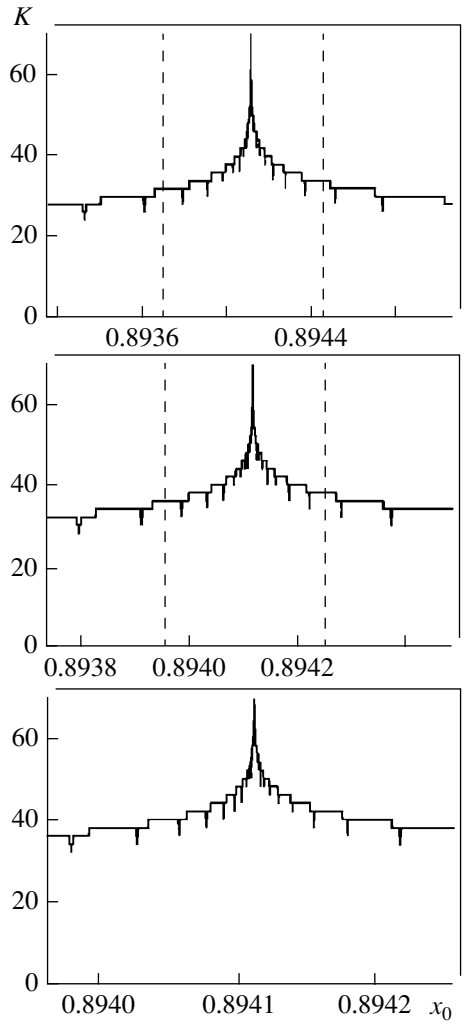

Fig. 3. Scaling in the vicinity of the unstable fixed point x^0 for $\lambda = 3.25$. The region between the dashed lines is exaggerated with the scale factor $\mu = 2.562$. On rescaling, the transient-duration dependence $K(x_0)$ is repeated by shifting to greater values by +1.

ACKNOWLEDGMENTS

This work was supported by the Russian Foundation for Basic Research (project no. 01-02-17392) and by the US Civilian Research and Development Foundation for the Independent States of the Former Soviet Union (grant no. REC-006).

REFERENCES

1. A. P. Kuznetsov and S. P. Kuznetsov, Izv. Vyssh. Uchebn. Zaved. Prikl. Nelin. Dinamika **1**, 15 (1993).
2. M. J. Feigenbaum, J. Stat. Phys. **21**, 669 (1979).

Translated by V. Tsarev

Doklady Physics, Vol. 47, No. 3, 2002, pp. 184–187. Translated from Doklady Akademii Nauk, Vol. 383, No. 3, 2002, pp. 326–329.

PHYSICS

Generalized Sine-Gordon Equation in Wave Dynamics and the Geometry of Surfaces

A. V. Krasnoslobodtsev, G. A. Lyakhov, and N. V. Suyazov

Presented by Academician F.V. Bunkin May 17, 2001

Received May 21, 2001

1. The sine-Gordon (sG) equation

$$\partial_\xi \partial_\eta \Phi = \sin\Phi, \quad (1)$$

where $\xi = x - ct$ and $\eta = x + ct$ are the light-front variables, describes numerous physical phenomena [1–5]. It was first applied in the differential geometry of surfaces with constant negative curvature (see, e.g., [6]). Among other applications, this equation provides a rather general scheme of three-frequency interaction involving a counterrunning wave [7].

2. Equation (1) can be generalized by analyzing four-frequency interaction. When frequencies ω_j and wave numbers k_j satisfy resonance conditions

$$\omega_1 + \omega_2 = \omega_3 + \omega_4, \quad k_1 + k_2 = k_3 + k_4,$$

the wave equation for a field reduces [8] to the set of equations for slow amplitudes a_j. This set consists of four similar equations, the first of which is

$$(\partial_t + c_1\partial_x)a_1 = ia_1\sum_{j=1}^{4} g_{1j}|a_j|^2 + ih_1 a_2^* a_3 a_4, \quad (2)$$

where c_j is the group velocity and h_j and g_{jl} are the nonlinearity coefficients proportional to the components of the cubic susceptibility. Furthermore, we assume that a pair of waves propagates contrary to another pair and that the absolute values of the group velocities are equal to each other, $c_1 = c_3 = -c_2 = -c_4 = c$. In this case, under the physically realizable conditions $g_{1j} = g_{3j}$ and $g_{2j} = g_{4j}$, and under the assumption of the equiphase condition, Eqs. (2) (in the natural normalization to the nonlinearity coefficients and for the real-valued amplitudes A_j) are reduced to the set

$$\partial_\eta A_{1,3} = \pm A_2 A_4 A_{3,1}, \quad \partial_\xi A_{2,4} = \mp A_1 A_3 A_{4,2}. \quad (3)$$

The set of equations (3) has two independent integrals, $A_1^2 + A_3^2 = G^2(\xi)$ and $A_2^2 + A_4^2 = F^2(\eta)$, where $G(\xi)$ and $F(\eta)$ are arbitrary functions. The substitution

$$A_3 + iA_1 = G(\xi)\exp\left(\frac{i\varphi_+}{2}\right),$$

$$A_4 + iA_2 = F(\eta)\exp\left(\frac{i\varphi_-}{2}\right)$$

with the real-valued functions $\varphi_\pm$ reduces Eqs. (3) to the desired set of equations

$$\partial_\pm \varphi_\pm = \sin\varphi_\mp, \quad (4)$$

where $\partial_\pm = \dfrac{\partial}{\partial x_\pm}$ are the operators of differentiation with respect to the new independent variables

$$x_+ = \int d\eta F^2(\eta), \quad x_- = -\int d\xi G^2(\xi).$$

Differentiation of set (4) yields a pair of second-order equations

$$\partial_+\partial_-\varphi_\pm = \sqrt{1 - (\partial_\pm\varphi_\pm)^2}\sin\varphi_\pm. \quad (5)$$

Each of these equations is a peculiar generalization of the sG equation. Indeed, these equations for $(\partial_\pm\varphi_\pm)^2 \ll 1$ (particular linearization) reduce to Eq. (1).

In the three-frequency problem [7], sG equation (1) arises from the set $\partial_+\Phi_+ = \sin\Phi_-$, $\partial_-\Phi_- = \Phi_+$. Therefore, set (4) can be referred to as the symmetric sine-Gordon (SsG) equation. Set (4) was first derived in [9, 10] for the case of the interaction of a pair of counterrunning waves with a standing low-frequency wave.

3. The set of equations (4) has a class of self-similar solutions depending only on the linear combination $S = \lambda x_+ + (-1)^n\lambda^{-1}x_-$ of the variables $x_\pm$, where λ and n are real-valued and integer-valued parameters, respectively. Set (4) reduced for this class of solutions has the integral (Hamiltonian)

$$(-1)^n\lambda\cos\varphi_+ - \lambda^{-1}\cos\varphi_- = H.$$

For $|H| > |H_s|$, where $H_s = \lambda - \lambda^{-1}$, both components $\varphi_\pm$ of a self-similar solution periodically oscillate. For

Institute of General Physics, Russian Academy of Sciences, ul. Vavilova 38, Moscow, 117942 Russia

1028-3358/02/4703-0184$22.00

$|H| < |H_s|$, one component oscillates, whereas the other unboundedly increases.

For $H = (-1)^m H_s$, where m is an integer, the separatrices of above regimes are the solitons

$$\varphi_\pm = (\pm 1)^m \times 2[\arctan(\Lambda C e^S) \pm \arctan(Ce^S)] + \pi\left[\frac{(1 \pm 1)n}{2} + m\right], \quad (6)$$

where $\Lambda = \dfrac{1+\lambda}{1-\lambda}$ and C is a constant. In the limiting case of $\lambda = \pm 1$, solution (6) describes a smooth drop between two constant levels, i.e., a simple π kink. For $\lambda \neq \pm 1$, solution (6) is the superposition of two kinks with the constant relative shift $\Delta S = \ln|\Lambda|$. The sum and difference of two kinks is a two-step kink with a total amplitude of 2π and a pulse, respectively. In the coordinate system (x, t) ($x_\pm = x \pm t$), the amplitude and width of this pulse are determined by the parameter λ and depend on the pulse velocity $v = \dfrac{[\lambda^2 - (-1)^n]^2}{1 - \lambda^4}$. For $\lambda^2 < 1$, the component φ_- has the pulse form. In contrast to Eqs. (4), the classical sine-Gordon equation has only simple-kink self-similar solitons.

4. The sum and difference of the solutions to Eqs. (4),

$$\Phi_\pm = \varphi_+ \pm \varphi_-, \quad (7)$$

satisfy Eq. (1) in the form $\partial_+\partial_-\Phi_\pm = \sin\Phi_\pm$. Therefore, set (4) describing actual phenomena [e.g., those described by Eq. (2)] is a dynamical realization of the formal Bäcklund transformation (BT) relating two solutions to the sG equation (see, e.g., [1, 4]) with the transformation parameter equal to 1. The pairs of solutions to the sG equation do not all generate the solution to set (4) according to Eq. (7). However, the aforementioned relation can be used to construct those exact solutions to set (4) that describe interactions between solitons (6).

To construct these exact solutions, we apply the method that was developed for constructing many-soliton solutions of the classical sine-Gordon equation and is based on the commutativity of Bäcklund transformations. The method consists in constructing closed chains or networks of successive BTs [1, 4]. To obtain solutions to the SsG set, this method should be adapted to Eqs. (4) using chains that end by the Bäcklund transformation with the parameter $\lambda = 1$. In this case, the components of a solution to set (4) are constructed as the half-sum and half-difference [see Eq. (7)] of two solutions to the sG equation related by the above transformation. However, this transformation corresponds to introducing a simple kink to the interaction between solitons [see Eq. (6) as $\lambda \longrightarrow 1$]. In order to obtain general many-soliton solutions to set (4), in particular, without introducing a simple kink, it is necessary to remove this kink from the interaction, shifting the kink to $\pm\infty$. This result is attained by taking 0 or ∞ for the free constant of the first transformation (with $\lambda = 1$) in the chain (i.e., taking the degenerate first transformation). This modified method provides many-soliton solutions of set (4), including solutions describing breather-type solitary waves and their interaction.

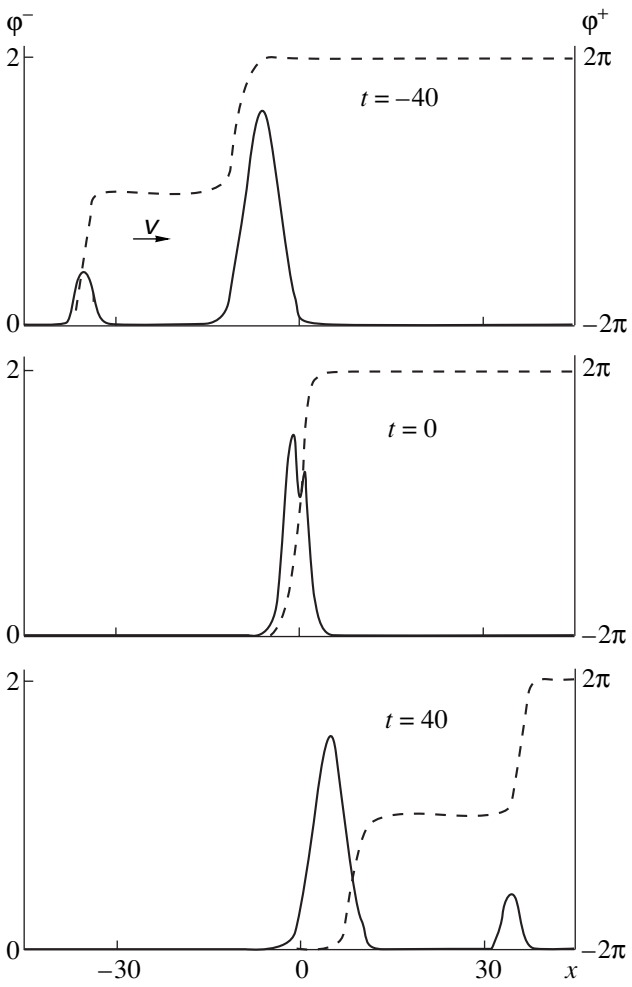

Fig. 1. Interaction between two composed symmetric sine-Gordon solitons (6) for $\lambda_1 = -\frac{1}{5}$, $\lambda_2 = -\frac{5}{7}$, $C = -1$, and $m = n = 0$: the elastic collision of two pulses (φ_-, solid line) and of two double kinks (φ_+, dashed line).

Figure 1 shows an example of the exact solution to set (4). This solution describes a collision of two composite solitons ($\lambda^2 \neq 1$) [see Eqs. (6)]. For the motion in the same direction in the (x, t) coordinate system, each of the components of the solution $\varphi_\pm$ describes interaction between equal-type solitons. Here, one of the components (φ_- when $v > 0$) presents a most interesting case of the interaction between pulse solitons. After interaction, the shape of the solitons is completely recovered.

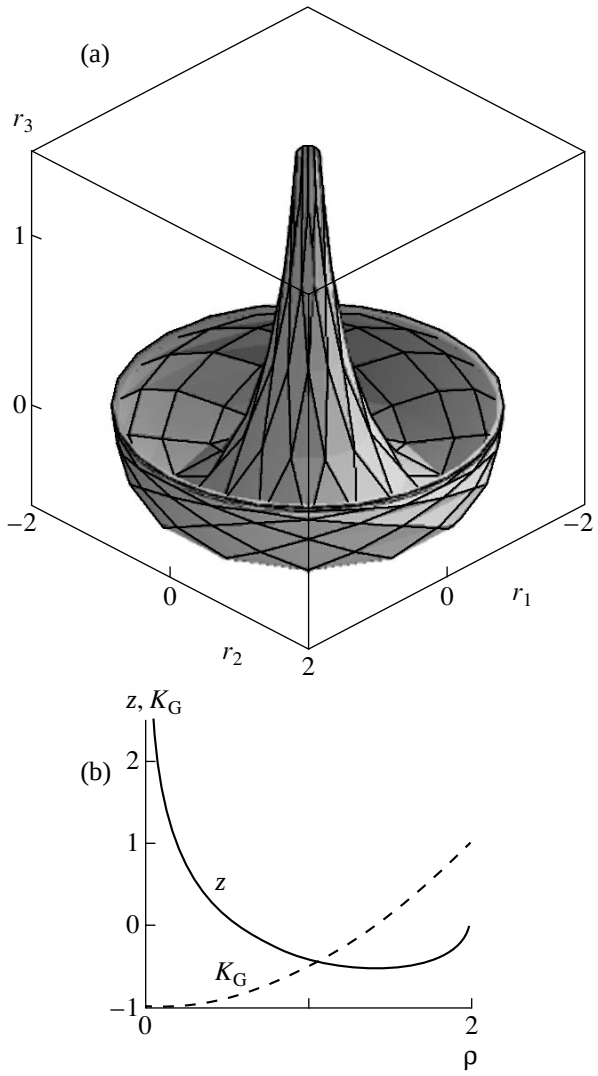

Fig. 2. (a) Surface of revolution (10) (contours $u_{1,2}$ = const are shown) and (b) generatrix $z(\rho)$ (solid line) and curvature K_G (dashed line) as a function of radius ρ.

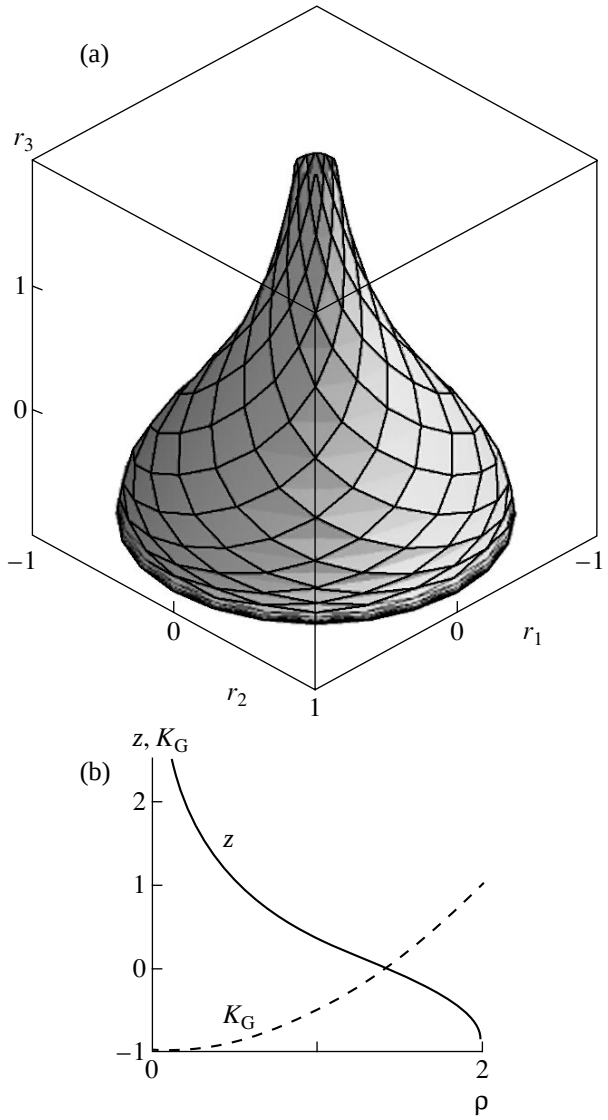

Fig. 3. The same as in Fig. 2 for surface of revolution (11).

5. We now discuss the application of SsG equations in the geometry of surfaces.

Let a surface in the three-dimensional space with Cartesian coordinates $\mathbf{r} = \{r_1, r_2, r_3\}$ be specified by equations $r_k = r_k(u_1, u_2)$, $k = 1, 2, 3$. The Gaussian coordinates (u_1, u_2) of the surface are chosen in such a manner that its metric tensor g_{ij} has the form $g_{11} = g_{22} = 1$ and $g_{12} = g_{21} = \cos\phi$. In this case, the Gaussian curvature of the surface is [11]

$$K_G = -\frac{1}{\sin\phi}\frac{\partial^2\phi}{\partial u_1 \partial u_2}. \quad (8)$$

This equation indicates that the angle ϕ between the contours $u_{1,2}$ = const for a surface of a constant negative curvature $K_G = -1$ is described by the sG equation. An example of such a surface is the Beltrami surface [6].

We now discuss surfaces for which the angle ϕ is determined by Eq. (4) for $x_\pm = u_{1,2}$ and $\varphi_+ = \phi$. It follows from Eqs. (8) and (4) that the curvature $K_G = -\cos\varphi_-$ of these surfaces can vary. We seek a corresponding example among surfaces of revolution,

$$r_1 = \rho\sin\beta, \quad r_2 = \rho\cos\beta, \quad r_3 = z(\rho).$$

In addition, we suppose that the angle ϕ and radius ρ depend only on the sum $\sigma = u_1 + u_2$. Substituting these relations into the definition for g_{ij} yields

$$\beta = b(u_1 - u_2), \quad \rho = b^{-1}\left|\sin\frac{\phi}{2}\right|, \quad b = \text{const}.$$

The generatrix of the surface of revolution, $z(\rho)$, is determined by the equation

$$\left(\frac{dz}{d\rho}\right)^2 = (1 - b^2\rho^2)\left(\frac{d\rho}{d\sigma}\right)^{-2} - 1.$$

To construct a surface corresponding to set (4), we use simple-kink solution (6) for $\lambda = \pm 1$, $\phi = 2\arctan[e^{\pm(u_1+u_2)}]$. In this case, the dependence of the curvature on surface coordinates also has the form of a surface-curvature kink

$$K_G = \pm\tanh(u_1 + u_2) \tag{9}$$

describing a variation in the curvature K_G from 1 to –1.

In order to determine the surface, we should also specify the parameter b. For $b = \frac{1}{2}$, the surface is expressed in elementary functions as

$$\begin{aligned} \rho &= 2[1 + e^{\mp 2\sigma}]^{-1/2}, \\ r_3 &= \operatorname{arcsinh}(e^{\mp\sigma}) - 2[1 + e^{\pm 2\sigma}]^{-1/2} \end{aligned} \tag{10}$$

and is shown in Fig. 2.

For $b = 1$, the generatrix of the surface is specified by the quadrature

$$\begin{aligned} \rho &= [1 + e^{\mp 2\sigma}]^{-1/2}, \\ r_3 &= \mp\int_0^\sigma \frac{\sqrt{(1 + e^{\pm 2s})(1 + e^{\pm 2s} + e^{\pm 4s})}}{(1 + e^{\pm 2s})^2} ds \end{aligned} \tag{11}$$

and is shown in Fig. 3. In the vicinity of $\rho = 1$, both of the curvature radii of surface (11) have almost the same magnitudes and this surface is close to the unit-radius hemisphere. As $\rho \longrightarrow 0$, this surface degenerates to a Beltrami pseudosphere. Thus, kink (9) here describes a variation in the curvature from the region with $K_G \approx 1$, in which the surface is locally spherical, to the region with $K_G \approx -1$, in which the surface behaves as a Beltrami pseudosphere.

The above applications of SsG equations are evidently related to each other. For the four-wave problem described by these equations [see Eqs. (3), (4)] with stationary boundary conditions, the squared amplitudes of the interacting waves are proportional to the functions $1 \pm \cos\varphi_{\pm,\mp}$. Therefore, the squared amplitudes of waves for each solution to set (4) are proportional to the Gaussian curvature of a surface generated by this solution.

ACKNOWLEDGMENTS

This work was supported by the Russian Foundation for Basic Research, project nos. 00-15-99636 and 99-02-16415.

REFERENCES

1. A. Seeger, H. Donth, and A. Kochenforfe, Z. Phys. **134**, 173 (1953).
2. J. K. Perring and T. H. R. Skyrme, Nucl. Phys. **31**, 550 (1962).
3. S. L. McCall and E. L. Hahn, Phys. Rev. **183**, 457 (1969).
4. G. L. Lamb, Rev. Mod. Phys. **43**, 99 (1971).
5. M. J. Ablowitz, D. J. Kaup, A. C. Newell, and H. Segur, Phys. Rev. Lett. **31**, 125 (1973).
6. B. A. Dubrovin, S. P. Novikov, and A. T. Fomenko, *Modern Geometry: Methods and Applications* (Nauka, Moscow, 1986).
7. A. V. Krasnoslobodtsev, G. A. Lyakhov, and N. V. Suyazov, Bull. Rus. Acad. Sci. Physics, Suppl. Phys. of Vibrations **61**, 197 (1997).
8. S. A. Akhmanov and R. V. Khokhlov, *Problems of Nonlinear Optics* (VINITI, Moscow, 1965).
9. K. I. Volyak, G. A. Lyakhov, and I. V. Shugan, Phys. Lett. A **96A**, 53 (1983).
10. K. I. Volyak, G. A. Lyakhov, and I. V. Shugan, Tr. Inst. Obshch. Fiz., Ross. Akad. Nauk **1**, 114 (1986).
11. B. Blyashke, *Einfürung in die Differentialgeometrie* (Springer, Berlin, 1950; Gostekhizdat, Moscow, 1957).

Translated by R. Tyapaev

Doklady Physics, Vol. 47, No. 3, 2002, pp. 188–191. Translated from Doklady Akademii Nauk, Vol. 383, No. 3, 2002, pp. 330–333.

PHYSICS

Enhancement of Energy and *Q*-factor of a Nonlinear Resonator with an Increase in Its Losses

Corresponding Member of the RAS O. V. Rudenko*, A. L. Sobisevich, L. E. Sobisevich**, and C. M. Hedberg*****

Received November 6, 2001

A phenomenon that is paradoxical at first sight is studied: an appropriately-organized energy outflow from a resonator cavity results not in the attenuation of nonlinear vibrations but in their noticeable enhancement.

An increase in the resonator *Q*-factor and in the energy accumulated in it is well pronounced when the frequencies of higher harmonics generated in a nonlinear medium are close to the natural frequencies of the resonator.

An important example of nonlinear systems with the necessary properties is an acoustic resonator with selective losses. First, we consider a conventional resonator whose right boundary $x = L$ is fixed and whose left boundary $x = 0$ oscillates with the velocity

$$u(x = 0, t) = A\sin(\omega_0 t). \quad (1)$$

Here, $\omega_0 = \pi c/L$, where c is the speed of sound. Since the spectrum of the natural frequencies is equidistant, $\omega_n = n\omega_0$ ($n = 2, 3, \ldots$) and a cascade of nonlinear processes takes place in the system, resulting in an effective transfer of energy to the high-frequency region (higher harmonics). In this region, the energy of oscillations is heavily absorbed due to the high-frequency dissipation effects, which are usually related to the viscosity and thermal conductivity of the medium [1]. A standing-wave field formed in the resonator involves shock fronts traveling between the walls [2]. Nonlinear absorption occurring in the narrow region of the front determines the Q_{nl}-factor of the resonator in the strong-oscillation mode. This *Q*-factor is much less than the conventional linear quality Q_{lin} [3]:

$$Q_{nl} = \left(\frac{8c}{\pi\varepsilon A}\right)^{1/2}, \quad Q_{lin} = \frac{c^2\rho}{\pi b\omega_0}. \quad (2)$$

Here, ρ, ε, and b are the density, nonlinearity, and effective viscosity of the medium, respectively [1].

Recall that the quantity Q is the ratio of the characteristic amplitude of field oscillations in the resonator to the amplitude of the oscillations of the boundary.

The necessity of increasing the energy stored in a resonator arises in many applications (see, e.g., [4, 5]). The ways of increasing Q_{nl} were discussed in [6]. One important method based on the introduction of selective losses at the second-harmonic frequency $2\omega_0$ is analyzed below.

The general ideas of controlling the nonlinear interactions by introducing selective losses were reported in [7, 8]. In this case, the absorption at the frequency $2\omega_0$ suppresses the generation of the second harmonic and, therefore, interrupts the cascade of the nonlinear transfer of energy upwards over the spectrum. In practice, losses at the frequency $2\omega_0$ can be realized either by introducing resonant scatterers to the medium (e.g., gas bubbles to a fluid) or by using selective boundaries (e.g., transmitting the frequency $2\omega_0$ and reflecting all other frequencies [9]).

We analyze a nonlinear resonator in an approximate approach. As was shown in [2], an oscillating field between the walls $x = 0$ and $x = L$ can be represented as the superposition of two mutually opposing waves. Each of them can be strongly distorted due to nonlinear self-action, but the contributions of cross interactions are nonresonant and can be neglected [3]. The velocity u of oscillating medium particles in one of the opposing waves obeys the equation [3, 7, 10]:

$$\frac{1}{c}\frac{\partial u}{\partial t} - \frac{\varepsilon}{c^2}u\frac{\partial u}{\partial \tau} - \frac{b}{2c^3\rho}\frac{\partial^2 u}{\partial \tau^2} = \frac{A}{2L}\sin(\omega_0\tau) - \frac{\alpha}{c}b_2(t)\sin(2\omega_0\tau). \quad (3)$$

Here, for definiteness, the wave traveling in the positive x-axis direction is considered; t is the slow time corresponding to the transition to a steady state in the resonator; the fast time τ describes the oscillations; α is the

* *Moscow State University, Vorob'evy gory, Moscow, 119899 Russia*

** *Schmidt Joint Institute of Physics of the Earth, Russian Academy of Sciences, Bol'shaya Gruzinskaya ul. 10, Moscow, 123995 Russia*

*** *Institutionen for Maskinteknik, Karlskrona, 37179 Sweden*

1028-3358/02/4703-0188$22.00

selective-absorption coefficient; and the amplitude of the second harmonic,

$$b_2(t) = \frac{2}{\pi}\int_0^\pi u(t,\tau)\sin(2\omega_0\tau)d(\omega_0\tau), \qquad (4)$$

is not known in advance. Thus, Eq. (3) with Eq. (4) is a nonlinear integro-differential equation [7]. When the right-hand side of Eq. (3) is defined, Eq. (3) goes over into a Burgers-type inhomogeneous equation [11].

For convenience, we use the dimensionless variables

$$V = \frac{u}{u_0}, \quad \theta = \omega_0\tau, \quad T = \frac{t}{t_s}, \qquad (5)$$

where t_s is the characteristic nonlinear time of forming a discontinuity in the wave and u_0 is the characteristic amplitude:

$$t_s = \frac{c}{\varepsilon\omega_0 u_0}, \quad u_0 = \sqrt{\frac{Ac}{2\pi\varepsilon}}. \qquad (6)$$

Equation (3) with Eq. (4) in view of Eqs. (5) and (6) takes the form

$$\frac{\partial V}{\partial T} - V\frac{\partial V}{\partial\theta} - \Gamma\frac{\partial^2 V}{\partial\theta^2} = \sin\theta - D\sin 2\theta\frac{2}{\pi}\int_0^\pi V(T,\theta')\sin 2\theta' d\theta'. \qquad (7)$$

Here, the dimensionless numbers

$$\Gamma = \frac{b\omega_0}{2\varepsilon\rho c u_0} = \frac{t_s}{t_a} \text{ and } D = \frac{\alpha c}{\varepsilon\omega_0 u_0} = \alpha t_s \qquad (8)$$

are the ratios of the nonlinear time t_s to the time of the conventional absorption t_a and to the characteristic time α^{-1} of selective losses, respectively.

To analyze the excitation of forced oscillations in the resonator, Eq. (7) should be solved with the zero initial conditions $V(T = 0, \theta) = 0$. For $T \longrightarrow \infty$, a balance between the energy inflow from the source (oscillating wall) and the losses of three types—viscous, nonlinear, and selective—is achieved. Steady-state oscillations are most easily analyzed. At the same time, steady states, where nonlinearity is most pronounced, are of the most interest. The steady-state solution satisfying the periodical conditions, which reduces to the homogeneous boundary conditions

$$V_{st}(\theta = \pi) = V_{st}(\theta = -\pi) = 0$$

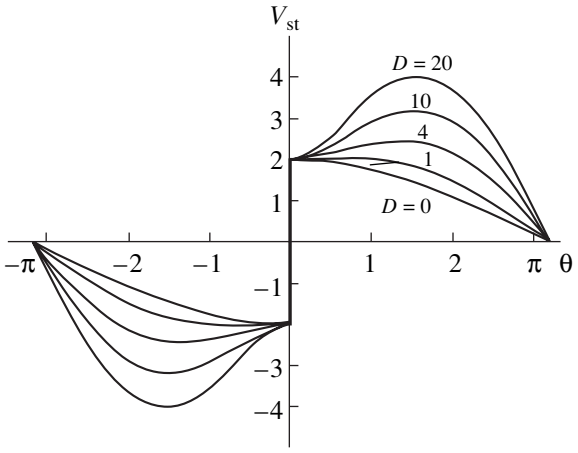

Fig. 1. One-period profiles of oscillations for various values of selective absorption *D*.

when the wall motion is described by Eq. (1), has the form

$$\frac{V_{st}(\theta)}{\sqrt{2}} = \pm(1+\cos\theta)^{1/2} \times\left[1 + D(1-\cos\theta)\frac{2}{\pi}\int_0^\pi V_{st}(\theta')\sin 2\theta' d\theta'\right]^{1/2}. \qquad (9)$$

The signs + and – in solution (9) are taken for the half-periods $0 < \theta \le \pi$ and $-\pi \le \theta < 0$, respectively. In the vicinity of $\theta = 0$, a shock front is formed. Ignoring its structure, we set $\Gamma = 0$ in solution (9). Allowance for nonzero Γ values can be made by the method of matched asymptotic expansions (see, e.g., [12]) and will give only small corrections (in the strongly pronounced-nonlinearity mode) for the energy characteristics of the field.

The one-period profiles of oscillations are shown in Fig. 1 for the *D* selective absorption values [Eq. (8)] equal to 0, 1, 4, 10, and 20. In the presence of only nonlinear absorption, the profile has the form

$$V_{st}(\theta) = 2\cos\frac{\theta}{2}\operatorname{sgn}\theta, \qquad (10)$$

which is the known solution of the nonuniform Burgers equation [11] and follows from (9) for $D = 0$. With an increase in the selective absorption *D*, the dimensionless amplitude of the discontinuity does not increase, but a noticeable increase in the perturbation V_{st} is observed in smooth sections of the profile. For $D \gg 1$, the oscillation is almost harmonic, $V_{st} \approx V_0\sin\theta$, and the jump of the small relative magnitude $2 \ll V_0$ only remains at the point $\theta = 0$.

Thus, the amplitude B_2 of the second harmonic $2\omega_0$ decreases noticeably with increasing *D*. The onset of this process is shown in Fig. 2. The suppression of the $2\omega_0$ wave retards the energy transfer to higher harmon-

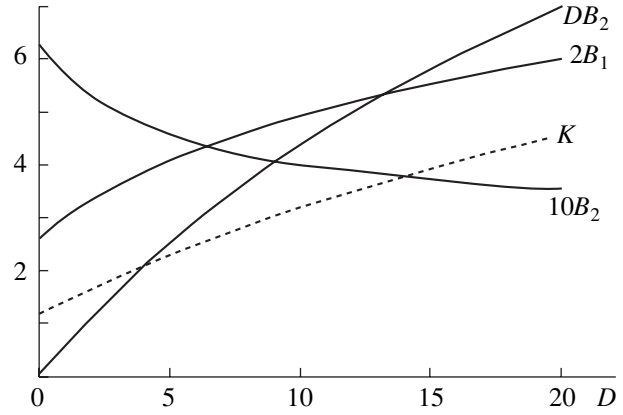

Fig. 2. The solid lines are the amplitudes B_1 and B_2 of the first and second harmonics, respectively, and the corresponding product DB_2 for various values of selective absorption D and (dashed line) the amplification coefficient K of the oscillation energy accumulated in the cavity of resonator.

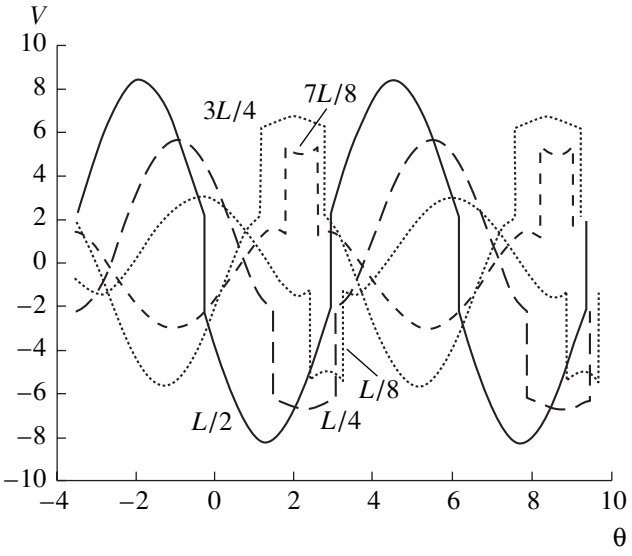

Fig. 3. Shapes of oscillations in the cavity sections $x = L/8$, $L/4$, $L/2$, $3L/4$, and $7L/8$ for $D = 20$.

ics $3\omega_0$, $4\omega_0$, … . Therefore, energy is accumulated at the fundamental frequency ω_0, which virtually does not attenuate. The first-harmonic amplitude $B_1(D)$ is also shown in Fig. 2. This figure shows product $DB_2(D)$ appearing in the basic formulas below.

In particular, perturbation (9) attains the maximum value $V_{st} = 2$ at $\theta = 0$ for $DB_2 \le 0.5$, and for $DB_2 > 0.5$ the peak (see Fig. 1) is shifted to the point θ_{max} at which

$$V_{max} = V_{st}\left(\theta_{max} = \arccos\frac{1}{2DB_2}\right) = \frac{1 + 2DB_2}{\sqrt{2DB_2}}. \quad (11)$$

The mean intensity over period

$$I = \overline{V_{st}^2} = 2 + DB_2(D) \quad (12)$$

also increases with an increase in $DB_2(D)$, i.e., with the enhancement of selective absorption.

In the limit $D \gg 1$, we obtain the formula $DB_2 \approx 2^{1/3}D^{2/3}$ and the expressions

$$V_{st} \approx 2^{2/3}D^{1/3}\sin\theta + 2^{1/3}D^{-1/3}\sin 2\theta, \quad (13)$$

$$V_{max} \approx 2^{2/3}D^{1/3}, \text{ and } I \approx 2^{1/3}D^{2/3} \quad (14)$$

for the steady-state profile, maximum (11), and mean intensity (12), respectively.

The profiles of standing waves between the walls of resonator $0 < x \le L$ are plotted by combining two functions (9) shifted relative to another [2, 3]:

$$V(x, \omega_0 t) = V\left(\omega_0 t + \pi - \pi\frac{x}{L}\right) - V\left(\omega_0 t - \pi + \pi\frac{x}{L}\right). \quad (15)$$

The shapes of oscillations measured in the cavity sections $x = L/8$, $L/4$, $L/2$, $3L/4$, and $7L/8$ are shown in Fig. 3 for $D = 20$. Similar profiles in the absence of selective absorption ($D = 0$) were plotted earlier (see Fig. 4 in [3])

The comparison of results shows that for $D = 20$ the "traveling discontinuities" in the profiles of standing waves are less pronounced than in the absence of selective losses. Consequently, nonlinear attenuation is partially suppressed. As a result, the maximum V values in Fig. 3 are approximately as high as the corresponding peaks for $D = 0$.

The Q-factor of the resonator in the nonlinear oscillation mode with a complicated spectrum can be defined as the ratio of the maximum velocity perturbation $2u_{max}$ in the standing wave to the velocity amplitude A of the boundary oscillations:

$$Q = 2\frac{u_{max}}{A} = \sqrt{\frac{2c}{\pi\varepsilon A}}\Phi(DB_2);$$
$$\Phi = \frac{1 + 2DB_2}{\sqrt{2DB_2}} \text{ for } 2DB_2 > 1, \quad (16)$$
$$\text{and } \Phi = 2 \text{ for } 2DB_2 \le 1.$$

It is also possible to define Q in terms of the ratio of the average intensities of these oscillations:

$$Q^2 = \frac{2\overline{u^2}}{A^2/2} = \frac{2c}{\pi\varepsilon A}(2 + DB_2). \quad (17)$$

Formulas (16) and (17) both describe an increase in the Q-factor with enhancement the selective absorption D.

"Amplification coefficient" $K(D)$ of the oscillation energy accumulated in the resonator cavity is shown in Fig. 2 by the dashed line.

The estimation of the nonlinear factor Q_{nl} by Eq. (2) for a conventional air-filled resonator whose boundary oscillates with the velocity $A = 10$ cm/s yields $Q_{nl} \approx 85$.

If the right wall $x = L$ of the resonator transmits 98% of the incident radiation power at the second harmonic frequency, it follows from Eq. (16) that $Q \approx 300$; i.e., selective losses should increase the resonator *Q*-factor by a factor of about 3.5 and the energy of oscillations by more than an order of magnitude.

We note that the problems of nonlinear systems with selective losses are recently of interest in connection with a number of applications [13, 14].

ACKNOWLEDGMENTS

This work was supported by INTAS, the US Civilian Research and Development Foundation for the Independent States of the Former Soviet Union, and Russian Foundation for Basic Research (including the grant for support of Leading Scientific Schools).

REFERENCES

1. O. V. Rudenko and S. I. Soluyan, *Theoretical Foundations of Nonlinear Acoustics* (Nauka, Moscow, 1975; Consultants Bureau, New York, 1977).
2. V. V. Kaner, O. V. Rudenko, and R. V. Khokhlov, Akust. Zh. **23**, 756 (1977) [Sov. Phys. Acoust. **23**, 432 (1977)].
3. O. V. Rudenko, C. M. Hedberg, and B. O. Enflo, Akust. Zh. **47** (2001) [Acoust. Phys. **47**, 452 (2001)].
4. A. B. Coppens and A. A. Atchley, in *Encyclopedia of Acoustics* (Wiley, New York, 1997), pp. 237–246.
5. R. Lanbury, Phys. Today **51** (2), 23 (1998).
6. O. V. Rudenko, Akust. Zh. **45**, 397 (1999) [Acoust. Phys. **45**, 351 (1999)].
7. O. V. Rudenko, Akust. Zh. **29**, 398 (1983) [Sov. Phys. Acoust. **29**, 234 (1983)].
8. O. V. Rudenko, Priroda (Moscow), No. 7, 16 (1986).
9. V. G. Andreev, V. É. Gusev, A. A. Karabutov, *et al.*, Akust. Zh. **31**, 275 (1985) [Sov. Phys. Acoust. **31**, 162 (1985)].
10. O. V. Rudenko and A. V. Shanin, Akust. Zh. **46**, 392 (2000) [Acoust. Phys. **46**, 334 (2000)].
11. A. A. Karabutov, E. A. Lapshin, and O. V. Rudenko, Zh. Éksp. Teor. Fiz. **71**, 111 (1976) [Sov. Phys. JETP **44**, 58 (1976)].
12. O. A. Vasil'eva, A. A. Karabutov, E. A. Lapshin, and O. V. Rudenko, *The Interaction of One-Dimensional Waves in Dispersion-Free Media* (Mosk. Gos. Univ., Moscow, 1983).
13. V. E. Gusev, H. Balliet, P. Lotton, *et al.*, J. Acoust. Soc. Am. **103**, 3717 (1998).
14. V. A. Khokhlova, S. S. Kashcheeva, M. A. Avierkiou, and L. A. Crum, AIP Conf. Proc. **524**, 151 (2000).

Translated by T. Galkina

Doklady Physics, Vol. 47, No. 3, 2002, pp. 192–194. Translated from Doklady Akademii Nauk, Vol. 383, No. 1, 2002, pp. 37–39.

TECHNICAL PHYSICS

The Selection of an Efficient Blast-Reduction Method when Detonating Explosives

B. E. Gelfand* and M. V. Sil'nikov**

Presented by Academician Yu.S. Vasil'ev September 3, 2001

Received September 17, 2001

The choice of simple and efficient means for protection from blast loads when detonating explosives is a topical problem in fundamental and applied studies. In searching for these means, sources of blast loads in the form of explosive charges were placed inside various containment shells or immersed in diverse media consuming blast energy.

There exist two directions aimed at creating means for blast protection. The first is associated with the obvious attempt to surround an explosive charge by a solid impermeable shell. Here, we deal with a trivial case when an explosive charge is placed into a closed or half-closed container [1]. In practice, it was shown that this method of charge localization is poorly efficient. Afterwards, in order to improve the exploitation properties of a protective container, its inner cavity came to be filled with a compressible substance. In [2], [3], and [4], a liquid foam, a liquid containing gas bubbles, and a granular or fibrous material, respectively, were used as fillers of containers. Each of these blast-consuming media can be characterized by an effective apparent density σ, which differs from the skeleton-material density ρ. For example, for water foam, $\sigma = 10–30$ kg/m^3 at $\rho = 1000$ kg/m^2; for water saturated with gas bubbles, $\sigma = 900–990$ kg/m^3; and for fibrous and granular fillers, $\sigma \geq 1000$ kg/m^3 at $\rho \geq 2000$ kg/m^3.

The second line of studies aimed at creating means of protection is specified by the complete rejection of an impermeable solid shell around an explosive charge. In this case, a variant of blast suppression in the volume of a sprayed liquid (most often, water) can be considered as an ultimate case [5]. However, due to the impossibility of obtaining highly concentrated liquid sprays with $\sigma \geq 1–2$ kg/m^3, this means of blast suppression has proved unfeasible.

In order to obtain a sufficient concentration of a blast-consuming material to provide reliable damping of explosive waves, gas-filled covers consisting of water foam [6] or polyurethane foam [7] were proposed. For these materials, $\sigma = 10–20$ kg/m^3 and 50–100 kg/m^3, respectively, while $\rho = 900$ kg/m^3.

In practice, the application of gas-filled shells to confine the demolition effects of explosive charges (with a weight not more than 3 kg) has shown that the energy of explosion products is spent mainly for the kinematic acceleration of containment shells. In addition, the role of the transformation of energy flows at the interfaces of explosion products, the blast-consuming medium, and the atmosphere is also significant. Attempts associated with regulating blast loads at the expense of energy loss for evaporating or spraying protective-medium materials have demonstrated little effect.

By virtue of the dominating role of inertial properties of containment shells when suppressing explosion shock waves, the change in the kinematic characteristics of a medium that damped the expansion of explosion products turned out to be an efficient means of blast reduction. Note that, for the medium surrounding an explosive charge, the compressibility is the most important characteristic. A reliable reduction of explosion effects is attained when the protective medium is a liquid that assures (at least, at initial expansion stages) against the penetration of explosion products into the atmosphere being protected.

As is known, the measure of the compressibility of a liquid is the speed of sound in it. We can control the speed of sound in a liquid by incorporating into its volume porous elements, gas bubbles, or hollow polymeric inclusions. The embedding of compressible inclusions is especially significant in affecting the propagation of moderate-intensity shock waves with a frontal pressure drop $\frac{P_1}{P_0} \leq 1000$. For higher-intensity shock waves, the presence of compressible elements is of less importance. The immersion of explosive charges in a compressible two-phase medium critically changes the characteristic time scales of all wave processes and

* *Semenov Institute of Chemical Physics, Russian Academy of Sciences, ul. Kosygina 4, Moscow, 117977 Russia*

** *Scientific and Industrial Enterprise of Special Materials, B. Sampsonievskiĭ pr. 28A, St. Petersburg, 194044 Russia*

1028-3358/02/4703-0192$22.00

enhances the possibilities of efficient energy exchange between the explosion products and the containment shell [8].

These arguments make it possible to propose a new blast-reduction method. Figure 1a shows such a scheme for an explosive charge (*1*), which involves a thin layer of a liquid dispersion medium confined in the volume (*2*) between elastic shells (*3*). The liquid layer is separated from the explosive charge by a gas-filled spacing [4]. The arrangement of the basic elements differs from that in the case of a traditional scheme [9] (Fig. 1b). The crucial role of the air spacing consists in reducing the amplitude of the shock wave (due to the difference in the explosive-charge volume R_{ch} and the shell inner cavity R_{in}) before its meeting with the liquid layer.

On the basis of published [9] and new experimental data, we can compare the efficiency of the blast reduction for the schemes shown in Figs. 1a and 1b. Information on the blast reduction with the help of a water shell contacting the explosive charge (i.e., for the scheme shown in Fig. 1b) was taken from [9]. Data on the blast reduction according to the scheme shown in Fig. 1a were obtained in a series of experiments similar to [10]. The ratio of the water mass (M) to the explosive-charge mass (G) was 50 (G = 40 and 100 g in [9] and [10], respectively).

Figure 2 shows the amplitude variation Φ for the coefficient of the blast reduction as a function of the normalized distance $R^* = \frac{R}{G^{1/3}}$. The distance R was measured from the blast epicenter to the measurement point. The blast-reduction coefficient $\Phi = \frac{\Delta P(R^*)}{\Delta P_0(R^*)}$ was evaluated using the amplitude of the shock wave $\Delta P(R^*)$ for the explosion in the liquid shell and the amplitude $\Delta P_0(R^*)$ for the explosion in the gas-filled shell of the same size according to the scheme shown in Fig. 1c. This is justified by the fact that the value of ΔP_0 (crosshatched region *1* in Fig. 2) is by 10–20% smaller than that of $\Delta P_1(R^*)$ for a completely open charge.

The regions *2* and *3* for values of Φ in Fig. 2 were obtained, respectively, for explosions corresponding to the schemes shown in Figs. 1b and 1a.

Figure 3 shows the variation in the pressure pulse for the shock wave in the case of compression phase I_+ when detonating an explosive in the gas-filled air shell (curve *1* according to [9]). The bands of values denoted as *2* and *3* for I_+ were obtained for explosions using the schemes shown in Figs. 1b and 1a, respectively.

The plots in Figs. 2 and 3 confirm that the scheme presented in Fig. 1a for reducing the demolition effect of an explosion has the highest efficiency.

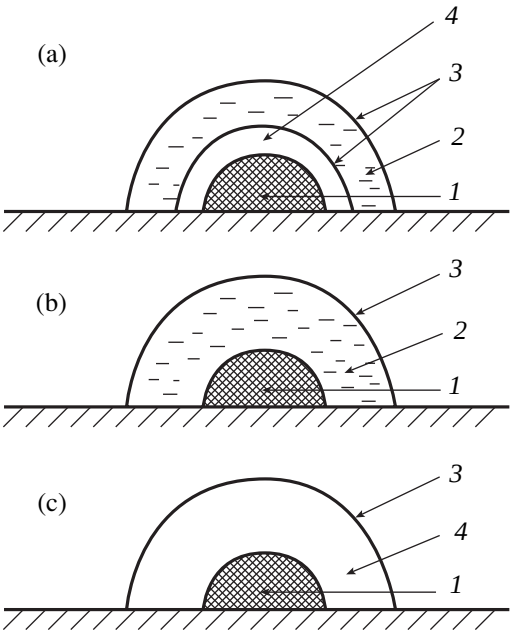

Fig. 1. Possible schemes of blast reduction, which use elastic containers filled with liquids: (*1*) explosive charge, (*2*) dispersion medium, (*3*) elastic shells, and (*4*) air spacing.

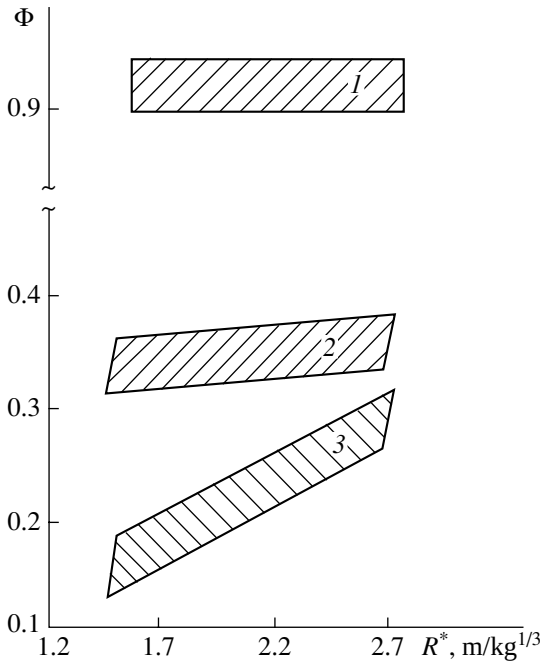

Fig. 2. Dependence of the coefficient of the shock-wave amplitude reduction on the normalized distance in the case of various blast schemes.

Our investigations are based on the rational use of propagation features for pressure waves and rarefaction waves when detonating explosives in a medium characterized by elevated (compared not only to a liquid, but also to a gas) compressibility.

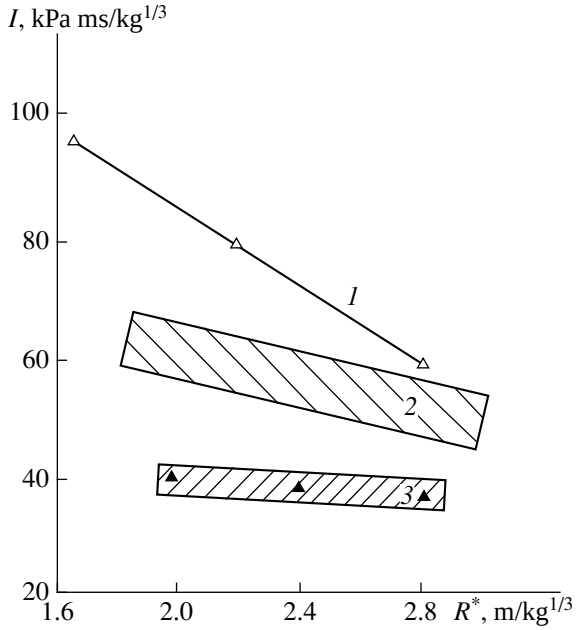

Fig. 3. Dependence of the pressure pulse for the compression phase on the normalized distance in the case of various blast schemes.

The essential distinction in the above method of blast reduction is the preliminary correction of initial conditions for the expansion of explosion products due to the attached volume of a thin gas layer between the explosive-charge surface and a compressible medium.

The described method of blast reduction was used in designing a series of devices for the rapid and reliable protection of equipment and personnel in the process of the conservation and/or elimination of explosive substances and systems.

REFERENCES

1. J. M. Powers and H. Krier, J. Haz. Mater **13**, 121 (1986).
2. R. Raspet, P. B. Butler, and F. Yahani, Appl. Acoust. **22**, 35 (1987).
3. A. A. Borisov, B. E. Gelfand, and E. I. Timofeev, Int. J. Multiphase Flow **9**, 531 (1983).
4. R. Raspet, P. B. Butler, and F. Yahani, Appl. Acoust. **22**, 243 (1987).
5. A. A. Buzukov, Fiz. Goreniya Vzryva **36**, 120 (2000).
6. V. M. Kudinov, B. I. Palamarchuk, B. E. Gelfand, and S. A. Gubin, Dokl. Akad. Nauk SSSR **228**, 555 (1976) [Sov. Phys. Dokl. **21**, 256 (1976)].
7. H. Kleine, K. Disconescu, and J. H. S. Lee, in *Proc. 20 Intern. Symp. on Shock Waves, Singapore, 1996* (World Sci., Singapore, 1996), Vol. 2, p. 1351.
8. I. M. Voskoboĭnikov, B. E. Gelfand, S. A. Gubin, *et al.*, Inzh.-Fiz. Zh. **31**, 674 (1976).
9. M. A. Rinaudo, P. D. Smith, T. A. Rose, in *Proc. of the 15 Int. Symp. on Military Aspects of Blast and Shock, Suffield, 1997* (Suffield, 1997), p. 225.
10. B. E. Gelfand, M. V. Sil'nikov, A. I. Mikhaĭlin, and A. V. Orlov, Fiz. Goreniya Vzryva **37**, 128 (2001).

Translated by Yu. Vishnyakov

Doklady Physics, Vol. 47, No. 3, 2002, pp. 195–200. Translated from Doklady Akademii Nauk, Vol. 383, No. 1, 2002, pp. 40–45.

TECHNICAL PHYSICS

A New Method of Multidimensional-Signal Processing with the Use of *R* Functions and Atomic Functions

V. F. Kravchenko* and M. A. Basarab**

Presented by Academician Yu.V. Gulyaev May 24, 2001

Received May 25, 2001

INTRODUCTION

Employment of atomic functions (AF) in the digital processing of one-dimensional signals was thoroughly analyzed in [1, 2]. Many operations of one-dimensional signal processing are considered to be applicable to the multidimensional case [3]. For example, employing operations of the direct product or rotation of one-dimensional windows, it is possible to synthesize multidimensional atomic-function windows having rectangular, hexagonal, or circular apertures. While using windows with an arbitrary reference region, certain complications of both a qualitative and quantitative nature arise, which are associated with a necessity of analytically describing the geometry of this region. This problem can be solved with the help of application of the *R*-function method [4]. In the present paper, we consider for the first time problems of constructing multidimensional windows based on both *R* functions and atomic functions, as well as on the concepts developed in [1].

R FUNCTION AND THE INVERSE PROBLEM OF ANALYTICAL GEOMETRY

Let a region Ω with the boundary $\partial\Omega$ be given in the space R^n. Let it be necessary to construct a function $\omega(\mathbf{x})$, $\mathbf{x} = (x_1, x_2, \ldots, x_n)$. This function must be strictly positive inside Ω, negative outside Ω, and equal to zero on $\partial\Omega$. The equation $\omega(x) = 0$ determines in the implicit form the boundary of the region. We assume that Ω can be represented as a combination of certain initial regions $\Omega_1, \Omega_2, \ldots, \Omega_m$ on the basis of the following logical operations over sets, namely, $\cap$ (intersection), $\cup$ (association), and $\neg$ (complementation). We can write out this assumption in the form

$$\Omega = F(\{\Omega_1, \Omega_2, \ldots, \Omega_m\}, \{\cap, \cup, \neg\}). \quad (1)$$

In this case, we also assume that the initial regions have simpler shapes than Ω and that, for each of them, the equation for its boundary $\omega_i(\mathbf{x}) = 0$, $i = 1, 2, \ldots, m$ is known. The theory (method) of *R* functions was developed by Rvachev [4]. In the framework of the set theory, this method makes it possible (on the basis of describing the Ω region) to obtain the equation $\omega(\mathbf{x}) = 0$ in the analytical form for the boundary of this region. According to [4], one of the basic complete systems of *R* functions is the $\mathfrak{R}_\alpha$ system of the form

$$x \wedge_\alpha y \equiv \frac{1}{1+\alpha}(x + y - \sqrt{x^2 + y^2 - 2\alpha xy}),$$
$$x \vee_\alpha y \equiv \frac{1}{1+\alpha}(x + y + \sqrt{x^2 + y^2 - 2\alpha xy}), \quad (2)$$
$$\neg x \equiv -x.$$

Here, $\alpha = \alpha(x, y)$ is an arbitrary function satisfying the condition $-1 < \alpha \le 1$. Usually, it is assumed that $\alpha \equiv 0$ ($\mathfrak{R}_0$ system) or $\alpha \equiv 1$ ($\mathfrak{R}_1$ system). The correspondence established by Rvachev between logical-algebra functions and *R* functions makes it possible to find a constructive solution to the inverse problem of analytical geometry. To do this, it is sufficient to formally exchange in (1) Ω by $\omega(\mathbf{x})$, Ω_i by $\omega_i(\mathbf{x})$, $i = 1, 2, \ldots, m$, and to use symbols of *R* operations $\{\wedge, \vee, -\}$ in system (2) instead of $\{\cap, \cup, \neg\}$, respectively. As a result, we obtain the analytical expression that determines the equation for the boundaries of the region Ω in terms of elementary functions

$$\omega(\mathbf{x}) = 0. \quad (3)$$

In this case, $\omega(\mathbf{x}) > 0$ for inner points and $\omega(\mathbf{x}) < 0$ for outer points of the region Ω.

* *Institute of Radio Engineering and Electronics, Russian Academy of Sciences, Mokhovaya ul. 18, Moscow, 103907 Russia*

** *Bauman Moscow State Technical University, Vtoraya Baumanskaya ul. 5, Moscow, 107005 Russia*

1028-3358/02/4703-0195$22.00

ATOMIC FUNCTIONS

The class of atomic functions [1, 2] includes finite solutions to functional differential equations (FDE) of the form

$$\sum_{n=1}^{N} d_n y^{(n)}(x) = \sum_{m=1}^{M} c_m y(ax - b_m).$$

Here, a, d_n, c_m, and b_m are numerical parameters, and $|a| > 1$. One of basic types of AF is determined by the following FDE:

$$\frac{2y'(x)}{a^2} = y(ax+1) - y(ax-1), \quad (4)$$

where $a > 1$. Finite solutions (4) with the carrier $\left[-\frac{1}{a-1}, \frac{1}{a-1}\right]$ are usually denoted as $h_a(x)$ [5]. Their Fourier transform has the form

$$F_a(p) = \prod_{k=1}^{\infty} \operatorname{sinc}(pa^{-k}), \quad (5)$$

where $\operatorname{sinc}(x) \equiv \frac{\sin x}{x}$. Using expression (4), we can express the derivatives of the nth order in terms of the values of functions themselves. For $a = 2$, we obtain the most well-known and investigated function $h_2(x) \equiv \operatorname{up}(x)$. The principal properties of both the parent's function $\operatorname{up}(x)$ and the function $h_a(x)$ are described in [1, 2, 4, 5]. As a rule, atomic functions and R^n functions are constructed on the basis of the direct product of one-dimensional AF, e.g.,

$$\operatorname{up}_n(\mathbf{x}) = \prod_{j=1}^{n} \operatorname{up}(x_j).$$

SYNTHESIZING TWO-DIMENSIONAL FILTERS WITH A FINITE PULSE CHARACTERISTIC AND A REGULAR APERTURE ON THE BASIS OF ATOMIC FUNCTIONS

One promising direction in the application of R functions and atomic functions is the digital processing of multidimensional signals. As is well known [3], in problems of the digital filtration of two-dimensional signals, filters with a finite pulse characteristic (FPC filters) gained the most acceptance. Their principal advantage compared to filters with an infinite pulse characteristic is the possibility to synthesize filters with a zero phase shift. In addition, a number of difficulties in constructing two-dimensional filters with an infinite pulse characteristic are associated with the necessity to provide their stability. A two-dimensional FPC filter ensures the zero phase shift, provided that its frequency characteristic is a real-valued function $H(\omega_1, \omega_2) = H^*(\omega_1, \omega_2)$ or that the pulse characteristic is symmetric with respect to the origin of a coordinate system; i.e., $h[n_1, n_2] = h^*[-n_1, -n_2]$. There exist several methods for calculating two-dimensional FPC filters [3]; among them, the window-function method is the most widely propagated in practice. In correspondence with this method, the desired two-dimensional frequency characteristic of the filter is represented in the form of the Fourier series

$$H_0(\omega_1, \omega_2) = \sum_{n_1=-\infty}^{\infty} \sum_{n_2=-\infty}^{\infty} h_0[n_1, n_2] e^{-j(\omega_1 n_1 + \omega_2 n_2)}, \quad (6)$$

where

$$h_0[n_1, n_2] = \frac{1}{4\pi^2} \int_{-\pi}^{\pi}\int_{-\pi}^{\pi} H_0(\omega_1, \omega_2) e^{j(\omega_1 n_1 + \omega_2 n_2)} d\omega_1 d\omega_2.$$

Here, $h_0[n_1, n_2]$ is the infinite pulse characteristic of a two-dimensional filter that corresponds to the given frequency characteristic $H_0(\omega_1, \omega_2)$. In order to realize the two-dimensional FPC filter, the summation in series (6) should be limited. This results in deteriorating the convergence of truncated series (6) to the given frequency characteristic in its discontinuity points (the so-called Gibbs effect). To improve the convergence, the coefficients $h_0[n_1, n_2]$ should be multiplied by the two-dimensional window function $w[n_1, n_2]$. In other words, the functions

$$h[n_1, n_2] = w[n_1, n_2] \cdot h_0[n_1, n_2]$$

are used as filter coefficients.

For filters with the zero phase shift, the window function must satisfy the condition $w[n_1, n_2] = w^*[-n_1, -n_2]$. Two-dimensional FPC filters are synthesized on the basis of two-dimensional window functions defined on rectangular, hexagonal, or circular reference regions (apertures) [3], which we call regular.

In the simplest case of a square aperture, the two-dimensional weight window is formed on the basis of a direct product of one-dimensional windows

$$w[n_1, n_2] = w[n_1] \cdot w[n_2]. \quad (7)$$

The window with a hexagonal reference region is formed in a similar manner:

$$w[n_1, n_2] = w[n_1] \cdot w\left[\frac{n_1 + n_2\sqrt{3}}{2}\right] \cdot w\left[\frac{n_1 - n_2\sqrt{3}}{2}\right]. \quad (8)$$

Finally, in the case of a circular aperture, the two-dimensional window is obtained by rotating a one-dimensional window about the symmetry axis and is described by the expression

$$w[n_1, n_2] = w[\sqrt{n_1^2 + n_2^2}]. \quad (9)$$

A large number of one-dimensional window weight functions are known [1, 15]. In addition, in solving

Table 1. Basic physical parameters of two-dimensional Kravchenko–Rvachev windows constructed on the basis of the atomic function $h_0(x)$

Parameter a	Equivalent noise band, bin	Correlation of overlapping segments (50% overlap), %	Parasitic amplitude modulation, dB	Maximum transformation loss, dB	Maximum level of side lobes, dB	Window width at the 6-dB level, bin	Coherent amplification
	b_1	b_2	b_3	b_4	b_5	b_7	b_8
1.1	20.7	2×10^{-7}	0.2	13.4	−154.3	6	0.03
1.2	10.24	8×10^{-3}	0.3	10.4	−86.1	4.2	0.05
1.3	7.02	0.18	0.5	9	−55.2	3.5	0.07
1.5	4.49	2	0.7	7.2	−36.3	2.8	0.12
2	2.62	12	1.2	5.4	−23.3	2.1	0.25
3	1.74	29	1.8	4.2	−17	1.7	0.45
5	1.35	40	2.5	3.8	−14.5	1.5	0.64

problems of one-dimensional signal processing, new widow classes, e.g., Rvachev–Kravchenko windows and Kravchenko windows (both based on atomic functions), as well as hybrid windows, e.g., Kravchenko–Hamming windows, Kravchenko–Kaiser windows, and Kravchenko–Blackman–Harris windows, find application [1, 2]. Using expressions (7)–(9), we can synthesize their two-dimensional analogs with regular reference regions. Below, we thoroughly analyze windows with square apertures, which are based on the atomic function $h_a(x)$. To compare the characteristics of two-dimensional windows (in the plane $\omega_2 = 0$) defined on the square aperture ($-1 \le x \le 1, -1 \le y \le 1$), we employ the following set of physical parameters.

1. The equivalent noise band,

$$b_1 = 4\frac{\int_{-1}^{1}\int_{-1}^{1} w^2(x, y)dxdy}{\left[\int_{-1}^{1}\int_{-1}^{1} w(x, y)dxdy\right]^2}.$$

2. The correlation of overlapping segments,

$$b_2 = \frac{\int_{-1}^{0}\int_{-1}^{1} w(x, y)w(x-1, y)dxdy}{\int_{-1}^{1}\int_{-1}^{1} w^2(x, y)dxdy}100\%.$$

3. The parasitic modulation amplitude (expressed in decibels),

$$b_3 = -10\log\left|\frac{W(\pi/2, 0)}{W(0, 0)}\right|^2,$$

where $W(p, q)$ is the two-dimensional Fourier transform for the window function.

4. The maximum transformation loss (expressed in decibels),

$$b_4 = 10\log(b_1) + b_3.$$

5. The maximum level of side lobes (expressed in decibels),

$$b_5 = 10\log\max_k\left|\frac{W(u_k, 0)}{W(0, 0)}\right|^2,$$

where $\{u_k\}$ are points of local maxima (excluding u_0).

6. The asymptotic-decrease velocity for side lobes (expressed in decibels per octave),

$$b_6 = 10\log\lim_{u\to\infty}\left|\frac{W(2u, 0)}{W(u, 0)}\right|^2.$$

7. The window width at the 6-db level,

$$b_7 = 2u,$$

where u is the maximum frequency such that $10\log\left|\frac{W(0, 0)}{W(u, 0)}\right|^2 = 6$.

8. The coherent amplification,

$$b_8 = \frac{1}{4}\int_{-1}^{1}\int_{-1}^{1} w(x, y)dxdy.$$

Here, the normalization conditions $w(x, y) = 0$ for $|x| > 1$ or $|y| > 1$; $w(0, 0) = 1$; and $w(-x, y) = w(x, y) = w(x, -y) = w(-x, -y)$ are fulfilled. By virtue of the condition of symmetry in the plane $\omega_1 = 0$, the window has the same characteristics.

The principal physical characteristics of the normalized windows $\frac{h_a(x/(a-1))}{h_a(0)}$ as functions of the parameter a are presented in Table 1. As in the one-dimensional case, owing to the infinite differentiability of atomic weight functions, the value of b_5 for all taken

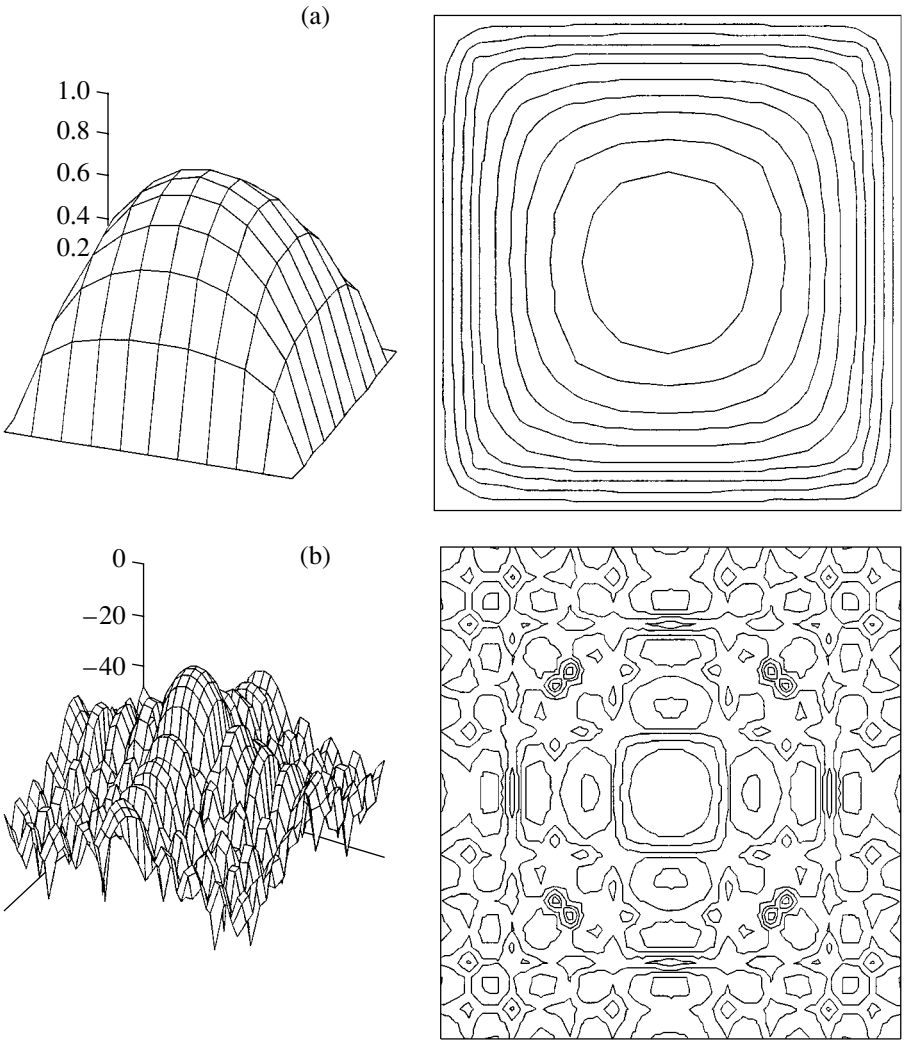

Fig. 1. Two-dimensional Kravchenko–Rvachev window with a square reference region, which is constructed on the basis (a) of the $\Re_0$ system, and (b) of the logarithm of its frequency characteristic.

windows is equal to infinity. In the case of ignoring this parameter, windows with $a \geq 2$ are similar to well-known Tukey windows [1].

In the one-dimensional case, modified $(M + 1)$-term windows of the form [1, 2]

$$\tilde{w}(x) = w(x) + \sum_{k=1}^{M} c_k w^{(2k)}(x) \qquad (10)$$

are used with the intent of improving the b_5 parameter. We now employ a similar approach for the two-dimensional case restricting this approach by the two-term windows ($M = 1$). We consider two-dimensional weight functions with a square aperture, which are based on one-dimensional windows [1]:

$$w_1(x) = \mathrm{up}(x) + 0.01\mathrm{up}''(x),$$

$$w_2(x) = 1.5249\left(h_{1.5}(2x) + \frac{1}{128}h''_{1.5}(2x)\right).$$

The numerical experiment has shown that as far as the b_5 parameter (equal to –31.1 and –52.7 dB) is concerned the synthesized windows are comparable to the classical Hamming windows (cosine squared) and Blackman windows; however, they considerably exceed these windows with respect to the parameter b_6. The parameters of synthesized windows are: $b_1 = 2.25$ and 3.65 bin; $b_2 = 17$ and 4.7%; $b_3 = 1.4$ and 0.9 dB; $b_4 = 4.9$ and 6.5 dB; $b_7 = 2$ and 2.5 bin; and $b_8 = 0.25$ and 0.14. The choice of a larger number of terms in expansion (10) allows two-dimensional weight windows with higher characteristics to be synthesized.

SYNTHESIZING TWO-DIMENSIONAL FPC FILTERS WITH AN ARBITRARY AMPLITUDE ON THE BASIS OF *R* FUNCTIONS

The above approaches (i.e., direct product and rotation) do not allow us to synthesize two-dimensional fil-

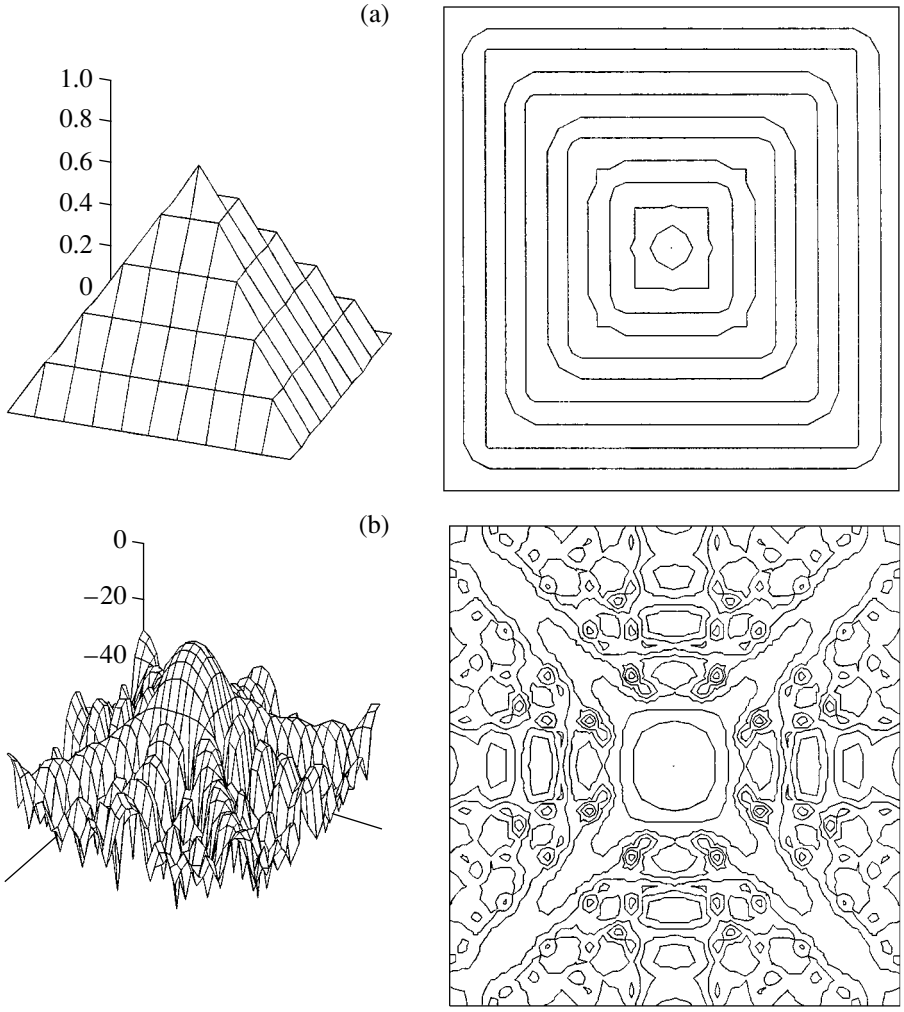

Fig. 2. Two-dimensional Kravchenko–Rvachev window with a square reference region, which is constructed on the basis (a) of the $\Re_1$ system, and (b) of the logarithm of its frequency characteristic.

ters with reference regions of an arbitrary configuration. This statement especially relates to nonconvex regions, e.g., cross-shaped and star-shaped ones. The only exception belongs to filters based on the simplest rectangular Dirichlet window. Employing the *R*-function method, we can efficiently realize the synthesis of two-dimensional windows for apertures of an arbitrary shape.

Let Ω be the required reference region for a window. Using one of the complete systems of *R* functions, we construct an equation for its boundary $\partial\Omega$, $\omega(x, y) = 0$. It is evident that the function

$$\tilde{\omega}(x, y) \equiv \frac{1}{2 \max\limits_{(x, y) \in \Omega} \omega(x, y)} (\omega(x, y) + |\omega(x, y)|) \quad (11)$$

coincides with $\omega(x, y)$ inside Ω, becomes zero outside it, and $\max\limits_{(x, y) \in \Omega} \tilde{\omega}(x, y) = 1$. Here, $\tilde{\omega}(x, y)$ is the window function finite in R^2. The new class of the weight functions (windows) proposed having an arbitrary aperture, we call two-dimensional Kravchenko–Rvachev windows, or KR2 windows. As examples, contour images and perspective projections of square $KR2_1$ windows and $KR2_2$ windows constructed with the help of *R* operations of system (2) in the case of $\alpha \equiv 0$ and $\alpha \equiv 1$ are shown in Figs. 1 and 2. The logarithms of their frequency characteristics (expressed in decibels) are also given in the same figures. Characteristics of these windows are presented in Table 2. Using the diversity of *R*-function systems [4], we can obtain the equation for $\tilde{\omega}(x, y)$ that provides the most suitable frequency characteristic of the desired FPC filter.

We now describe a new method for constructing a two-dimensional analog $w[n_1, n_2]$ of a one-dimensional prototype window $w[n]$ on an arbitrary reference region whose boundary is described by algebraic curves with an order not exceeding two. Initially, on the basis of a complete system (2) of *R* functions for $\alpha \equiv 1$ with the

Table 2. Basic physical parameters of two-dimensional Kravchenko–Rvachev windows

Window	Equivalent noise band, bin	Correlation of overlapping segments (50% overlap), %	Parasitic amplitude modulation, dB	Maximum transformation loss, dB	Maximum level of side lobes, dB	Window width at the 6-dB level, bin	Coherent amplification
	b_1	b_2	b_3	b_4	b_5	b_7	b_8
$KR2_1$	1.27	40	2.4	7.5	−17	1.4	0.55
$KR2_2$	1.5	31	2.1	7.2	−20	1.4	0.33

help of (11), we compose the equation for the reference region $\omega(x, y) \geq 0$ such that $\max \omega(x, y) = \omega(0, 0) = 1$. Furthermore, the two-dimensional window is represented in the form

$$w[n_1, n_2] = w(1 - \omega[n_1, n_2]). \quad (12)$$

In the case of a circular reference region for the unit radius and of a center in the origin, described by the formula $\omega(x, y) = 1 - \sqrt{x_2 - y^2} = 0$, relationship (12) coincides with expression (9). Thus, formula (12) represents the generalization of the expression (9) for the case of the reference region of an arbitrary configuration.

We consider the algorithm proposed for the case of a square aperture represented by the equation

$$\omega(x, y) = (1 - x) \wedge_1 (1 + x) \wedge_1 (1 - y) \wedge_2 (1 + y) = 0$$

or, with allowance for (2) in the complete form,

$$\omega(x, y) = 1 - \frac{1}{2}(|x| + |y| + ||y| - |x||) = 0.$$

Then, formula (12) acquires the form

$$w[n_1, n_2] = w\left(\frac{|n_1| + |n_2| + ||n_1| - |n_2||}{2}\right). \quad (13)$$

We now compare formulas (7) and (13). It is evident that when n_1 or n_2 are equal to zero they yield the same result transforming into the one-dimensional prototype weight function. However, in contrast to expression (7), formula (13) also yields the same function at the diagonals of the square ($|n_1| = |n_2|$). This fact can turn out to be useful, e.g., for image processing, when four rather than two directions in the image plane are equivalent. In addition, the algorithm indicated is applicable for the case of a reference region with an arbitrary geometry, i.e., when the direct product in the forms of (7) or (8) is unacceptable.

CONCLUSIONS

Thus, new designs of two-dimensional windows proposed and substantiated in this paper can find wide application in solving problems of processing multidimensional digital signals of Doppler radars and radar stations with digital synthesis of the antenna's aperture, in the case of signal isolation and compression, and in solving problems of medical telemetry, mathematical modeling of a heart bioelectric generator, computer thermography, and tomography as well.

ACKNOWLEDGMENTS

The authors are grateful to Academician Yu.V. Gulyaev, Academician of the National Academy of Sciences of the Ukraine V.L. Rvachev, Corresponding Member of the RAS V.I. Pustovoĭt, and Professor A.V. Sokolov for discussing the results of this work.

REFERENCES

1. V. F. Kravchenko, Dokl. Akad. Nauk **382**, 190 (2002) [Dokl. Phys. **47** (2002)].
2. E. G. Zelkin and V. F. Kravchenko, Radiotekh. Élektron. **46**, 903 (2001).
3. D. E. Dudgeon and R. M. Mersereau, *Multidimensional Signal Digital Processing* (Prentice-Hall, Englewood Cliffs, London, 1984; Mir, Moscow, 1988).
4. V. L. Rvachev, *R-Function Theory and Applications* (Naukova Dumka, Kiev, 1982).
5. V. L. Rvachev and V. A. Rvachev, *Nonclassical Methods in Theory of Approximations for Boundary Value Problems* (Naukova Dumka, Kiev, 1979).

Translated by G. Merzon

Doklady Physics, Vol. 47, No. 3, 2002, pp. 201–205. Translated from Doklady Akademii Nauk, Vol. 383, No. 2, 2002, pp. 189–193.

TECHNICAL PHYSICS

Application of Singular Integral Equations for Solving Problems of Wave Diffraction on an Array Composed of Irregular Planar Strips

V. A. Doroshenko* and V. F. Kravchenko**

Presented by Academician V.A. Sadovnichiĭ September 28, 2001

Received September 28, 2001

INTRODUCTION

While studying the diffraction of electromagnetic waves on ideally conducting arrays, the solution to electrodynamic boundary value problems is traditionally reduced to that of the first or second boundary value problem of mathematical physics. However, variation in the geometry of the structure that we deal with and allowance for its physical parameters (e.g., the impedance) that were not previously taken into account result in the complication of the mathematical model under consideration. Solving electrodynamic boundary value problems for superconductors and superconducting coatings suggests introducing impedance boundary conditions [1]. This corresponds to solving the third and fourth boundary value problems for such structures (with allowance for connection of the normal and tangential derivatives). In this paper, an approach is proposed based on employing the Kontorovich–Lebedev integral transformation and singular integral equations. This approach is used for solving problems of wave diffraction on a three-dimensional array consisting of irregular planar impedance strips on which the third and fourth boundary conditions are given.

FORMULATION OF THE PROBLEM: THE THIRD BOUNDARY CONDITION ON STRIPS

We consider a scalar problem for wave diffraction on a periodic array composed of N infinitely thin unbounded imperfectly conducting irregular (angular) planar strips having a common vertex. The array is located in the plane $z = 0$ of a Cartesian coordinate system. The array period is $l = \frac{2\pi}{N}$, the width of the strips is α, and the slit width is $d = l - \alpha$ and defines dihedral angles formed by the planes passing through the OZ-axis and the edge of neighboring strips (see figure). We introduce a spherical coordinate system (r, ϑ, φ) with the origin at the vertex of the strips $\left(\text{the array plane is defined by the equation } \vartheta = \frac{\pi}{2}\right)$. A source of spherical waves is located at the point $B(\mathbf{r}_0)$, $\mathbf{r}_0 = (r_0, \vartheta_0, \varphi_0)$, and the wave field varies according to a harmonic law. We need to find a potential $u(\mathbf{r})$, $\mathbf{r} = (r, \vartheta, \varphi)$ corresponding to the total field and satisfying the following equations and conditions.

1. Helmholtz equation (everywhere outside the strips and the source), i.e.,

$$\Delta u - q^2 u = 0, \quad q > 0;$$

2. The boundary condition on the array strips Σ

$$\left(\widehat{\xi} u + \widehat{\zeta}\frac{\partial u}{\partial n}\right)\Big|_{\Sigma} = 0, \quad \widehat{\xi}(r, \varphi)\widehat{\zeta}(r, \varphi) \neq 0; \qquad (1)$$

3. The condition of the energy boundedness

$$\int_D (|u|^2 + |\nabla u|^2) dV < \infty;$$

4. The condition at infinity.

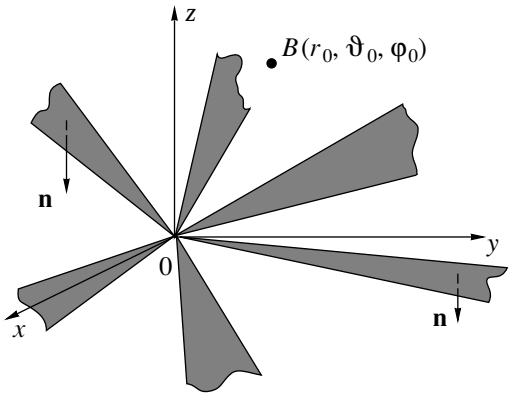

Geometry of the problem.

* *Kharkov Technical University of Radio Electronics, pr. Lenina, Kharkov, 61276 Ukraine*

** *Institute of Radio Engineering and Electronics, Russian Academy of Sciences, Mokhovaya ul. 18, Moscow, 103907 Russia*

1028-3358/02/4703-0201$22.00

The validity of the conditions 2–4 provides the uniqueness of the solution to the problem formulated. With due regard for $\mathbf{n} = \mathbf{e}_\vartheta$, boundary condition (1) can be written as

$$\left(\widehat{\xi}u + \widehat{\zeta}\frac{1}{r}\frac{\partial u}{\partial \vartheta}\right)\Big|_\Sigma = 0,$$

$$\Sigma = \left\{(r, \vartheta, \varphi) \in R^3: r \in [0, +\infty), \vartheta = \frac{\pi}{2}, \varphi \in L\right\}, \quad (2)$$

$$L = \bigcup_{s=1}^{N} L_s, \quad L_s = \left((s-1)l + \frac{d}{2}, sl - \frac{d}{2}\right),$$

$$CL = [0, 2\pi]\backslash L.$$

We now assume that one of the cases

$$\widehat{\xi} = \frac{1}{r}\xi, \quad \xi = \text{const}, \quad \widehat{\zeta} = \zeta, \quad \zeta = \text{const} \quad (3)$$

or

$$\widehat{\zeta} = \zeta r, \quad \zeta = \text{const}, \quad \widehat{\xi} = \xi, \quad \xi = \text{const} \quad (4)$$

takes place. Then, the condition (2) acquires the form

$$\left(\xi u + \zeta\frac{\partial u}{\partial \vartheta}\right)\Big|_\Sigma = 0, \quad (5)$$

where ξ and ζ are constant quantities. Furthermore, we consider boundary condition (5) instead of (1), assuming the validity of formulas (3) or (4). The desired potential u can be represented in the form

$$u = u_0 + u_1. \quad (6)$$

Here, $u_0 = \dfrac{\exp(-qr)}{4\pi r_0|\mathbf{r} - \mathbf{r}_0|}$ corresponds to the source field (primary field), while the potential u_1 is caused by the existence of the array and corresponds to the secondary field.

To solve the problem formulated, we make use of a pair of Kontorovich–Lebedev integral transformations with respect to the radial coordinate [2]:

$$\widehat{G}(\tau) = \int_0^{+\infty} G(r)\frac{K_{i\tau}(qr)}{\sqrt{r}}dr, \quad (7)$$

$$G(r) = \frac{2}{\pi^2}\int_0^{+\infty} \tau\sinh\pi\tau\,\widehat{G}(\tau)\frac{K_{i\tau}(qr)}{\sqrt{r}}d\tau. \quad (8)$$

Here, $K_{i\tau}(z)$ is the Macdonald function. With allowance for the representation

$$u_0 = \frac{2}{\pi^2}\int_0^{+\infty} \tau\sinh\pi\tau \sum_{m=-\infty}^{+\infty} a_{m\tau}U^{(0)}_{m\tau}e^{im\varphi}\frac{K_{i\tau}(qr)}{\sqrt{r}}d\tau, \quad (9)$$

$$U^{(0)}_{m\tau}(\vartheta, \vartheta_0, m, \tau) = \begin{cases} P^m_{-1/2+i\tau}(\cos\vartheta)P^m_{-1/2+i\tau}(-\cos\vartheta_0), & \vartheta < \vartheta_0 \\ P^m_{-1/2+i\tau}(-\cos\vartheta)P^m_{-1/2+i\tau}(\cos\vartheta_0), & \vartheta < \vartheta_0, \end{cases}$$

$$a_{m\tau} = \frac{1}{4r_0}e^{-im\varphi_0}(-1)^m\frac{K_{i\tau}(qr_0)}{\sqrt{r_0}}\frac{1}{\cosh\pi\tau}\frac{\Gamma\left(\frac{1}{2} - m + i\tau\right)}{\Gamma\left(\frac{1}{2} + m + i\tau\right)},$$

where $\Gamma(z)$ is the gamma function and $P^m_{-1/2+i\tau}(\cos\vartheta)$ is the associated Legendre function of the first kind, we seek the potential u_1 in the form of the Kontorovich–Lebedev integral (7)–(9):

$$u_1 = \frac{2}{\pi^2}\int_0^{+\infty} \tau\sinh\pi\tau \sum_{m=-\infty}^{+\infty} b_{m\tau}U^{(1)}_{m\tau}\frac{K_{i\tau}(qr)}{\sqrt{r}}d\tau, \quad (10)$$

$$b_{m\tau} = -a_{m\tau}P^m_{-1/2+i\tau}(\cos\vartheta_0), \quad \vartheta_0 < \frac{\pi}{2},$$

$$U^{(1)}_{m\tau} = \begin{cases} \displaystyle\sum_{n=-\infty}^{+\infty} x_{m,n+m_0}(\tau)\frac{P^{m+nN}_{-1/2+i\tau}(\cos\vartheta)}{\dfrac{d}{d\vartheta}P^{m+nN}_{-1/2+i\tau}(\cos\vartheta)\Big|_{\vartheta=\pi/2}}e^{i(nN+m)\varphi}, \\ 0 < \vartheta < \dfrac{\pi}{2} \\ \displaystyle\sum_{n=-\infty}^{+\infty} y_{m,n+m_0}(\tau)\frac{P^{m+nN}_{-1/2+i\tau}(-\cos\vartheta)}{\dfrac{d}{d\vartheta}P^{m+nN}_{-1/2+i\tau}(-\cos\vartheta)\Big|_{\vartheta=\pi/2}}e^{i(nN+m)\varphi}, \\ \dfrac{\pi}{2} < \vartheta < \pi. \end{cases}$$

FUNCTIONAL RELATIONSHIPS. THE SINGULAR INTEGRAL EQUATION

In order to determine the unknown coefficients $x_{m,n+m_0}$ and $y_{m,n+m_0}$, we use the boundary condition (5)

$$\left[\xi u_1 + \zeta\frac{\partial u_1}{\partial \vartheta}\right]\Big|_{\vartheta=\pi/2+0} = \left[\xi u_1 + \zeta\frac{\partial u_1}{\partial \vartheta}\right]\Big|_{\vartheta=\pi/2-0} = -\left[\xi u_0 + \zeta\frac{u_0}{\partial \vartheta}\right]\Big|_{\vartheta=\pi/2} = g(\varphi), \quad \varphi \in L \quad (11)$$

and the conjugation condition in slits

$$\frac{\partial u_1}{\partial \vartheta}\Big|_{\vartheta=\frac{\pi}{2}-0} = \frac{\partial u_1}{\partial \vartheta}\Big|_{\vartheta=\frac{\pi}{2}+0}, \quad \varphi \in CL. \quad (12)$$

Extracting from formulas (11) and (12) conditions for their transforms (7), and allowing for representation (10), we arrive at the system of equations with respect to the coefficients z_n connected with the desired coefficients (by virtue of the array periodicity, these equations are considered for a period)

$$\xi^2 \sum_{n=-\infty}^{+\infty} \frac{1}{N(n+\nu)} \frac{|n|}{n} (1-\varepsilon_n^{(1)}) z_n e^{in\psi}$$

$$-\zeta^2 \sum_{n=-\infty}^{+\infty} N(n+\nu) \frac{|n|}{n} (1-\varepsilon_n^{(2)}) z_n e^{in\psi} = \xi \hat{g}(\psi), \quad (13)$$

$$|\psi| < \frac{\pi\alpha}{l},$$

$$\sum_{n=-\infty}^{+\infty} z_n e^{in\psi} = 0, \quad \frac{\pi\alpha}{l} < |\psi| \le \pi. \quad (14)$$

Here, $\frac{m}{N} = m_0 + \nu$, m_0 is an integer closest to $\frac{m}{N}$, $-\frac{1}{2} \le \nu < \frac{1}{2}$,

$$\frac{1}{N(n+\nu)} \frac{|n|}{n} (1-\varepsilon_n^{(1)}) = \frac{1}{\pi} (-1)^{N(n+\nu)+1}$$

$$\times \cosh \pi\tau \frac{\Gamma\left(\frac{1}{2} + i\tau + N(n+\nu)\right)}{\Gamma\left(\frac{1}{2} + i\tau - N(n+\nu)\right)} \quad (15)$$

$$\times \frac{1}{\left[\frac{d}{d\vartheta} P_{-1/2+i\tau}^{N(n+\nu)}(\cos\vartheta)\Big|_{\vartheta=\pi/2}\right]^2},$$

$$1-\varepsilon_n^{(2)} = \frac{1}{1-\varepsilon_n^{(1)}}, \quad z_n = (-1)^n (y_{m,n} - x_{m,n}),$$

$$\psi = N\varphi - \frac{|\varphi|}{\varphi}\pi,$$

and $\hat{g}$ is transform (7) of the function g. For $\varepsilon_n^{(j)}$, the estimate

$$\varepsilon_n^{(j)} = O\left(\frac{1}{N^2(n+\nu)^2}\right), \quad N(n+\nu) \gg 1, \quad j = 1, 2$$

takes place. After differentiating both parts of Eq. (14) with respect to ψ and complementing the additional condition at $\psi = \pi$, we obtain the relations

$$\sum_{n=-\infty}^{+\infty} (n+\nu) z_n e^{in\psi} = 0, \quad \frac{\pi\alpha}{l} < |\psi| \le \pi, \quad (16)$$

$$\sum_{n=-\infty}^{+\infty} (-1)^n z_n = 0, \quad \psi = \pi. \quad (17)$$

We now introduce the function

$$F(\psi) = i \sum_{n=-\infty}^{+\infty} N(n+\nu) z_n e^{i(n+\nu)\psi}, \quad \psi \in [-\pi, \pi], \quad (18)$$

where

$$z_n = \frac{1}{2\pi N i (n+\nu)} \int_{-\pi}^{\pi} F(\psi) e^{-i\nu\psi} e^{-in\psi} d\psi, \quad (19)$$

$$n + \nu \ne 0.$$

For $n + \nu = 0$, which is possible at $n = 0$ and $\nu = 0$, z_0 is determined from relationship (17). In accordance with relationship (16),

$$F(\psi) = 0, \quad \frac{\alpha\pi}{l} < |\psi| \le \pi,$$

so that we find from (19)

$$z_n = \frac{1}{2\pi N i (n+\nu)} \int_S F(\psi) e^{i\nu\psi} e^{-in\psi} d\psi, \quad (20)$$

$$S: |\psi| < \delta, \quad \delta = \frac{\alpha\pi}{l}.$$

With allowance for

$$\frac{\pi}{\sin\pi\nu} e^{-i\nu\beta} = \sum_{n=-\infty}^{+\infty} \frac{(-1)^n}{n+\nu} e^{in\beta},$$

we have from relationships (17) and (20)

$$z_0 = -\frac{1}{2\pi i N} \int_S F(\beta) \left(\frac{\pi}{\sin\pi\nu} - \frac{1}{\nu} e^{-i\nu\beta}\right) d\beta. \quad (21)$$

Thus, we can derive a singular integral equation for determination of the unknown function $F(\psi)$ (18) from Eq. (15) by substituting into it the representation (20), (21) for z_n:

$$\frac{1}{\pi} \zeta^2 \int_S \frac{F(\beta) e^{-i\nu\beta}}{\beta - \psi} d\beta$$

$$+ \frac{1}{\pi} \int_S \breve{K}_{m\tau}(\beta - \psi) F(\beta) e^{-i\nu\beta} d\beta = \xi \hat{g}(\psi), \quad (22)$$

$$\psi \in S,$$

where

$$\breve{K}_{m\tau}(\theta) = \zeta^2 \left(\frac{1}{2} \cot\frac{\theta}{2} - \frac{1}{\theta}\right)$$

$$+\frac{1}{2iN}\left(\xi^2 A_\tau^\nu - \zeta^2\frac{1}{A_\tau^\nu}\right)\left(\frac{1}{\nu}-\frac{\pi}{\sin\pi\nu}e^{i\nu\theta}\right)$$

$$+\frac{1}{2i}\xi^2\left[\sum_{n\neq 0}\frac{1}{N^2(n+\nu)^2}\frac{|n|}{n}e^{-in\theta}\right.$$

$$\left.-\sum_{n\neq 0}\frac{1}{N^2(n+\nu)^2}\frac{|n|}{n}\varepsilon_n^{(1)}e^{-in\theta}\right]+\frac{1}{2i}\zeta^2\sum_{n\neq 0}\frac{|n|}{n}\varepsilon_n^{(2)}e^{-in\theta},$$

$$A_\tau^\nu = \frac{1}{N(n+\nu)}\frac{|n|}{n}(1-\varepsilon_n^{(1)})\Big|_{n=0}.$$

The singular integral equation obtained (22) with the Cauchy kernel and the smooth function $\breve{K}_{m\tau}(\theta)$ can be solved numerically by its discretization and the employment of Gaussian quadratures.

THE FOURTH BOUNDARY CONDITION ON STRIPS

We now analyze the problem of wave diffraction on a periodic array composed of strips for which the fourth boundary condition is given. Everywhere outside the strips and the source, the desired potential $w(\mathbf{r})$ satisfies the Helmholtz equation with the boundary conditions

$$\left(\zeta_1\frac{\partial w}{\partial n}+\zeta_2\frac{\partial w}{\partial \varsigma}\right)\Big|_\Sigma = 0, \quad \zeta\zeta_2\neq 0, \tag{23}$$

constraints of the finite energy, and conditions at infinity. In condition (23), $\frac{\partial w}{\partial n}$ and $\frac{\partial w}{\partial \varsigma}$ are the normal and tangential derivatives of $w(r)$, respectively,

$$\zeta_1 = \zeta_1(r,\varphi), \quad \zeta_2 = \zeta_2(r,\varphi),$$
$$\mathbf{n} = \mathbf{e}_\vartheta, \quad \varsigma = \nu_r\mathbf{e}_r + \mu_\varphi\mathbf{e}_\varphi. \tag{24}$$

Taking into account relationships (24), we can write out conditions (23) in the form

$$\left(\zeta_2 r\nu_r\frac{\partial\nu}{\partial r}+\zeta_1\frac{\partial\nu}{\partial\vartheta}+\zeta_2\mu_\varphi\frac{\partial\nu}{\partial\varphi}\right)\Big|_\Sigma = 0. \tag{25}$$

Assuming $\nu_r = 0$, we obtain from boundary conditions (23)

$$\left(\zeta_1\frac{\partial\nu}{\partial\vartheta}+\zeta_2\mu_\varphi\frac{\partial\nu}{\partial\varphi}\right)\Big|_\Sigma = 0. \tag{26}$$

Next, we consider the following particular cases of condition (26):

(i) $\zeta_1 = \chi_1 = \text{const}$, $\zeta_2\mu_\varphi = \chi_2 = \text{const}$, $\mu_\varphi(r,\varphi)\neq 0$;

(ii) $\zeta_1 = \chi_1\kappa(r,\varphi)$, $\chi_1 = \text{const}$, $\zeta_2\mu_\varphi = \chi_2\kappa(r,\varphi)$, $\chi_2 = \text{const}$, $\kappa(r,\varphi)\neq 0$;

(iii) $\zeta_1 = \chi_1\mu_\varphi(r,\varphi)$, $\chi_1 = \text{const}$, $\zeta_2 = \chi_2 = \text{const}$.

In each of these cases, this condition is transformed to the form

$$\chi_1\frac{\partial\nu}{\partial\vartheta}+\chi_2\frac{\partial\nu}{\partial\varphi} = 0, \quad \vartheta = \frac{\pi}{2}, \quad r\in(0,+\infty). \quad \varphi\in L. \tag{27}$$

Here, χ_1 and χ_2 are constants. Under the assumptions made above, initial boundary condition (23) is reduced to the form (27), which is analyzed below. We seek the potential w_1 corresponding to the secondary field in form (10):

$$w_1 = \frac{2}{\pi^2}\int_0^{+\infty}\tau\sinh\pi\tau\sum_{m=-\infty}^{+\infty}b_{m\tau}V_{m\tau}^{(1)}\frac{K_{i\tau}(qr)}{\sqrt{r}}d\tau, \tag{28}$$

$$b_{m\tau} = -a_{m\tau}P^m_{-1/2+i\tau}(\cos\vartheta_0), \quad \vartheta_0<\frac{\pi}{2},$$

$$V_{m\tau}^{(1)} = \begin{cases}\displaystyle\sum_{n=-\infty}^{+\infty}\hat{x}_{m,n+m_0}(\tau)\frac{P^{m+nN}_{-1/2+i\tau}(\cos\vartheta)}{P^{m+nN}_{-1/2+i\tau}(0)}e^{i(nN+m)\varphi}, \\ 0<\vartheta<\dfrac{\pi}{2} \\ \displaystyle\sum_{n=-\infty}^{+\infty}\hat{y}_{m,n+m_0}(\tau)\frac{P^{m+nN}_{-1/2+i\tau}(-\cos\vartheta)}{P^{m+nN}_{-1/2+i\tau}(0)}e^{i(nN+m)\varphi}, \\ \dfrac{\pi}{2}<\vartheta<\pi.\end{cases}$$

As a result of the employment of the boundary condition

$$\left[\chi_1\frac{\partial w_1}{\partial\vartheta}+\chi_2\frac{\partial w_1}{\partial\varphi}\right]\Big|_{\vartheta=\pi/2+0}$$
$$= \left[\chi_1\frac{\partial w_1}{\partial\vartheta}+\chi_2\frac{\partial w_1}{\partial\varphi}\right]\Big|_{\vartheta=\pi/2-0}$$
$$= -\left[\chi_1\frac{\partial w}{\partial\vartheta}+\chi_2\frac{\partial w_1}{\partial\varphi}\right]\Big|_{\vartheta=\pi/2} = f(\varphi), \quad \varphi\in L$$

and the condition $w_1|_{\vartheta=\pi/2+0} = w_1|_{\vartheta=\pi/2+0}$, $\varphi\in CL$ for the conjugation in slits, we arrive at the system of equations

$$\chi_1^2 \sum_{n=-\infty}^{+\infty} N(n+\nu)\frac{|n|}{n}(1-\varepsilon_n^{(2)})\widehat{z}_n e^{in\psi}$$

$$-\chi_2^2 \sum_{n=-\infty}^{+\infty} N(n+\nu)\frac{|n|}{n}(1-\varepsilon_n^{(2)})\widehat{z}_n e^{in\psi} = \chi_1 \widehat{f}(\psi), \quad (29)$$

$$|\psi| < \delta,$$

$$\sum_{n=-\infty}^{+\infty} (n+\nu)\widehat{z}_n e^{in\psi} = 0, \quad \delta < |\psi| \le \pi,$$

$$\sum_{n=-\infty}^{+\infty} (-1)^n \widehat{z}_n = 0, \quad \psi = \pi, \quad (30)$$

$$z_n = (-1)^n(\widehat{y}_{m,n} - \widehat{x}_{m,n}).$$

Here, $\widehat{f}$ is the transform of the function f. After introducing the function

$$\Phi(\psi) = i\sum_{n=-\infty}^{+\infty} N(n+\nu)\widehat{z}_n e^{i(n+\nu)\psi},$$

$$\psi \in [-\pi, \pi]$$

and using formulas (19)–(21), we arrive at

$$\frac{\chi_1^2+\chi_2^2}{\pi}\int_S \frac{\Phi(\beta)e^{-i\nu\beta}}{\beta-\psi}d\beta$$

$$+\frac{1}{\pi}\int_S Q_{m\tau}(\beta-\psi)\Phi(\beta)e^{-i\nu\beta}d\beta = \chi_2\widehat{f}(\psi),$$

$$\psi \in S,$$

$$Q_{m\tau}(\theta) = (\chi_1^2+\chi_2^2)\left(\frac{1}{2}\cot\frac{\theta}{2} - \frac{1}{\theta}\right) \quad (31)$$

$$+\frac{1}{2i}\left(\frac{1}{NA_{m\tau}^{\nu}}\chi_1^2 + N^2\nu^2 A_{m\tau}^{\nu}\chi_2^2\right)\left(\frac{\pi}{\sin\pi\nu}e^{i\nu\theta} - \frac{1}{\nu}\right)$$

$$+\frac{1}{2i}(\chi_1^2+\chi_2^2)\sum_{n\neq 0}\frac{1}{N^2(n+\nu)^2}\frac{|n|}{n}e^{-in\theta}$$

$$+\frac{\chi_1^2}{2i}\sum_{n\neq 0}\frac{|n|}{n}\left(\varepsilon_{m,n}^{(2)} - \frac{1}{N^2(n+\nu)^2}\right)e^{-in\theta}$$

$$+\frac{\chi_2^2}{2i}\sum_{n\neq 0}\frac{|n|}{n}\left(\varepsilon_{m,n}^{(1)} - \frac{1}{N^2(n+\nu)^2}\right)e^{-in\theta}.$$

Singular integral equation (31) has the Cauchy kernel, $Q_{\nu\tau}(\theta)$ being the smooth function.

CONCLUSIONS

Thus, as a result of employing Kontorovich–Lebedev integral transformation, the third and fourth boundary value problems of the Helmholtz equation for the three-dimensional array consisting of planar angular strips are reduced to singular integral equations of the first kind with the Cauchy kernel. The unambiguous solvability of singular integral equations (22) and (31) follows from their equivalence to the pair summator equations (13), (14) and (29), (30), respectively, the latter being adequate to the initial boundary value problem. The algorithms developed imply the necessity of numerically solving singular integral equations. The approach can be realized by discretizing singular integral equations and using Gaussian quadratures.

ACKNOWLEDGMENTS

The authors are grateful to Academician V.A. Sadovnichiĭ, Corresponding Member of the RAS V.I. Pustovoĭt, Professor Yu.V. Gandel, and Professor Ya.S. Shifrin for discussing the results of this work.

REFERENCES

1. V. T. Erofeenko and V. F. Kravchenko, Radiotekh. Élektron. **45**, 1 (2000).
2. V. A. Doroshenko and V. F. Kravchenko, Dokl. Akad. Nauk **375**, 611 (2000) [Dokl. Phys. **45**, 659 (2000)].

Translated by G. Merzon

Doklady Physics, Vol. 47, No. 3, 2002, pp. 206–208. Translated from Doklady Akademii Nauk, Vol. 383, No. 3, 2002, pp. 334–336.

TECHNICAL PHYSICS

Propagation of an Acoustic Wave in a Thin Elastic Strip Embedded in a Low-Modulus Matrix

S. L. Bazhenov

Presented by Academician N.F. Bakeev October 31, 2001

Received October 31, 2001

In connection with the practical problem of measuring the elastic modulus for rubber deposited on a metal or glass substrate, we theoretically solve the problem of the propagation of longitudinal acoustic waves in a thin elastic strip-shaped rod embedded in an unbounded bulk low-modulus matrix. The speed of the propagation of acoustic waves in an elastic rod is determined by the density ρ_0 and elastic modulus E of the rod [1]:

$$c = \sqrt{\frac{E}{\rho_0}}. \quad (1)$$

The velocity of longitudinal ultrasonic waves in a thin strip-shaped rod was found to decrease upon dipping the rod into a fluid [2, 3]. This decrease is caused by a boundary layer involved in joint vibrations with the rod. The thickness of the boundary layer depends on the vibration frequency and the density and viscosity of the fluid [4–6]. This effect was used for determining fluid viscosity, and the results of these acoustic measurements are consistent with those obtained by conventional methods [3].

Let the elastic modulus of the strip be much greater than the modulus of the matrix. In this case, according to Eq. (1), the longitudinal-wave velocity in the rod is much higher than that in the matrix. Being in contact with the strip, the boundary layer of the matrix is involved in the motion. It is evident that the matrix motion is of a shear origin and that a longitudinal wave in the strip excites a shear wave in the matrix.

We assume that the strip width significantly exceeds the length of the transverse wave excited in the matrix. Under this assumption and taking into account that a strip element is subjected to the elastic tensile–compressive forces and forces of shearing interaction with the latter caused by the matrix, one can describe the longitudinal vibrations of the strip by the equation

$$\rho_0 h\frac{\partial^2 u}{\partial t^2} = Eh\frac{\partial^2 u}{\partial y^2} + 2\tau. \quad (2)$$

Institute of Synthetic Polymeric Materials, Russian Academy of Sciences, Profsoyuznaya ul. 70, Moscow, 117393 Russia

Here, u is the displacement of the strip element from its equilibrium position, h is the strip thickness, τ is the shear stress at the rubber–strip interface, and y is the strip axis along which the acoustic wave propagates. The factor 2 corresponds to the two strip–matrix interfaces.

To determine the quantity τ, we consider the shear vibrations of the matrix in the elastic half-plane $x > 0$. These vibrations are described by the equation [1]

$$\rho\frac{\partial^2 u}{\partial t^2} = G\frac{\partial^2 u}{\partial x^2}. \quad (3)$$

Here, ρ and G are the density and shear modulus of the matrix, respectively, and x is the axis perpendicular to the strip plane.

The boundary conditions are determined by the requirement that displacements of the matrix at the $x = 0$ interface are equal to those of the strip. We seek a solution of Eq. (3) in the form of a traveling wave:

$$u = u_0\exp[-i(\omega t - k_\perp x)], \quad (4)$$

where $k_\perp$ is the wave number of a transverse wave in the matrix and ω is the angular frequency of the strip vibrations. Substituting Eq. (4) into Eq. (3), we have

$$k_\perp = \omega\sqrt{\frac{\rho}{G}}. \quad (5)$$

The length of the transverse wave in the matrix is given by the formula

$$\lambda_\perp = \frac{1}{f}\sqrt{\frac{G}{\rho}},$$

where $f = \omega/2\pi$ is the vibration frequency. For G = 1 MPa and $\rho = 10^3$ kg/m^3, which are typical values for rubber, f = 250 kHz, and the transverse wave length is estimated as 125 μm.

1028-3358/02/4703-0206$22.00

Stress in the matrix at the strip–matrix interface is defined as $G\frac{\partial u}{\partial x}$ at $x = 0$ and is equal to

$$\tau = iGk_{\perp}u. \quad (6)$$

We seek a solution of Eq. (2) in the form

$$u = u_0\exp[-i(\omega t - k_{\parallel}y)], \quad (7)$$

where $k_{\parallel}$ is the wave number.

Assuming that the longitudinal wavelength in the rod is much greater than the transverse wavelength in rubber, and substituting Eqs. (6) and (7) into Eq. (2), we obtain the following expression for the wave number of the longitudinal wave in the rod:

$$k_{\parallel} = \frac{\omega}{c_0}\sqrt[4]{1 + \frac{\rho^2\lambda_{\perp}^2}{\pi^2\rho_0^2h^2}}e^{i\varphi}, \quad (8)$$

where c_0 is the speed of sound in the rod and $\varphi = \frac{1}{2}\arctan\frac{\rho\lambda_{\perp}}{\pi\rho_0 h}$.

The phase velocity of the longitudinal wave is equal to $\omega/k_{\parallel}$. Using the equality $\lambda_{\perp} = 2\pi/k_{\perp}$ and taking Eq. (5) into account, we obtain the following expression for the phase velocity of the longitudinal wave:

$$c = \frac{c_0}{\sqrt[4]{1 + \frac{\rho G}{\pi^2 f^2\rho_0^2h^2}}}. \quad (9)$$

When $\lambda_{\perp} \ll h$, the second term in the radicand is much less than unity. Retaining the first two terms in the expansion of Eq. (9) in a power series of this term, we have the relation

$$c = c_0\left(1 - \frac{\rho G}{4\pi^2 f^2\rho_0^2h^2}\right), \quad (10)$$

which can be written in the form

$$c = c_0\left(1 - \frac{m_1^2}{4\pi^2 m_0^2}\right), \quad (11)$$

where $m_1 = \rho\lambda_{\perp}$ and $m_0 = \rho_0 h$ are the masses of the boundary layer and strip, respectively.

The complex-valued component of the wave number determines wave damping. It is easy to prove that the inequality $\lambda_{\perp} \ll h$ is satisfied for $\varphi \ll 1$. In this case,

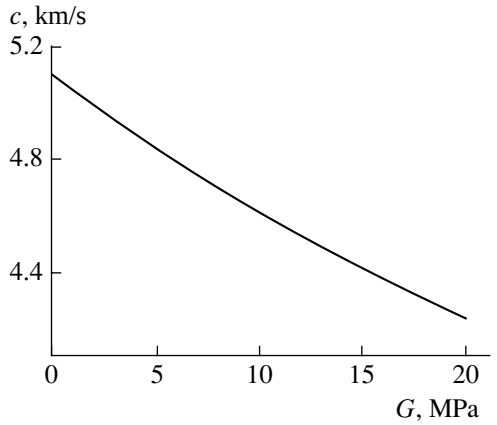

Fig. 1. Speed of sound vs. the shear modulus G. The calculations were carried out for the strip thickness $h = 0.1$ mm, $c_0 = 5.1$ km/s, vibration frequency $f = 250$ kHz, $\rho_0 = 2.6$ g/cm^3, and $\rho = 0.93$ g/cm^3.

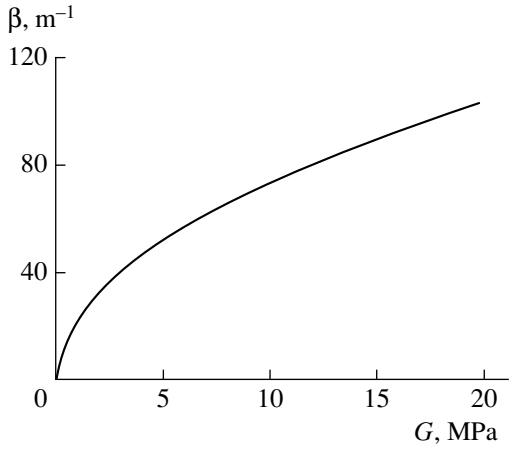

Fig. 2. The same as in Fig. 1, but for the damping coefficient.

the amplitude of the longitudinal wave in the strip is given by the relationship

$$u = u_0\exp(-\beta y), \quad (12)$$

where $\beta = \frac{\sqrt{G\rho}}{\rho_0 c_0 h}$ is the damping coefficient for the longitudinal wave. It is worth noting that the coefficient β is equal to the ratio m_1/m_0 of the boundary-layer mass to the strip mass. If the wave damping factor is small, the coefficient β can be considered as a small parameter. In this case, the decrease in velocity is a second-order correction in the damping coefficient.

The results calculated by Eq. (9) for the velocity of the propagation of acoustic waves are shown in Fig. 1 as a function of the matrix shear modulus G. The velocity of sound decreases monotonically with the increasing shear modulus of the matrix. A similar dependence for the damping coefficient is presented in Fig. 2. In the case of the matrices with small coefficients of stiff-

ness, the damping coefficient increases very rapidly as $\beta \propto \sqrt{G}$.

Thus, the results of embedding a thin strip in a low-modulus matrix are similar to the results of the immersion of the strip into a fluid [4–6]. Namely, longitudinal vibrations of the strip excite a transverse wave in the matrix. There is also an inverse effect, which becomes substantial when the strip mass is commensurable with the mass of the matrix boundary layer. Because of the presence of the matrix, the longitudinal wave is damped and its velocity decreases.

REFERENCES

1. L. D. Landau and E. M. Lifshitz, *Theory of Elasticity* (Nauka, Moscow, 1986; Pergamon, Oxford, 1986).
2. A. K. Rogozinskiĭ, S. L. Bazhenov, and A. A. Berlin, Dokl. Akad. Nauk **362**, 618 (1998) [Dokl. Phys. **43**, 623 (1998)].
3. A. K. Rogozinskiĭ, S. L. Bazhenov, and A. A. Berlin, Dokl. Akad. Nauk **362**, 481 (1998) [Dokl. Phys. **43**, 616 (1998)].
4. L. D. Landau and E. M. Lifshitz, *Fluid Mechanics* (Nauka, Moscow, 1988; Pergamon, Oxford, 1987).
5. V. A. Krasil'nikov and V. V. Krylov, *Introduction to Physical Acoustics* (Nauka, Moscow, 1984).
6. L. F. Lependin, *Acoustics* (Vysshaya Shkola, Moscow, 1978).

Translated by V. Chechin

Doklady Physics, Vol. 47, No. 3, 2002, pp. 209–214. Translated from Doklady Akademii Nauk, Vol. 383, No. 3, 2002, pp. 337–342.

TECHNICAL PHYSICS

A New Class of Self-Similar Antenna Arrays

V. F. Kravchenko* and M. A. Basarab**

Presented by Academician V.A. Sadovnichiĭ October 25, 2001

Received November 6, 2001

INTRODUCTION

Currently, new approaches in the analysis and synthesis of antenna systems, which are based on concepts of fractal geometry, have received wide recognition [1–8]. As is well known, the simplest mathematical abstraction for a self-similar set is a Cantor set (dust is an analog) [9–12]. On this basis, one-dimensional and two-dimensional antenna radiators were developed and their properties were thoroughly investigated [6, 7].

In the present study, a new class of self-similar sets based on a simple recurrence procedure is considered. In this case, terms of the sequence being formed alternate in accordance with the distribution law for signs of derivatives of certain atomic functions (AF) [13]. These functions are finite solutions to functional differential equations relating shifts and compressions of such functions to their derivatives. Note that atomic functions turn out similar to linear combinations of their derivatives. Therefore, their multiple differentiation makes it possible to design a new type of self-similar antenna arrays.

THE $h_a(x)$ FAMILY OF ATOMIC FUNCTIONS

Atomic functions are finite solutions to linear functional differential equations with constant coefficients

$$\sum_{n=1}^{N} d_n y^{(n)}(x) = \sum_{m=1}^{M} c_m y(ax - b_m).$$

Here, a, d_n, c_m, and b_m are numerical parameters, and $|a| > 1$. One of the basic classes of atomic functions is determined by the following expression:

$$\frac{2y'(x)}{a^2} = y(ax+1) - y(ax-1). \qquad (1)$$

Solutions (1) for the function $h_a(x)$ are determined on the carrier $[-(a-1)^{-1}, (a-1)^{-1}]$, and their Fourier transforms have the form:

$$F_a(p) = \prod_{k=1}^{\infty} \operatorname{sinc}(pa^{-k}),$$

where $\operatorname{sinc}(x) \equiv \dfrac{\sin x}{x}$. The derivatives of the nth order can be expressed in terms of the function $h_a(x)$ in itself as

$$h_a^{(n)}(x) = 2^{-n} a^{\frac{n(n+3)}{2}} \times \sum_{k=1}^{2^n} \delta_k h_a\left(a^n x + \sum_{j=1}^{n} a^{j-1}(-1)^{p_j(k-1)}\right), \qquad (2)$$

where

$$\delta_1 = 1, \quad \delta_{2k} = -\delta_k, \quad \delta_{2k-1} = \delta_k, \quad k = 1, 2, \ldots. \qquad (3)$$

Here, $p_j(k)$ denotes the jth bit in the binary representation of the number k; i.e., $p_j(k) = [k \times 2^j] \bmod 2$. For $a = 2$, we obtain the simplest atomic function $\mathrm{up}(x)$ with the carrier $(-1, 1)$, which satisfies the equation

$$\frac{y'(x)}{2} = y(2x+1) - y(2x-1).$$

Expression (2) for the derivatives of $\mathrm{up}(x)$ has the form

$$\mathrm{up}^{(n)}(x) = 2^{n(n+1)/2} \sum_{k=1}^{2^n} \delta_k \mathrm{up}(2^n x + 2^n + 1 - 2k).$$

In Fig. 1, plots are presented for the function $\mathrm{up}(x)$, its first two derivatives, and the Fourier transform as well. As is seen from Figs. 1b and 1c, the derivatives consist of equal parts, similar to the function itself in the shift–compression sense. In addition, in each of these segments, the derivatives have a sign determined by the recurrence sequence (3).

DESIGN OF A SELF-SIMILAR ANTENNA ARRAY

Certain questions associated with the application of atomic functions in problems of antenna-array synthe-

* *Institute of Radio Engineering and Electronics, Russian Academy of Sciences, Mokhovaya ul. 18, Moscow, 103907 Russia*

** *Bauman Moscow State Technical University, Vtoraya Baumanskaya ul. 5, Moscow, 107005 Russia*

1028-3358/02/4703-0209$22.00

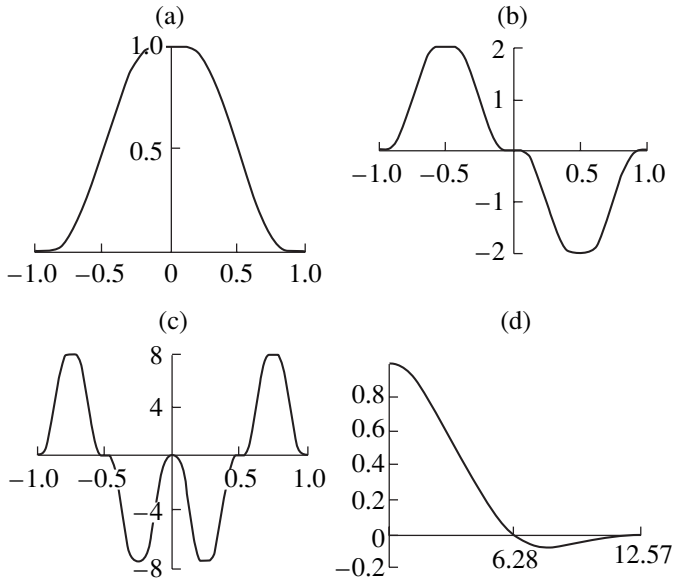

Fig. 1. (a) Atomic function up(x), (b) its first derivative, and (c) second derivatives; as well as (d) the Fourier transform.

sis are considered in [1–4]. In the present study, we use an original approach for creating a non-Cantor antenna array of a new type. This array is based on the employment of generating sequence (3). It is well known that the multiplier of a linear equidistant array is represented in the form [14]

$$AF(\psi) = \begin{cases} I_0 + 2\sum_{n=1}^{N} I_n \cos(n\psi) & \text{for } 2N+1 \text{ element} \\ 2\sum_{n=1}^{N} I_n \cos\left[\left(n-\frac{1}{2}\right)\psi\right] & \text{for } 2N \text{ elements.} \end{cases} \quad (4)$$

Here, $\psi = kd(\cos\theta - \cos\theta_0)$, $k = \frac{2\pi}{\lambda}$, and d is the distance between array elements. Let certain of them be switched off or removed so that

$$I_n = \begin{cases} 1 & \text{if the element is switched on} \\ 0 & \text{if the element is switched off.} \end{cases}$$

As a result, a nonequidistant equal-amplitude line of discrete radiators is formed.

The simplest scheme (based on the Cantor-set concept) for constructing a fractal array is analyzed in [5]. The 101 equidistant generating sequence consisting of three elements (with the central one switched off) is considered as an initial sequence. The triad Cantor array is obtained recursively by the sequential exchange of unity by 101 and zero by 000 at each design stage [6]. Possible generalizations of Cantor radiators (two-scale arrays) and methods for improving their characteristics are considered in [7].

We now investigate one possible design of a self-similar antenna array. Assuming the number of its elements to be even, we use the relationship $I_n = \frac{\delta_n + 1}{2}$ as a law for the electric-current distribution, where δ_n are recursively determined from relationships (3). Let $N = 4^k$. Then, the expression for the multiplier of array (3) can be written out in the form

$$AF_k(\psi) = \sum_{n=1}^{N} (\delta_n + 1)\cos\left[\left(n-\frac{1}{2}\right)\psi\right]. \quad (5)$$

It is evident that $\delta_{N-i+1} = \delta_i$ and $\delta_{N/2-i+1} = -\delta_i$. Thus, it can be shown that the preceding relationship has a simpler form

$$AF_k(\psi) = 4\cos\left(\frac{N\psi}{2}\right)\sum_{n=1}^{N/4} \cos\left[\left(2n-1+\frac{\delta_n}{2}\right)\psi\right]. \quad (6)$$

The number of arithmetic operations needed for finding AF_k in accordance with formula (6) is less than in the case of employing formula (5) by a factor of four. We now denote $b_n \circ b_{n-1}$ the concatenation of two finite sequences b_n and b_{n-1}, where n is the recursion index.

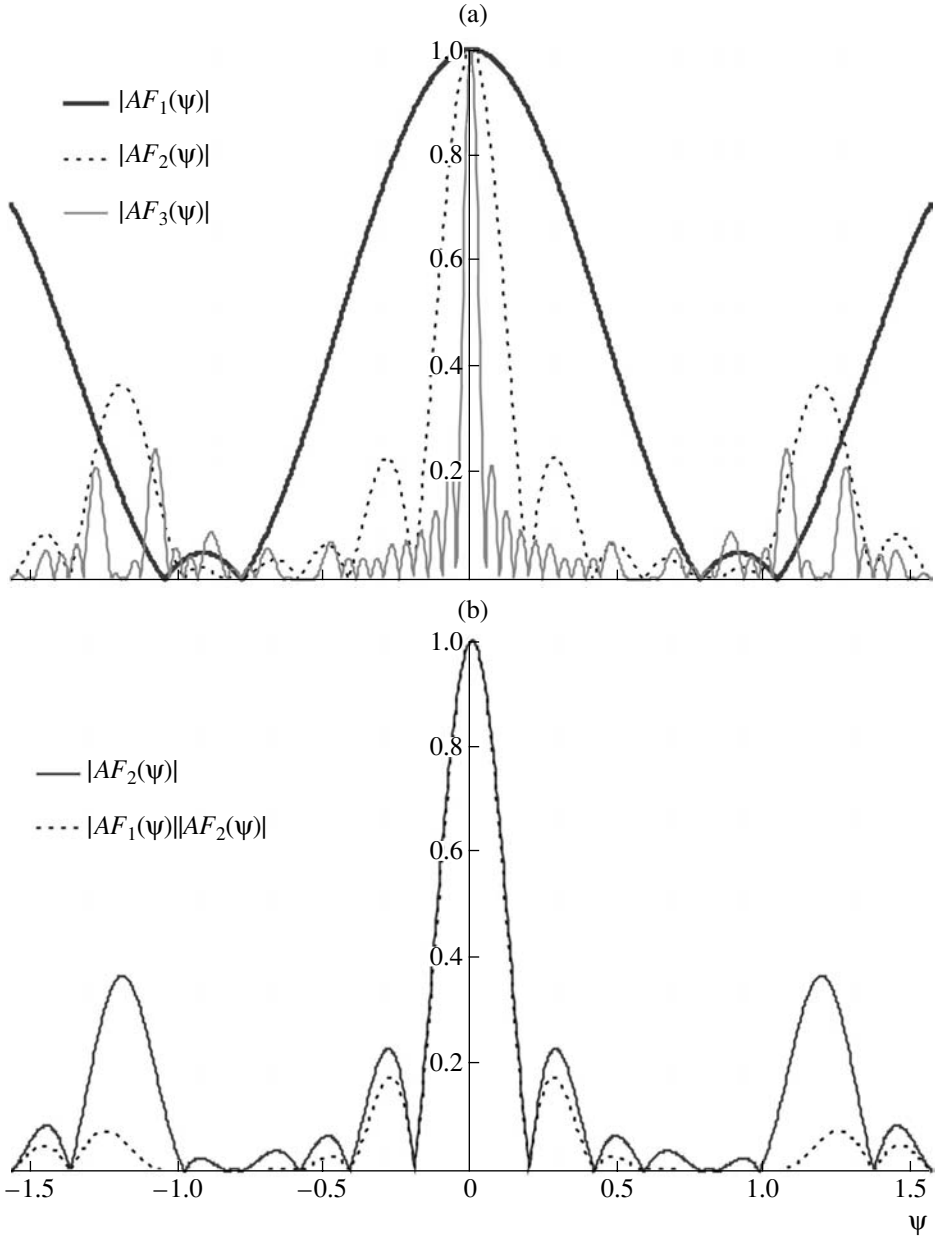

Fig. 2. (a) Moduli of the antenna-array multiplier for the first three stages of construction, $k = 1, 2, 3$, and (b) multipliers for an array of the second level (solid line) and combined array (dashed line) formed by the convolution of arrays of the first and second levels.

Then, the following recurrence formula for the ordered set of included (1) and excluded (0) array elements takes place:

$$F_0 = 1, \quad F_n = F_{n-1} \circ \bar{F}_{n-1}, \quad n = 1, 2, \ldots. \quad (7)$$

Here, the bar from above denotes the logical negation. The desired current distribution has the form $I = F_{2n} \circ F_{2n}$, $n = 0, 1, \ldots$. Thus, we have obtained the following algorithm for constructing a discrete radiator line. Beginning from the initial sequence 11, we should substitute 1001 instead of 1 and 0110 instead of 0. In particular, at the second step, we have 10011001.

It is of interest to compare expression (7) with the Fibonacci sequence

$$F_0 = 1, \quad F_1 = 0, \quad F_n = F_{n-1} \circ F_{n-2},$$
$$n = 2, 3, \ldots,$$

which is formed from the initial unity by the recurrent exchange 1 by 10 and 0 by 1.

We consider a number of properties for the new array. Furthermore, we use the normalized expression

$$AF_k(\psi) = \frac{4}{N}\cos\left(\frac{N\psi}{2}\right)\sum_{n=1}^{N/4}\cos\left[\left(2n - 1 + \frac{\delta_n}{2}\right)\psi\right] \quad (8)$$

instead of (6).

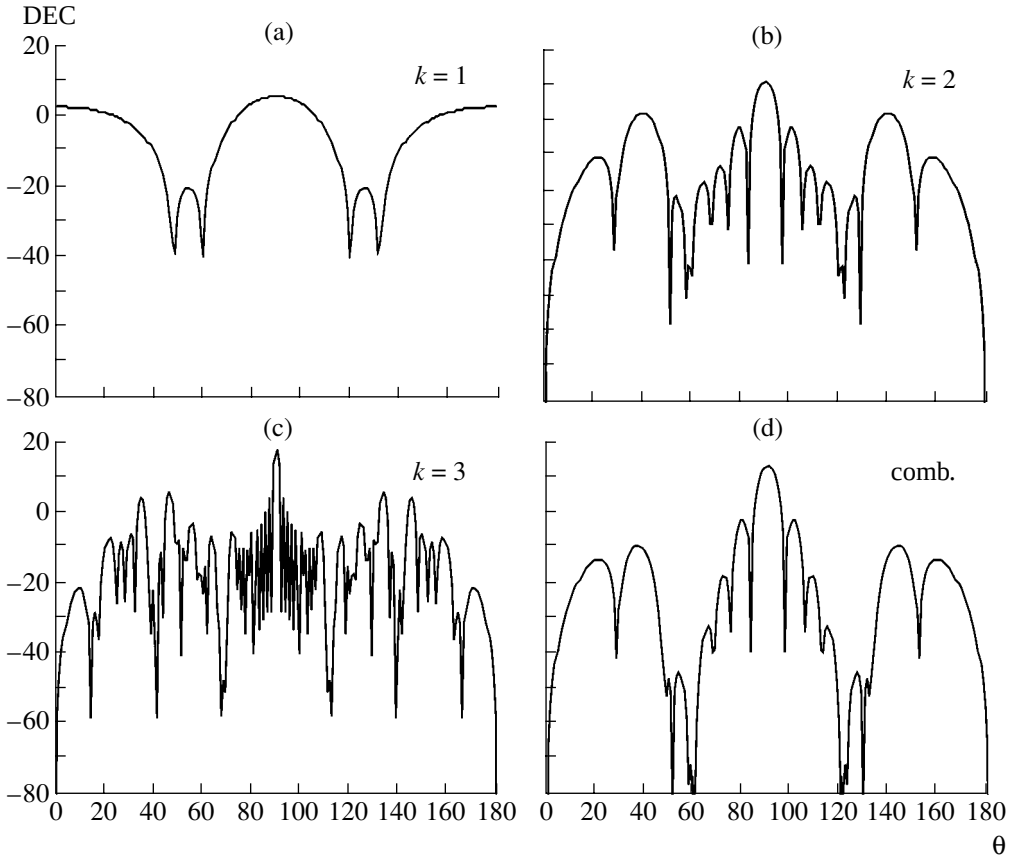

Fig. 3. Directional-effect coefficients (DEC) as functions of the angle θ for (a) $k = 1$, (b) 2, and (c) 3, and (d) DEC for the combined array formed by the convolution of arrays of the first and second levels.

In Fig. 2, we show the results for the multiplier (8), which are obtained at the three first stages of designing the array. Let the distance between its three elements be a quarter of the wavelength; i.e., $d = \frac{\lambda}{4}$. In this case, for $\theta_0 = 90°$, we arrive at the following expression for the array directional-effect coefficient (DEC):

$$D_k(u) = 2\frac{AF_k^2(\psi)}{\int_{-1}^{1} AF_k^2(\psi)du},$$

where $\psi = \pi u/2$ and $u = \cos\theta$. The maximum value of this coefficient corresponds to $u = 0$. It turns out that in the asymptotic limit, $D_k(0) \underset{k\to\infty}{\approx} 4D_{k-1}(0)$. The values of the DEC are presented for $k = 1, \ldots, 5$ in the following table:

k	1	2	3	4	5
$D_k(0)$	3.771	13.258	52.282	208.422	832.983

Plots of the DEC for $k = 1, 2, 3$ are shown in Figs. 3a, 3b, and 3c.

We now consider the procedure of constructing a combined two-scale array [7], which is defined as a convolution of two arrays with a different number of elements $N_1 = 4^k$ and $N_2 = 4^l$. In this case, the array multiplier is a product of the multipliers corresponding to initial radiators $AF_{k,l}(\psi) = AF_k(\psi)AF_l(\psi)$. This combination makes it possible to optimize the array design from the standpoint of decreasing the level of side lobes. Figure 2b exhibits moduli of the multipliers for the initial array of the second level ($N_1 = 16$) and an array represented as a convolution of two sequences for two linear discrete radiators of the second and first ($N_2 = 4$) levels. The directional-effect coefficient of the resulting array is shown in Fig. 3d.

A TWO-DIMENSIONAL ARRAY

The Sierpinski carpet is a generalization of the Cantor set to the two-dimensional case. In [6], problems are analyzed associated with constructing a fractal antenna array based on the Sierpinski carpet. In our case, the process of constructing a plane system of discrete radiators is quite similar. We take the matrix $\begin{bmatrix} 1 & 1 \\ 1 & 1 \end{bmatrix}$ as an ini-

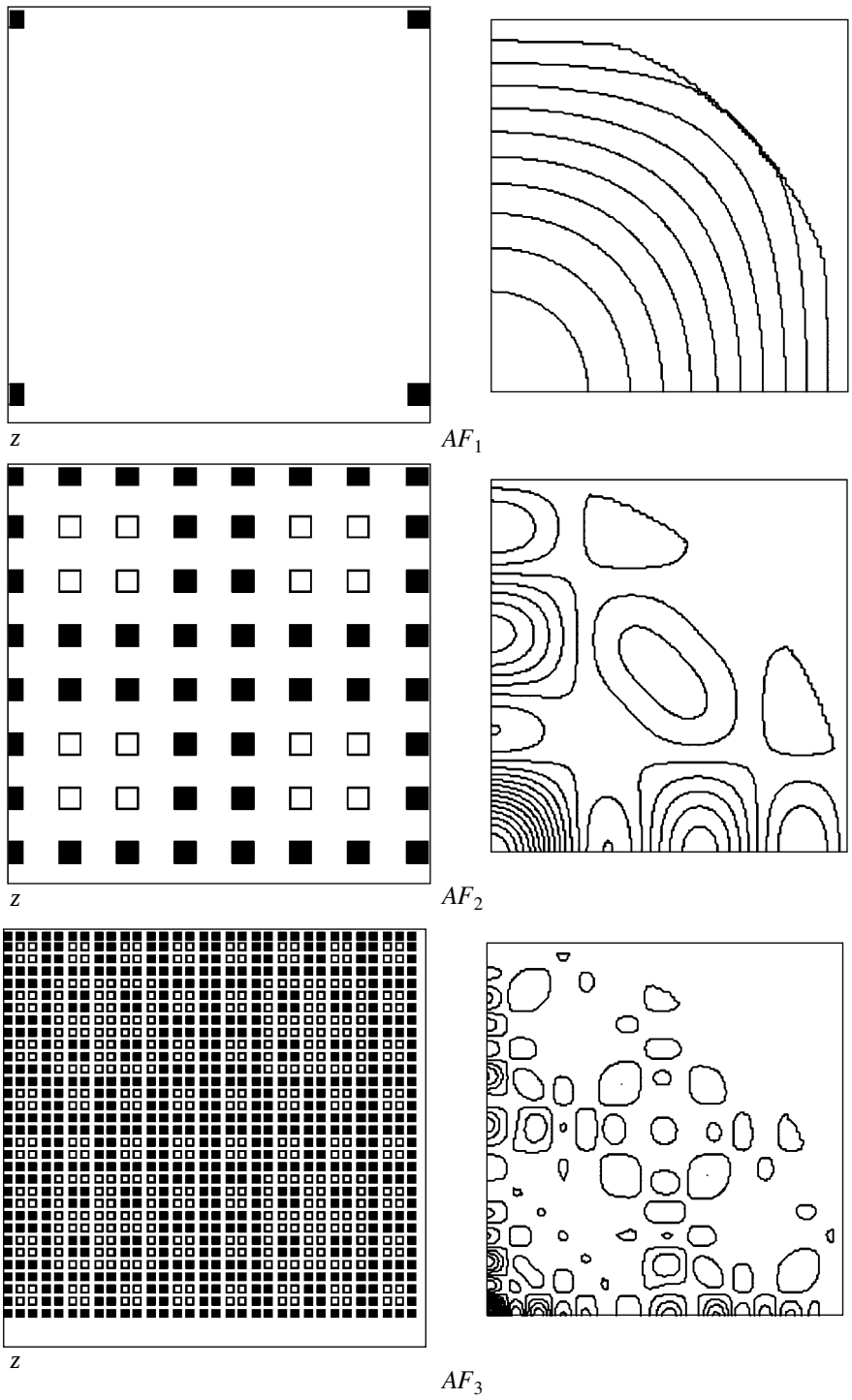

Fig. 4. Two-dimensional antenna arrays and their corresponding multipliers for the three first construction stages.

tial sequence and then sequentially change each 1 or 0 by

$$\begin{bmatrix} 1 & 1 & 1 & 1 \\ 1 & 0 & 0 & 1 \\ 1 & 0 & 0 & 1 \\ 1 & 1 & 1 & 1 \end{bmatrix} \text{ or } \begin{bmatrix} 0 & 0 & 0 & 0 \\ 0 & 1 & 1 & 0 \\ 0 & 1 & 1 & 0 \\ 0 & 0 & 0 & 0 \end{bmatrix},$$

respectively. The expression for the array multiplier takes the form

$$AF_k(\psi_1, \psi_2) = \sum_{m=-N+1}^{N} \sum_{n=-N+1}^{N} I_{m,n} \times \exp\left[i\left(m - \frac{1}{2}\right)\psi_1 + \left(n - \frac{1}{2}\right)\psi_2 \right],$$

where $N = 4^k$. In Fig. 4 (on the right), we demonstrate the general view of two-dimensional arrays (discrete radiators are situated in the center of black squares). On the left, their multipliers are displayed as functions of angles ψ_1 and ψ_2, which vary within the limits from 0 to π.

Thus, in the present study, a new approach associated with the concept of atomic functions is proposed for constructing one-dimensional and two-dimensional antenna arrays. The construction is based on the recurrence procedures; however, in contrast to the traditional Cantor sets it cannot be called fractal. It is easy to verify that the new type of array is based on the Hausdorff–Besikovich sets of unit dimensionality [8]. In spite of this fact, these arrays possess self-similar properties, which allows us to considerably simplify the analysis of their properties and characteristics. Possible generalizations of the arrays proposed, such as combined two-scale ones and two-dimensional discrete radiators, are also considered.

ACKNOWLEDGMENTS

The authors are grateful to Academician V.A. Sadovnichiĭ, Academician of the National Academy of Sciences of the Ukraine V.L. Rvachev, and Corresponding Member of the RAS V.I. Pustovoĭt for discussing the results of this work.

REFERENCES

1. V. F. Kravchenko, A. A. Potapov, and V. M. Masyuk, Zarub. Radioélektron. Usp. Sovrem. Radioélektron., No. 6, 4 (2001).
2. V. F. Kravchenko and A. A. Potapov, in *Proc. of the URSI Intern. Symp. on Electromagn. Theory, Victoria, 2001*, p. 660.
3. V. F. Kravchenko and A. A. Potapov, in *Proc. of the IV Intern. Symp. on Physics and Engineering of Millimeter and Sub-Millimeter Waves, Kharkov, Ukraine, 2001*, Vol. 1, p. 102.
4. M. A. Basarab, V. F. Kravchenko, and V. M. Masyuk, Zarub. Radioélektron. Usp. Sovrem. Radioélektron., No. 8, 5 (2001).
5. H. P. Peitgen, H. Jurgens, and D. Saupe, *Chaos and Fractals: New Frontiers of Science* (Springer, New York, 1992).
6. D. H. Werner, R. L. Haupt, and P. L. Werner, IEEE Antennas and Propag. Mag. **41**, 37 (1999).
7. S. E. El-Khamy and M. I. Elkashlan, in *Proc. of the URSI Int. Symp. on Electromag. Theory, Victoria, 2001*, p. 16.
8. B. B. Mandelbrot, *The Fractal Geometry of Nature* (Freeman, San Francisco, 1983).
9. A. V. Arkhangel'skiĭ, *Theory of Cantor Sets* (Mosk. Gos. Univ., Moscow, 1988).
10. M. Schroeder, *Fractals, Chaos, Power Laws: Minutes from an Infinite Paradise* (Freeman, New York, 1990).
11. J. L. McCauley, *Chaos, Dynamics, and Fractals: An Algorithmic Approach to Deterministic Chaos* (Cambridge Univ. Press, Cambridge, 1995).
12. A. N. Kolmogorov and S. V. Fomin, *Elements of the Theory of Functions and Functional Analysis* (Nauka, Moscow, 1981; Vol. 1, Graylock Press, Rochester, New York, 1957; and Vol. 2, Graylock Press, Albany, New York, 1961).
13. E. G. Zelkin and V. F. Kravchenko, Radiotekh. Électron. **46**, 903 (2001).
14. W. L. Stutzman and G. A. Thiele, *Antenna Theory and Design* (Wiley, New York, 1981).
15. M. A. Basarab and V. F. Kravchenko, Élektromag. Volny i Élektron. Sistemy **6**, 31 (2001).

Translated by G. Merzon

Doklady Physics, Vol. 47, No. 3, 2002, pp. 215–218. Translated from Doklady Akademii Nauk, Vol. 383, No. 2, 2002, pp. 194–197.

ENERGETICS

Acoustic Instability while Combusting Aluminum Particles in MHD Facilities

V. R. Pesochin

Presented by Academician V.E. Fortov September 26, 2001

Received October 5, 2001

In this paper, the theoretical study of acoustic-vibration excitation while combusting aluminum particles in a gas mixture is carried out. At long distances, aluminum particles are considered to be monodisperse and immobile with respect to the gas. In determining the excitation conditions for acoustic vibrations, the gas mixture used was considered as a perfect gas. Expressions for the frequency and excitation increment of acoustic vibrations are obtained, characteristics of a fuel and of an oxidizer explicitly entering into these expressions.

In [1], powders prepared on the basis of carbon and metals were suggested as a fuel for pulsed MHD generators. Air or oxygen are oxidizers in this case. Characteristics of MHD generators while operating with these fuels, in fact, do not differ from those obtained using solid rocket propellants. In this case, the powder-like fuel presents the possibility for profound control of the device power when changing the mass flow-rate of components and provides for long-term operation of powerful MHD generators. It was shown in [2] that aluminum fuel is optimal for pulsed MHD generators, provided that the air oxidizer is employed.

It is known [3] that in the process of burning a disperse fuel the acoustic vibrations can be excited, which results in violation of the normal operation of combustion chambers and even in their destruction. In the practice of rocket-engine development [4], engines having pressure-vibration amplitudes of not more than 5% from the nominal value are related to those exhibiting stable combustion. It was shown in [5] that the requirements for stability of the combustion process in the MHD-generator combustion chamber should be more rigorous than in rocket engines. This is caused by the fact that for such pressure vibrations electric-power pulsation phenomena hinder the normal operation of an MHD generator. Therefore, consideration of acoustic-vibration excitations in the case of combusting a powder-like fuel in the combustion camber of an MHD generator is an urgent problem.

Usually, in studies of acoustic-vibration excitation, it is suggested that, in the case of combusting a disperse fuel, the burning zone is substantially smaller than the length of the combustion chamber [3, 4]. In actual conditions, the burning zone has a certain extension along the longitudinal axis of the combustion chamber, which is comparable with its length [6]. Therefore, in the case of acoustic vibrations of pressure, disturbances of the velocity and temperature of the gas mixture along the length of the combustion chamber are different, which affects the stability of the combustion process [3, 4]. In this paper, in studies of the excitation of acoustic vibrations, a distributed combustion model is used. In other words, we assume that the zone of burning aluminum particles is approximately equal to the length of the combustion chamber.

Here, in calculations of the burning process in a forward-flow combustion chamber, the aluminum particles are considered to be monodisperse and immobile with respect to the gas mixture. It is assumed that the particle combustion occurs in the vapor-phase diffusion regime. The specific heat c_p and the adiabatic index γ of the gas mixture were assumed to be constant and independent of its temperature and component concentrations. The flow in the combustion chamber was assumed to be one-dimensional under complete mixing in the transverse direction and in the absence of mixing in the longitudinal direction. Such assumptions are common in calculations of the design of combustion chambers [6]. While analyzing acoustic vibrations, the gas mixture was considered as a perfect gas, and the presence of a disperse phase in it was ignored.

Under these assumptions, the continuity equation, the equation of motion, and the energy equation can be written in the form

$$\frac{\partial \rho}{\partial t} + \frac{\partial}{\partial x}(\rho u) = -\frac{3}{4}\frac{M_1}{M}W, \tag{1}$$

$$\frac{\partial u}{\partial t} + u\frac{\partial u}{\partial x} = -\frac{1}{\rho}\frac{\partial p}{\partial x}, \tag{2}$$

Institute of High-Energy Densities,
Joint Institute for High Temperatures,
Russian Academy of Sciences,
ul. Fadeeva 6, Moscow, 125047 Russia

1028-3358/02/4703-0215$22.00

$$\rho c_p\left(\frac{\partial T}{\partial t} + u\frac{\partial T}{\partial x}\right) = \frac{Q}{4M}W + \frac{\partial p}{\partial t}, \quad (3)$$

where W is the combustion rate for aluminum particles in the volume unit, Q is the thermal effect of the reaction of the aluminum oxidation, and M and M_1 are the atomic and molecular masses of aluminum and oxygen, respectively.

Below, we consider that a local thermodynamic equilibrium is conserved in the gas phase. This assumption is common in studies of the excitation of acoustic vibrations in combustion chambers [3]. Then, we can write the equation of state for the gas mixture

$$\rho = \rho(p, T). \quad (4)$$

It is known [3, 4] that high-frequency acoustic vibrations are the most dangerous and difficult for elimination. As follows from [3], they are characterized by the fact that for them, the parameter $\mathrm{Sh} \gg 1$. Here, $\mathrm{Sh} = \omega l/u$, ω is the angular frequency, and l is the chamber length. Thus, linearizing equations (1)–(3) with allowance for $\mathrm{Sh} \gg 1$, we arrive at

$$\frac{\partial \rho'}{\partial t} + \rho\frac{\partial u'}{\partial x} + u'\frac{\partial \rho}{\partial x} = -\frac{3}{4}\frac{M_1}{M}W', \quad (5)$$

$$\frac{\partial u'}{\partial t} = -\frac{1}{\rho}\frac{\partial p'}{\partial x}, \quad (6)$$

$$\rho c_p\left(\frac{\partial T'}{\partial t} + u'\frac{\partial T}{\partial x}\right) = \frac{Q}{4M}W' + \frac{\partial p'}{\partial t}. \quad (7)$$

Here and below, the perturbations are indicated by primes.

Linearizing (4), we obtain a thermodynamic connection between perturbations of p, ρ, and T.

$$\frac{\rho'}{\rho} = \frac{p'}{\rho a_T^2} - \frac{T'}{T}. \quad (8)$$

Here, a_T is the isothermal sound velocity.

Substituting expression (8) into Eq. (5) with account of (7), we obtain

$$\frac{1}{\gamma}\frac{\partial}{\partial t}\left(\frac{p'}{p}\right) + \frac{u'}{T}\frac{\partial T}{\partial x} + \frac{\partial u'}{\partial x} + \frac{u'}{\rho}\frac{\partial \rho}{\partial x} = \frac{QW'}{4M\rho c_p T}.$$

Then, using the relation

$$\frac{\partial \rho}{\partial x} = -\frac{\rho}{T}\frac{\partial T}{\partial x},$$

we write out the last equation in the form

$$\frac{1}{\gamma}\frac{\partial}{\partial t}\left(\frac{p'}{p}\right) + \frac{\partial u'}{\partial x} = \frac{QW'}{4M\rho c_p T}. \quad (9)$$

Differentiating Eq. (6) with respect to x and Eq. (9) with respect to t, and excluding u', we find

$$\frac{\partial^2}{\partial x^2}\left(\frac{p'}{p}\right) = \frac{1}{a_s^2}\frac{\partial^2}{\partial t^2}\left(\frac{p'}{p}\right) - \frac{\gamma Q}{4M\rho c_p T a_s^2}\frac{\partial W'}{\partial t}, \quad (10)$$

where a_s is the adiabatic sound velocity.

To solve the last equation, it is necessary to obtain the expression for W'. As a rule, for description of the combustion of metal particles, the combustion theory for drops of a liquid fuel complemented with the allowance for the formation of condensed products (oxides) is used [7]. It is considered that in the diffusion vapor-phase model of combusting metal particles, as in the combustion theory of liquid-fuel drops, chemical transformations including the formation of condensed combustion products (oxides) occur in a narrow zone above the particle surface. This theory leads to a satisfactory agreement for the calculated time of combusting a metal particle with the experimental data in the low pressure zone ($p < 30$ atm). In the zone of high pressures characteristic for the conditions in the combustion chamber of a pulsed MHD generator, a noticeable discrepancy with the vapor-phase diffusion model is observed. The combustion time for an aluminum particle becomes proportional to $r_0^{3/2}$ but not to r_0^2 (the Sreznevskiĭ law). Here, r_0 is the initial radius of a particle. This is associated with the fact that, in the case of high pressures, the liquid aluminum oxide is accumulated at the surface of a particle, thus hampering its evaporation. At the present time, there is no theoretical model of the vapor-phase combustion of aluminum particles with allowance for the accumulation of the oxide at their surfaces. Therefore, in this paper, an empirical time dependence for the size of a burning particle is employed [7]:

$$r^{3/2} = r_0^{3/2} - \alpha c t. \quad (11)$$

Here, α is an empirical constant and c is the dimensionless mass concentration of oxygen far away from the burning particle.

For combustion of a monodisperse system of aluminum particles in the combustion chamber of a pulsed MHD generator, there exists a correlation between the particle sizes and oxygen concentration:

$$(r/r_0)^3 = c/c_0,$$

where c_0 is the initial dimensionless mass concentration of oxygen.

Differentiating (11) with respect to t and substituting the last relation into the equation obtained, we have

$$\frac{3}{2}r_0^3 r^{-5/2}\frac{dr}{dt} = -\alpha c_0. \quad (12)$$

The initial condition is $r = r_0$ for $t = 0$.

The solution to this equation has the form

$$\left(\frac{r}{r_0}\right)^{3/2} = \frac{1}{1 + \alpha c_0 t / r_0^{3/2}}. \quad (13)$$

The number of particles N per volume unit of the combustion chamber is determined from the balance equation

$$N = N_0 \frac{T_0}{T} = \frac{M}{M_1}\frac{T_0}{T}\frac{\rho_0 c_0}{\pi r_0^3 \rho_p}, \quad (14)$$

where ρ_0 is the density of an aluminum particle.

When deriving this expression, the change of the gas mixture flow-rate as a result of combustion of aluminum particles was ignored. We should note that this assumption is common in calculations of combustion chambers [3]. With the help of Eqs. (12)–(14), we can obtain the expression for the steady-state combustion rate of aluminum particles in the volume unit

$$W^0 = -4\pi r^2 \rho_p N \frac{dr}{dt} = \frac{8}{3}\frac{M}{M_1}\frac{T_0}{T}\frac{\rho_0 c_0^2 \alpha}{(1 + \alpha c_0 t / r_0^{3/2})^3}. \quad (15)$$

As is seen from this expression, in contrast to the high-temperature combustion of the monodisperse system of carbon particles [8], in the case of the combustion of aluminum particles, the boundary of the burning zone is absent and the process is continued beyond the combustion chamber (in the nozzle and in the channel of a MHD generator).

The energy equation for the steady-state combustion of aluminum particles in the combustion chamber has the form

$$\rho c_p u \frac{dT}{dx} = \frac{Q}{4M} W^0.$$

The boundary condition is $T = T_0$ for $x = 0$.

The approximated solution to the last equation has the form

$$T = T_0 + \frac{Q c_0}{3 M_1 c_p}\left[1 - \frac{1}{(1 + \alpha c_0 x / \langle u \rangle r_0^{3/2})^2}\right];$$

here, $\langle u \rangle$ is the average velocity of the gas mixture in the combustion chamber: $\langle u \rangle = u_0 \langle T \rangle / T_0$, $\langle T \rangle$ is the gas-mixture temperature averaged over the combustion chamber length.

Averaging the last expression over the chamber length, we arrive at the expression:

$$\frac{\langle T \rangle}{T_0} = \frac{\langle \alpha_s^2 \rangle}{\alpha_{s0}^2} = \frac{\alpha c_0}{u_0}\frac{l}{r_0^{3/2}}, \quad (16)$$

where l is the length of the combustion chamber.

When deriving the expression for $\langle T \rangle$, it was taken into account that the following inequalities take place:

$$\frac{Q c_0}{3 M_1 c_p T_0} \gg 1; \quad \frac{\alpha c_0 l}{u_0 r_0^{3/2}} \gg 1.$$

Furthermore, averaging expression (15) for the steady-state combustion rate, we obtain with the help of (16)

$$\langle W^0 \rangle = \frac{M}{M_1}\frac{\rho_0 c_0 u_0}{l}.$$

In [7], the results of experiments on the combustion rate of finely dispersed aluminum particles as a function of temperature and pressure for the invariable composition of the gas mixture are given. According to these data, the combustion rate practically does not change within the temperature range from 1600 to 3300 K, and the pressure dependence ceases to manifest itself for $p > 25$ atm. In this case, we can obtain an approximate expression for W'

$$W' = \langle W_0 \rangle \frac{p'}{p} \approx \frac{M}{M_1}\frac{\rho_0 c_0 u_0}{l\gamma}\frac{p'}{p}.$$

It is taken into account in the last expression that for acoustic vibrations in gas mixtures the following relationships takes place the (quasi-adiabatic approach) [3]

$$\frac{\rho'}{\rho} = \frac{1}{\gamma}\frac{p'}{p}, \quad \frac{N'}{N} = \frac{\rho'}{\rho}.$$

Substituting the expression for W' into (10), we obtain an equation of the telegraph-type, which approximately describes the excitation of acoustic vibrations while combusting aluminum particles in the combustion chamber of a pulsed MHD generator:

$$\frac{\partial^2}{\partial x^2}\left(\frac{p'}{p}\right) = \frac{1}{\langle \alpha_s^2 \rangle}\frac{\partial^2}{\partial t^2}\left(\frac{p'}{p}\right) - 2\frac{\delta}{\langle \alpha_s^2 \rangle}\frac{\partial}{\partial t}\left(\frac{p'}{p}\right), \quad (17)$$

where $\delta = \dfrac{Q c_0}{8 M_1 c_p T_0}\dfrac{u_0}{l}$.

To determine frequencies of acoustic vibrations as a result of their excitation, it is necessary to set boundary conditions for Eq.(17). The question on the boundary conditions at the nozzle inlet is rather complicated and can be the object of a special study [3, 4]. In the present paper, similar to [4], the simplest assumption is made that the flow-velocity perturbations in the critical cross section of the nozzle are absent. Then, the boundary conditions can be written in the form

$$\frac{\partial p'}{\partial x} = 0 \text{ for } x = 0; \quad (17.1)$$

$$\frac{\partial p'}{\partial x} = 0 \text{ for } x = l. \quad (17.2)$$

Solving Eq. (17) by the method of separation of variables with allowance for the boundary conditions, we obtain

$$\frac{p'}{p} = e^{\delta t}\sum_{k=1}^{\infty} B_k \cos\frac{\pi k x}{l} \times \cos\left[\sqrt{\left(\frac{\pi k}{l}\right)^2 \langle a_s^2\rangle - \delta^2}\, t + \varphi_k\right]. \quad (18)$$

Here, $k = 1, 2, 3, \ldots$. The quantities B_k, φ_k, and the eigenfrequency are determined from the initial conditions and boundary conditions, respectively. This frequency is

$$\omega_k = \frac{\pi k \langle a_s\rangle}{l}.$$

It is seen from expression (18) that for $\delta > 0$ the excitation of acoustic vibrations caused by the combustion of aluminum particles can occur with the increment

$$\mu = \frac{2\pi\delta}{\sqrt{\left(\frac{\pi k}{l}\right)^2 \langle \alpha_s^2\rangle - \delta^2}}. \quad (19)$$

As follows from formula (18), excitation of the acoustic vibrations results in a decrease of the vibration frequency of the combustion chamber compared to the eigenfrequency. However, this decrease is insignificant. For example, for combustion of aluminum particles with $r_0 = 30$ μm, $T_0 = 400$ K in air, the value of δ is equal to ~70 s^{-1} for the principal harmonic ~3000 s^{-1} ($l \sim 1$ m). As is seen from expressions (18) and (19), the excitation conditions for acoustic vibrations are improved with an increase in the initial concentration of the oxidant and a decrease in the initial sizes of aluminum particles (or a reduction in the length of the combustion chamber). These conclusions are confirmed by the known fact of the excitation of acoustic vibrations by enhancement of the afterburn in the combustion chamber [3].

In conclusion, we note that the condition of the vibration excitation, which is known in thermal acoustics as the Rayleigh criterion [3], allows us to obtain sufficient conditions for acoustic stability and reveal sources of the vibration energy in the case when they are not evident, e.g., for phase transitions in vapor–gas mixtures [9]. However, this criterion does not allow us to determine the increment and the vibration frequency. The model of the acoustic-vibration excitation, which is suggested in this paper as distinct from the Rayleigh criterion, makes it possible to obtain (with invoking a known empirical dependence for the rate of steady-state combustion of an individual aluminum particle) the expression for the increment and frequency, which explicitly depends on the fuel and oxidant parameters.

REFERENCES

1. Yu. M. Volkov, Yu. G. Degtev, V. V. Krikun, *et al.*, in *Proc. of 8th Intern. Conf. on MHD Power Transformation, Moscow, Russia, 1983* (Moscow, 1983), p. 104.
2. Yu. G. Degtev and V. P. Panchenko, Teplofiz. Vys. Temp. **31**, 229 (1993).
3. K. I. Artamonov, *Thermohydroacustical Stability* (Mashinostroenie, Moscow, 1982).
4. *Liquid Propellant Rocket Combustion Instability*, Ed. by D. T. Harrje and F. G. Reardon (NASA, Washington, 1972; Mir, Moscow, 1975).
5. E. L. Borblik, R. V. Ganefel'd, V. V. Naletov, *et al.*, Preprint No. 67, IED AN UkrSSR (Inst. of Electrodynamics, Akad. Nauk UkrSSR, 1973).
6. F. A. Williams, *Combustion Theory* (Addison–Wesley, Reading Mass., 1968; Nauka, Moscow, 1971).
7. N. F. Pokhil, A. F. Belyaev, Yu. V. Frolov, *et al.*, *The Combustion of Powder-Like Metals in Active Media* (Nauka, Moscow, 1972).
8. A. M. Golovin and V. R. Pesochin, Fiz. Goreniya Vzryva **21**, 59 (1985).
9. V. R. Pesochin, Teplofiz. Vys. Temp. **32**, 791 (1994).

Translated by T. Galkina

Doklady Physics, Vol. 47, No. 3, 2002, pp. 219–223. Translated from Doklady Akademii Nauk, Vol. 383, No. 1, 2002, pp. 46–50.

MECHANICS

New Asymmetric and Multimode Solutions of the Problem on Viscous-Fluid Flow inside a Plane Confusor

L. D. Akulenko*, D. V. Georgievskiĭ, and S. A. Kumakshev***

Presented by Academician D.M. Klimov October 2, 2001

Received October 3, 2001

The problem on steady viscous-fluid flows in a plane confusor (the Jeffrey–Hamel problem [1–3]) again attracts attention due to increased numerical and analytical possibilities of currently available computers, as well as to the development of corresponding software [4, 5]. This attention is also induced by practical needs for solving a wider class of problems on flows of a viscoplastic medium with a low yield stress in a plane confusor [6, 7]. In this paper, we report the results of constructing and investigating multimode and asymmetric solutions in a wide region of physical and geometric parameters of the system. New qualitative mechanical effects were established and discussed.

1. We consider a steady flow of an incompressible fluid with density ρ in a plane confusor, which has angle 2β ($0 < \beta < \pi$) and outflow power Q ($Q > 0$) at the point O. It is convenient to describe the motion in the polar coordinates (r, θ), where the region occupied by the fluid has the form $|\theta| < \beta$, $r > 0$. In addition to the density, the fluid is characterized by the kinematic viscosity ν. For the plane confusor, three quantities $\{\rho, Q, \nu\}$ are dimensionally dependent ($[Q] = [\nu]$). Since there are no other dimensional quantities in the problem, the subsequent equations cannot be made totally dimensionless. The Reynolds number $\mathrm{Re} = \dfrac{Q}{\nu}$ is a dimensionless combination.

For a certain distribution of the pressure p in the angle θ (for $r \longrightarrow \infty$, this distribution can be found on the basis of kinematic relationships), the velocity field (v_r, v_θ) is radial [1, 3]:

$$v_r = -\frac{Q}{r}V(\theta), \quad v_\theta \equiv 0. \tag{1}$$

According to Eqs. (1) providing the incompressibility condition, we write the nonzero components of the strain-rate and stress tensors

$$v_{rr} = -v_{\theta\theta} = \frac{Q}{r^2}V(\theta), \quad v_{r\theta} = -\frac{Q}{2r^2}V'(\theta), \tag{2}$$

$$\sigma_{rr,\,\theta\theta} = -p \pm \frac{2\rho Q^2}{r^2\mathrm{Re}}V(\theta),$$
$$\sigma_{zz} = -p, \quad \sigma_{r\theta} = -\frac{\rho Q^2}{r^2\mathrm{Re}}V'(\theta). \tag{3}$$

The substitution of Eqs. (3) into two Navier–Stokes equations [1] leads to the following ordinary differential equation for the function $V(\theta)$ appearing in Eqs. (1)–(3) and yields the pressure p:

$$V'' + 4V - \mathrm{Re}V^2 = C, \quad C = \mathrm{const}; \tag{4}$$

$$p = \frac{\rho Q^2}{2r^2\mathrm{Re}}(C - 4V). \tag{5}$$

The mechanical meaning of the constant C is clear from the condition of adhering the fluid to the confusor walls $|\theta| = \beta$

$$V(\pm\beta) = 0, \quad C = V''(\pm\beta). \tag{6}$$

Furthermore, the integral condition of constant flow rate closes the formulation of the Jeffrey–Hamel problem:

$$\int_{-\beta}^{\beta} V(\theta)d\theta = 1. \tag{7}$$

The analytical investigations of the problem, Eqs. (4), (6), and (7), were extensively considered and reported in special papers [4, 5] and manuals [1–3]. The order of Eq. (4) can be reduced by multiplying both sides by V' and isolating the total derivatives. The equation has the first integral

$$\frac{1}{2}V'^2 + 2V^2 - \frac{1}{3}\mathrm{Re}V^3 - CV = \frac{1}{2}V'^2(\mp\beta). \tag{8}$$

* *Institute for Problems of Mechanics, Russian Academy of Sciences, pr. Vernadskogo 101, Moscow, 117526 Russia*

** *Moscow State University, Vorob'evy gory, Moscow, 119899 Russia*

1028-3358/02/4703-0219$22.00

It follows from Eq. (8) that the derivatives V' are equal in magnitude at the zeros θ_i of the function $V(\theta)$; i.e., we have $V'^2(\theta_i) = V'^2(\mp\beta)$. Equations (8) and (4) can be integrated in elliptic functions [1–3]. However, it is difficult to analyze the elliptic integrals obtained and to solve the set of two transcendental equations with respect to the constants of integration [1]. One fails to construct an explicit solution of the boundary value problem for arbitrary values of parameters β and Re.

It should be noted that Re can formally be negative; in this case, a diffuser flow takes place ($Q < 0$). Such a flow was considered as more complicated and diverse than the confusor one. Asymmetric (about the axis $\theta = 0$) regimes and regimes admitting the alternation of flow-out and flow-into zones (multimode regimes) were known for this flow [1–3]. The presence of these regimes is the manifestation of the fact that the nonlinear boundary value problem with the condition of constant flow rate has several solutions. With increasing Re, a steady flow in a diffuser loses its stability and becomes turbulent.

However, the asymmetric and multimode character was not explicitly established for a confusor flow. Therefore, the following questions remained unanswered: (a) Are the asymmetric or multimode velocity profiles possible in the confusor along with the symmetric and single-mode ones, and if so, under what conditions? (b) If these profiles are possible, what are their properties?

The boundary value problem, Eqs. (4) and (6), with condition (7) is two-parametric; it admits variational treatment [4, 5]. For further numerical–analytical investigation, it is convenient to change the parameters (β, Re) to the pair (a, b), where $a = 4\beta$ and $b = 2\beta\mathrm{Re}$. Changing $V(\theta)$ to the new unknown function $y(x)$, where $V = \dfrac{y}{2\beta}$ and the argument $\theta = (2x - 1)\beta$ $(0 < x < 1)$, the initial problem is represented in the form

$$y'' + a^2 y - by^2 = \lambda, \quad y(0) = y(1) = 0,$$
$$y'(0) = \gamma, \quad \int_0^1 y(x)dx = 1, \tag{9}$$
$$\lambda = 8\beta^3 C = y''(0) = y''(1).$$

Along with the variables y and y', we introduce the variable z characterizing the fluid flow rate according to Eq. (8):

$$z' = y - 1, \quad z(0) = 0, \quad z(1) = 0. \tag{10}$$

It is necessary to solve the boundary value problem, Eqs. (9) and (10), for the variables y and z. The parameter λ is unknown and must be calculated. This parameter can be excluded by differentiating Eq. (9); however, a third-order nonlinear equation is obtained as a result.

2. On the basis of the high-accuracy numerical–analytical method with improved convergence [4] in a wide range of parameters (a, b), we constructed numerical solutions to problem (9) in the class of symmetric single-mode profiles $y(x)$ [5]. We also analytically investigated the following asymptotic cases of the parameters (a, b) or (β, Re):

(i) $\mathrm{Re} \ll 1$, $0 < \beta < \dfrac{\pi}{2}$;

(ii) $\mathrm{Re} \sim 1$, $0 < \beta \ll 1$;

(iii) $\beta \ll 1$, $\beta\mathrm{Re} \sim 1$;

(iv) $\mathrm{Re} \gg 1$, $\beta \sim 1$.

In case (iii), numerical methods should be applied [5]; in case (iv), there exists a formal passage to the discontinuous-profile limit for an inviscid fluid. The presence of the large parameter b requires the application of methods of singular perturbations [8]. By means of these methods, the asymptotic behavior of the solution [1] in case (iv) can be represented in the very convenient form [5, 7]

$$y_\infty(x) \approx 1 - \frac{6}{1 + \cosh\left[\operatorname{arccosh} 5 + \sqrt{\frac{b}{2}}(1 - |2x - 1|)\right]},$$
$$y_\infty(0) = y_\infty(1) = 0, \tag{11}$$
$$y'_\infty(0) = \gamma_\infty \approx \sqrt{\frac{4b}{3}}, \quad y''_\infty(0) = \lambda_\infty \approx -b, \quad b \longrightarrow \infty.$$

Expressions (11) provide satisfactory accuracy for $b \sim 10^3$–10^4.

Further, we present certain integral estimates for $y(x)$, λ, and γ following from Eq. (9). It should be noted that, for an arbitrary function $f(x)$ continuously differentiable on the interval $0 < x < 1$, the following equality is valid:

$$\int (y'' + a^2 y - by^2) f' dx = \lambda[f(x_2) - f(x_1)], \tag{12}$$

where two arbitrary zeros x_1 and x_2 of the function $y(x)$ satisfy the conditions $0 \le x_1 < x_2 \le 1$. In Eq. (12) and below, we omit the limits of integration with respect to x from x_1 to x_2.

A. Let $f(x) = y(x)$; in this case, integration of Eq. (12) by parts yields two important equalities

$$y'(x_2) = \pm y'(x_1). \tag{13}$$

If $x_1 = 0$ and $x_2 = 1$, the lower sign in Eq. (13) corresponds to the symmetrical single-mode regime including the classical one; the upper sign corresponds to the asymmetric regime. It follows from the condition $y'(1) = y'(0)$ that the multimode velocity profile is possible.

B. Let $f' = y$ and $f(0) = 0$. In this case, taking into account the Friedrichs inequality

$$\int y'^2 dx \geq \left[\frac{\pi^2}{(x_2 - x_1)^2}\right]\int y^2 dx,$$

we obtain the upper estimate of the parameter λ from Eq. (12):

$$\begin{aligned}\lambda\int y dx &= \int(-y'^2 + a^2y^2 - by^3)dx \\ &\leq \left(a^2 - \frac{\pi^2}{(x_2 - x_1)^2}\right)\int y^2 dx - b\int y^3 dx,\end{aligned} \tag{14}$$

which is very accurate for the case of the single-mode flow (on the entire interval $0 \leq x \leq 1$).

C. Let $f(x) = y'(x)$; in this case, integrating (12) by parts, we write the equality

$$n\lambda\gamma = \int(y''^2 - a^2y'^2 + 2byy'^2)dx, \tag{15}$$

where n takes the values –2, 0, and 2 depending on the choice of the sign in Eq. (13). For $n = 0$, i.e., for the functions with the boundary conditions

$$y(x_1) = y(x_2) = 0,$$
$$y'(x_1) = y'(x_2), \quad y''(x_1) = y''(x_2),$$

one more Friedrichs inequality is valid:

$$\int y''^2 dx \geq \frac{4\pi^2}{(x_2 - x_1)^2}\int y'^2 dx.$$

This inequality and Eq. (15) lead to the estimate

$$\int\left[\frac{4\pi^2}{(x_2 - x_1)^2} - a^2 + 2by\right]y'^2 dx \leq 0. \tag{16}$$

3. For definiteness, we consider a fixed value of the aperture angle $\beta = 10°$, i.e., $a \approx 0.7$, that is widely met in the applied problems [5, 7]. Numerous calculations were also carried out for other values of a. The value b is considered to vary within wide limits: $0 < b \leq 200$, i.e., $0 < \mathrm{Re} \lesssim 600$. A high-accuracy solution of Eqs. (8) and (10) with a relative error of 10^{-7}–10^{-8} {absolute error $O(10^{-5})$} can be constructed using the modified method of improved convergence of the Newton algorithm type and the procedure of continuation with respect to a parameter [4]. It was successfully applied to the classical problem of investigating single-mode symmetric flows [5] for which an exact limiting solution is known in the analytical form for $b \longrightarrow 0$ and arbitrary a.

Substantial difficulties in constructing multimode velocity profiles are caused by the degeneration of the problem for $b \longrightarrow 0$. This fact leads to unlimited values of the desired parameters $\gamma(b)$ and $\lambda(b)$ necessary for integrating the corresponding Cauchy problem. For a certain fixed value of the parameter $b = b_0$ (conventionally, $b_0 \approx 10$) and the number of the chosen mode (n = 2, 3, 4, …), we seek unknown values γ and λ and calculate them with a high accuracy, providing the above residual with respect to the boundary conditions. Then, by means of the procedure of continuation with respect to the parameter b, we plot universal curves $\gamma(b)$ and $\lambda(b)$ for $0 < b < b_0$ and $b_0 < b < \infty$. The difficulties in these calculations are aggravated by the fact that the values $\gamma_n \gg \gamma_1$ and $\lambda_n \gg \lambda_1$ (by several orders of magnitude) and attain high values for $b = 1$, for example, $\gamma_5 \sim 10^4$ and $\lambda_5 \sim 10^5$. These circumstances can explain why conclusive results on determining and analyzing multimode flows in the Jeffrey–Hamel problem have not been obtained yet.

Below, we outline and discuss the graphic representation of the results of numerical–analytical investigation of multimode flows for n = 2, 3, 4, 5. They are compared with the corresponding curves for the classical solution ($n = 1$), which was studied in detail in [5], in particular, for various values of the parameter a. It was established that the odd n modes for $n \geq 2$ correspond to symmetric (about $x = 1/2$, i.e., $\theta = 0$) solutions, whereas the even n modes correspond to asymmetric solutions.

The analysis shows that the flows have certain structural properties. Namely, the positive maxima ($n \geq 3$) and the negative minima ($n \geq 4$) of the functions $y_n(x, b)$ have the same magnitudes. Furthermore, in all the zeros x_i, $i = 1, \ldots, n + 1$, of the function $y_n(x, b)$ (for fixed n, b), the derivatives y_n' are equal in magnitude; i.e., $\gamma_n(b) = \pm y_n'(x_i, b)$. Thus, in a certain sense, a multimode flow is a combination (aggregate) of single-mode and two-mode flows. This property likely follows from the fact that the flows are radial.

Figures 1 and 2 show the functions $\gamma_n(b)$ and $\lambda_n(b)$ in different scales for $1 \leq b \leq 10$ and $10 \leq b \leq 200$. The functions determine the solutions to the boundary value problem, Eqs. (9) and (10), by integrating the Cauchy problems for a fixed value of the parameter a (i.e., the angle β). The curves are grouped in pairs n = 2 and 3, and n = 4 and 5. Interesting properties of these curves manifest themselves near $b = 0$, and the graphs have vertical asymptotes: $\gamma_n \longrightarrow +\infty$ and $\lambda_n \longrightarrow -\infty$ for $b \longrightarrow +0$. We recall that finite values γ_1 and λ_1 correspond to the classical single-mode solution [5]. Large magnitudes of γ_n and λ_n for $b \sim 1$ are also remarkable. The differences $\gamma_n - \gamma_{n-1}$ and $\lambda_{n-1} - \lambda_n$ increase indefinitely for $b \to +0$ and with the number n. Every curve γ_n attains a minimum for a certain large value $b = b_n^\gamma \sim 10^2$–10^3 and tends very slowly to asymptote $\gamma_\infty = \sqrt{4b/3}$ (11) from above. Similarly, the curves λ_n attain maxima for certain $b = b_n^\lambda \sim 10^2$ and also tend very slowly to asymptote $\lambda_\infty = -b$ (11) from below. On the

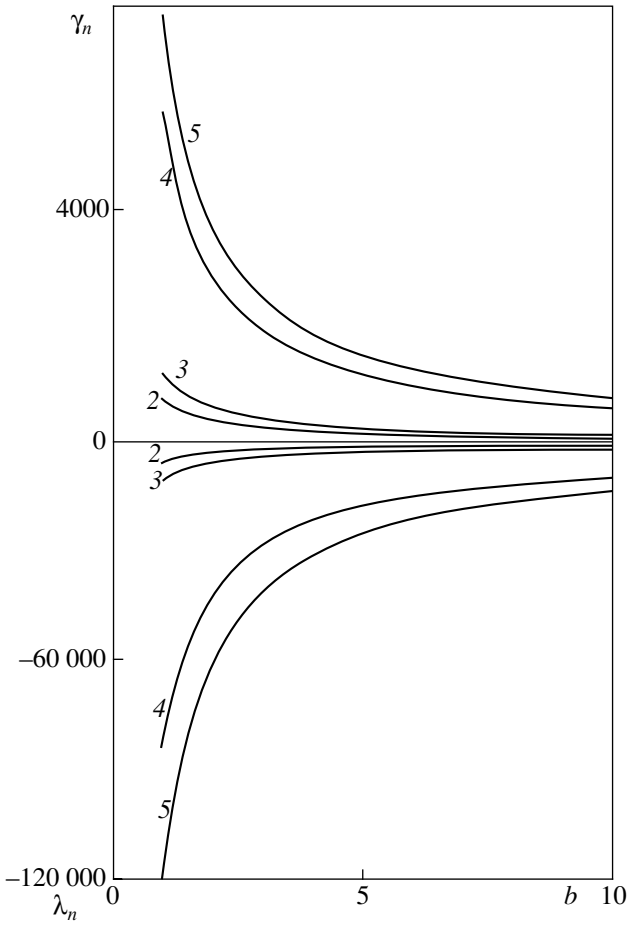

Fig. 1. γ_n and λ_n vs. the parameter b, $1 \le b \le 10$.

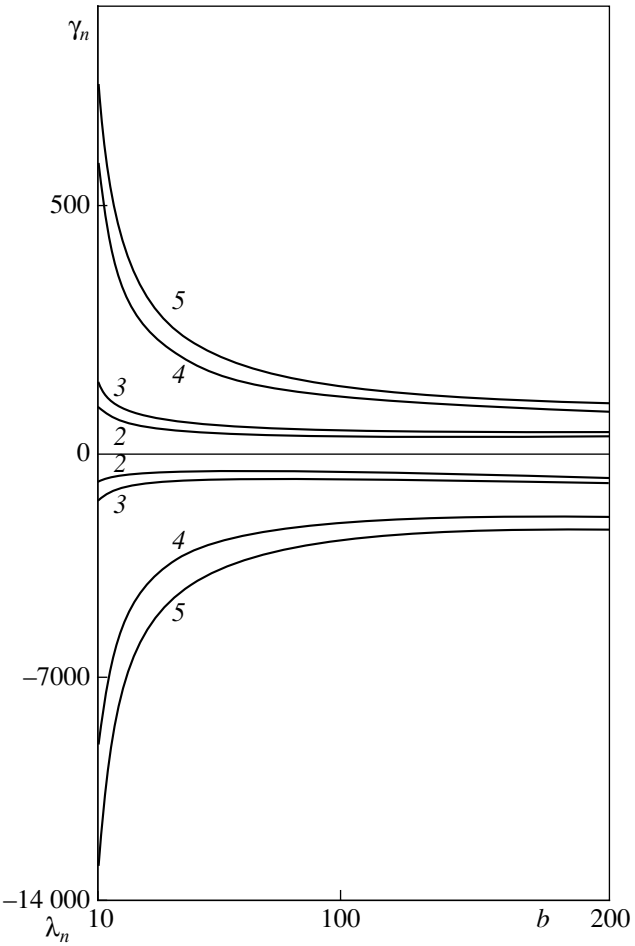

Fig. 2. The same as in Fig. 1, but for $10 \le b \le 200$.

basis of these facts, we arrive at the important mechanical conclusion that all the modes of steady flows, including the fundamental one ($n = 1$, see [5]), tend to a perfect-fluid flow in the limit $b \longrightarrow \infty$ (Re $\longrightarrow \infty$) in a certain metric for $0 < x < 1$.

The curves $\gamma_n(b)$ and $\lambda_n(b)$ are essentially the principal result of these investigations and provide the numerous characteristics of steady flows in a confusor by integrating the Cauchy problem for Eqs. (9) and (10). These characteristics, cited in Section 1, are velocity profile (1), pressure (5), components of the strain-rate tensor (2) and strain tensor (3), etc. The shape of the curves γ_n and λ_n is rather simple; however, their construction requires very cumbersome high-

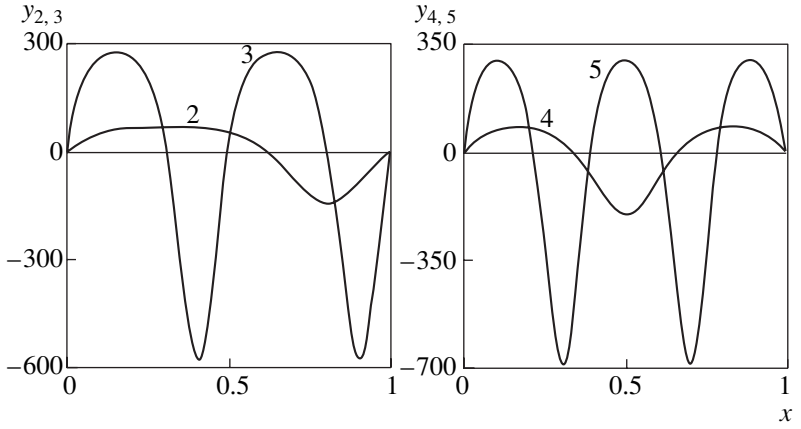

Fig. 3. Velocity profiles $y_n(x)$ for $b = 1$.

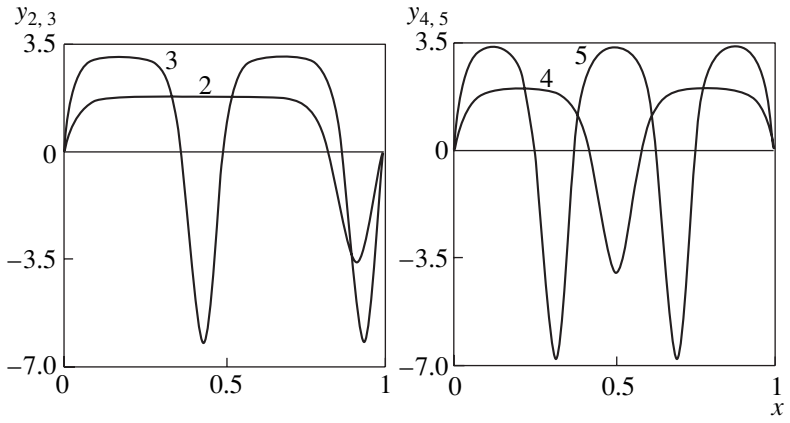

Fig. 4. The same as in Fig. 3, but for $b = 200$.

accuracy calculations, which are considerably complicated for $b \longrightarrow +0$ and $b \longrightarrow \infty$. Pronounced boundary layer effects take place in the problem. Calculating algorithms on the basis of the known functional-analysis methods (Bubnov–Galerkin), finite-element and finite-difference methods does not provide satisfactory results.

To illustrate multimode flows, Figs. 3 and 4 show the velocity profiles $y_n(x)$, $n = 2, 3, 4, 5$, for a relatively small value of $b = 1$ and a relatively large value of $b = 200$, respectively. For small values of the parameter b (Re), large oscillations of positive and negative velocity values, i.e., the functions $y_n(x)$, are observed. The inflow ($y_n > 0$) and outflow ($y_n < 0$) regions correspond to these values. An increase in the parameter b(Re) reduces the amplitude of oscillations and reverse flows. For large values $b \sim 10^2$–10^3, the pronounced forms corresponding to confusor flow (11) are observed for a weakly viscous fluid. A deviation from the rectangular profile of a flow of a nonviscous (perfect) fluid in a certain metric tends to zero for $0 < x < 1$; near $x = 0$ and 1 ($\theta = \mp\beta$), typical boundary layer phenomena arise.

ACKNOWLEDGMENTS

This work was supported by the Russian Foundation for Basic Research, project nos. 99-01-00222, 99-01-00276, 01-01-06306, and 99-01-00125.

REFERENCES

1. N. E. Kochin, I. A. Kibel', and N. V. Roze, *Theoretical Hydromechanics* (Fizmatlit, Moscow, 1963).
2. L. D. Landau and E. M. Lifshitz, *Course of Theoretical Physics: Fluid Mechanics* (Nauka, Moscow, 1986; Pergamon, New York, 1987).
3. L. G. Loĭtsyanskiĭ, *Mechanics of Fluids and Gases* (Nauka, Moscow, 1987).
4. L. D. Akulenko and S. V. Nesterov, Dokl. Akad. Nauk **374**, 624 (2000) [Dokl. Phys. **45**, 543 (2000)].
5. L. D. Akulenko, D. V. Georgievskiĭ, S. A. Kumakshev, and S. V. Nesterov, Dokl. Akad. Nauk **374**, 44 (2000) [Dokl. Phys. **45**, 467 (2000)].
6. D. M. Klimov, S. V. Nesterov, L. D. Akulenko, D. V. Georgievskiĭ, and S. A. Kumakshev, Dokl. Akad. Nauk **375**, 37 (2000) [Dokl. Phys. **45**, 601 (2000)].
7. D. V. Georgievskiĭ, *Stability of Deformation Processes of Viscoplastic Bodies* (Izd. URSS, Moscow, 1998).
8. S. A. Lomov, *Introduction to the General Theory of Singular Perturbations* (Nauka, Moscow, 1981).

Translated by V. Bukhanov

Doklady Physics, Vol. 47, No. 3, 2002, pp. 224–228. Translated from Doklady Akademii Nauk, Vol. 383, No. 1, 2002, pp. 51–56.

MECHANICS

On an Extreme Feature of Detached Flows upon the Interaction of a Shock with a Boundary Layer

M. A. Zubin and N. A. Ostapenko

Presented by Academician G.G. Chernyĭ September 20, 2001

Received September 27, 2001

Calculations carried out with empirical relations under certain assumptions have revealed nontrivial regularities inherent in λ-configurations of shocks produced at the developed separation of a turbulent boundary layer in cone flows and are characterized by the minimum (or near-minimum) production of entropy.

Experimental studies [1–4] of the separation of a turbulent boundary layer in cone flows under the action of shocks revealed that a disturbed flow has a number of fundamental features that have not been theoretically explained yet. Among them are the following ones. A flow with a boundary layer separation has a cone character, which is disturbed only in the regions of laminar-to-turbulent state transition [2–4]. The quantitative characteristics of a detached flow for the artificially induced turbulence of a boundary layer [1] coincide with those under natural conditions of varying the local Reynolds number along the line of turbulent boundary layer separation in the range $\mathrm{Re} \times 10^{-6} \in (1.5; 20)$ [4]. Some other features will be mentioned later.

Semiempirical relations for angles φ and γ between the direction of an undisturbed flow with the Mach number M and the lines of separation and attachment, respectively (see Fig. 1, the flow diagram), are obtained in [4] for regimes of "free" interaction $\left(\varphi < \frac{\pi}{2} - \varepsilon\right)$ [5, 6]. These relations are applicable for calculating the angular dimensions and position of the region of separating the turbulent boundary layer under the model-problem conditions (a flow in a right dihedral angle, Fig. 1). They may also be used for similar calculations in a shock layer at the interaction of a boundary layer with curvilinear shocks and compression-shock systems [4, 7, 8]. The formula for calculating the angle φ has the form [4]

$$\varphi = h\log\left(\frac{p_s}{p_k}\right) + \varphi_k,$$
$$h = 5.1\exp(-0.89\mathrm{M}) + 0.71, \qquad (1)$$
$$\varphi_k = \arcsin\left(\frac{\mathrm{M}_{nk}}{\mathrm{M}}\right).$$

Here, the quantities with the index *k* correspond to the formation of separating the turbulent boundary layer, and $p_k = 1.6$ is the minimum value of the intensity p_s of the shock *C* generated by a plate *A*, which makes an angle α with the flow direction at infinity (Fig. 1). The shock is incident at a right angle on the plate *B* positioned along the flow direction. The Mach number

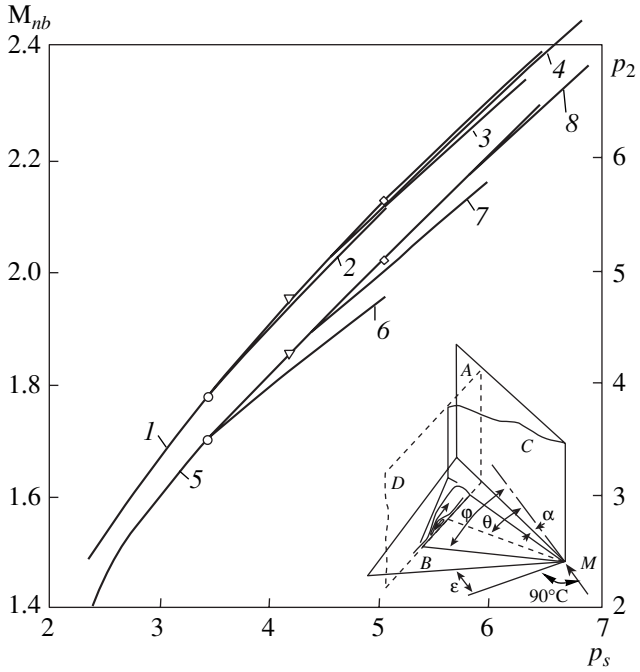

Fig. 1.

Institute of Mechanics, Moscow State University, Michurinskiĭ pr. 1, Moscow, 117192 Russia

1028-3358/02/4703-0224$22.00

$M_{nk} = 1.23$ of the undisturbed-flow velocity component normal to the wave corresponds to p_k.

The values of p_k and M_{nk} agree with data on the formation of a plane separation (see, e.g., [9]). This is one of the general features of separating the turbulent boundary layer in flows with various dimensions. Among these features is the fact that the pressure downstream from the oblique shock above the region of the developed separation is equal to the pressure plateau p_1. The latter corresponds to the free-interaction regimes [2, 3]. According to [10], p_1 (divided by the pressure p_∞ in the undisturbed flow) can be calculated by the formula

$$p_1 = 0.287 + 0.713M, \tag{2}$$

which yields adequate results for $M \in (1.75, 5)$. For cone flows with boundary-layer separation, in Eq. (2) M should be replaced by the Mach number $M_{ns} = M\sin\varphi(p_s)$ [2–4] of the free-flow velocity normal to the separation line.

For "restricted" interaction, the indicated property holds as before, but with other pressure levels [5, 6]. For $M = 3.04$ and $\varepsilon \in (36°, 46°)$, the slope θ_s of the oblique shock above the separation region is calculated as

$$\theta_s = K(\varepsilon)[\rho_s - p_s(\varepsilon)] + \theta_s^0[p_s(\varepsilon)],$$
$$p_{sm} \geq p_s \geq p_s(\varepsilon), \tag{3}$$
$$K(\varepsilon) = -1.03\varepsilon^2 + 1.774\varepsilon - 0.577,$$

$$\varphi[p_s(\varepsilon)] = \frac{\pi}{2} - \varepsilon. \tag{4}$$

Here, the intensity $p_s(\varepsilon)$ of the incident shock C (Fig. 1) is such that, according to Eq. (4), the separation line coincides with the leading edge of the plate B having the glancing angle ε; the slope $\theta_s^0[p_s(\varepsilon)]$ of the shock above the separation region corresponds to this case and is calculated using both Eq. (2) (with M replaced by $M\cos\varepsilon$) and the above pressure-plateau property; and the intensity p_{sm} of the incident shock C corresponds to the maximum possible value of the angle $\theta = \frac{\pi}{2} - \varepsilon$ (Fig. 1) at restricted interaction for fixed sweep angle ε.

Under certain assumptions, the above data enable us to calculate the entropy variation induced by passing the shock λ-configuration of a developed detached flow. It is impossible to calculate the entropy-flow increment by introducing a reference volume including the characteristic region of the disturbed flow produced by the interaction of the incident shock with the boundary layer (Fig. 1). The first reason is the lack of necessary qualitative data on the flow parameters in a conic separation zone and in adjacent flow regions. Moreover, it is difficult to simulate three-dimensional mixing processes in such a way as to provide an efficient calculation of the entropy increment caused by viscosity and heat conductivity.

Nevertheless, the effect of various processes on entropy production can be estimated. Let us consider the entropy increment $\Delta S_w = S_w - S_\infty$ per unit mass of a gas (S_∞ is the specific entropy in an undisturbed flow) when one or several shock waves of local supersonic regions located in the separation-zone outline travel through the shock λ-configuration and move further downstream [2–6]. We suppose that this entropy increment is about the increment in a single incident wave characterized by the Mach number M_n of the velocity normal to the wave front:

$$\Delta S_w \sim c_v \ln\left\{\left[1 + \frac{2\gamma}{\gamma+1}(M_n^2 - 1)\right]\right.$$
$$\left.\times\left[1 - \frac{2\gamma}{\gamma+1}\frac{(M_n^2 - 1)}{M_n^2}\right]^\gamma\right\}. \tag{5}$$

Here, c_v is the constant-volume specific heat for ideal gas, and γ is the specific heat ratio.

Let the entropy per unit mass of the gas increase due to viscosity (in the presence of velocity gradients) by ΔS_μ in a characteristic time of $T = L/U_\infty$, where L is the characteristic dimension of the reference volume in the flow direction or the length of the experimental model [2–4] and U_∞ is the velocity magnitude for the undisturbed flow. The similar increment determined by heat conductivity (in the presence of the temperature gradient) is denoted by ΔS_λ. These increments are about

$$\Delta S_\mu \sim c_v\frac{\gamma(\gamma-1)M^2}{\mathrm{Re}}, \quad \Delta S_\lambda \sim c_v\frac{\gamma}{\mathrm{Pr}\,\mathrm{Re}}. \tag{6}$$

Here, Re is the Reynolds number calculated on the length L, and Pr is the Prandtl number. We take into account the foregoing intervals of varying the quantities appearing in Eqs. (6), as well as the fact that $M_n > M_{nk}$ for a developed detached flow. Then, we conclude that the entropy increment in compression shocks of the shock λ-configuration, i.e., ΔS_w from (5), makes the greatest contribution to entropy production.

To find the entropy production in compression shocks situated under the contact-discontinuity surface emanating from the shock branch line, one should calculate the entropy flow transported in a unit of time by the gas particles passing through the oblique shock above the separation region and other downstream waves.

We assume that the isentropic-deceleration parameters (and, consequently, entropy) on all current surfaces between the indicated contact-discontinuity surface and conic separation region (Fig. 1), after the passage of all discontinuities, are close to (or coincide with) the corresponding parameters for gas particles passing

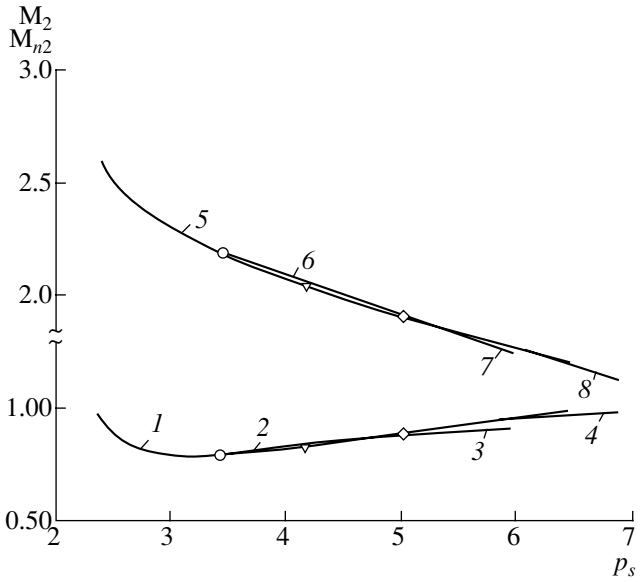

Fig. 2.

through the oblique shock and breakdown shock wave in the branch-line vicinity. There is only indirect support for this speculation. Such an assumption was made in [2] for particles on the current surface coming to the attachment line (Fig. 1), and this allowed description of those observed qualitative changes in the internal flow of the separation region that are caused, among other factors, by the transonic transition of the backward flow.

Since the entropy flow downstream of the shock λ-configuration is generally described by an improper integral, one should consider the ratio of this flow to the entropy flow transported in unit time by the corresponding particles of the undisturbed flow. Under the above assumption, this ratio reduces to the ratio of the values S_b and S_∞ of the specific entropy in the shock branch line under the contact-discontinuity surface and in the undisturbed flow, respectively. The reason is that, under the accepted assumption, the integrals are the mass flows upstream and downstream of the shock λ-configuration and are equal and cancel each other according to the mass conservation law. In turn, the calculation of the ratio S_b/S_∞ is equivalent to the calculation of the entropy function $s = \left(\frac{p_b}{p_\infty}\right)\Big/\left(\frac{\rho_b}{\rho_\infty}\right)^\gamma$, which will be discussed later.

To calculate gas parameters under the contact-discontinuity surface emerging from the shock branch line, one needs to determine the Mach number M_{nb} of the undisturbed-flow velocity component normal to the branch line. Relations (1), (2) (free interaction) or (3), (4) (restricted interaction) are inadequate to calculate M_{nb} for the given M and α. The quantity M_{nb} should be determined from a solution of the corresponding boundary value problem, since the oblique shock above the separation region interacts with the incident shock on the section of the subsonic cone flow downstream of the shock. The branch-line position is considered to be little different from the position of the line of the oblique-shock intersection with the undisturbed shock *C* incident on the plate *B* at a right angle (Fig. 1). This assumption is strongly supported by experimental results obtained for a disturbed flow by a special optic method [2–6]. Thus, we accept that M_{nb} is equal to the Mach number of the velocity normal to the line of intersection of the incident shock and the oblique shock specified by empirical relations (1), (2) or (3), (4).

The dependencies M_{nb} calculated in such a way are shown in Fig. 1 for the undisturbed-flow Mach number M = 3.04 corresponding to approximations (3). Curve *1* and $\alpha \in [12°, 30°]$ correspond to the free-interaction case, whereas curves *2–4* for ε = 46°, 41°, and 36°, respectively, correspond to the restricted interaction. The upper circle, triangle, and diamond denote the origins of respective curves *2–4*, which show the solutions of Eq. (4). The terminal points of these curves correspond to the values of the intensity of the incident shock *C*, when its position coincides with the leading edge of the plate *B*: $\theta = \frac{\pi}{2} - \varepsilon$ (Fig. 1, the flow diagram). Curves *2–4* differ little from curve *1* for the same p_s value, because the angle between the line of intersection of the oblique shock with the incident shock and the plate *B* is small compared with the angle θ.

The branch-point structure is calculated for a three-shock configuration, which is supplemented with a centered rarefaction wave when the corresponding solution is absent. In this case, the parameters of the breakdown shock wave at the branch point correspond to the acoustic point in the interior polar constructed for the Mach number of the uniform-flow velocity component downstream of the oblique shock above the flow separation region normal to the branch line.

Figure 1 also shows the data calculated for the pressure p_2 (divided by the pressure p_∞) downstream from the shocks at the branch point for (line *5*) free and (lines *6–8* corresponding to lines *2–4* for M_{nb}) restricted interactions. Figure 2 shows the Mach numbers on the sphere M_{n2} and the total velocity M_2 for parameters under the contact discontinuity at the branch point (curves *1*, *5* and *2–4*, *6–8* correspond to free and restricted interactions, respectively). The circles, triangles, and diamonds have the same meaning as in Fig. 1.

The results obtained for p_2 (Fig. 1) and M_2 (Fig. 2) with empirical relations (1)–(3) point to an unexpected fact: the total pressure recovery factor η in the flow downstream from the shock λ-configuration takes close values for two fundamentally different interaction regimes if the incident shocks have the same intensity. The same conclusion also holds for the entropy function related to the recovery factor as $s = \eta^{1-\gamma}$.

Let us consider the dependence $s(\gamma, M, p_{ss})$, where p_{ss} is the arbitrary intensity of the oblique shock ramifying in the three-shock configuration in a flow with the Mach number M. For $\gamma = 1.4$ (air), Figs. 3a and 3b show the curve nets $s(\gamma, M, p_{ss})$ corresponding to the Mach numbers M = (*1*) 1.5, (*2*) 1.7, (*3*) 1.9, (*4*) 2.1, (*5*) 2.3, and (*6*) 2.4 and M = (*1*) 1.5, (*2*) 2, (*3*) 2.5, (*4*) 3, (*5*) 3.5, and (*6*) 4, respectively. From the right, the curves are bounded by the values $p_{ss} = \dfrac{p_1 + p_s^s}{2}$, where p_1 is determined by Eq. (2) and p_s^s is the pressure at the sound point of the interior polar constructed for the number M. For each M value, the point *A* indicates the *s* value corresponding to the normal shock wave. These values do not coincide with the ordinates of the curves $s(\gamma, M, p_{ss})$ for $p_{ss} \longrightarrow 1$, because shock disturbance for a subsonic flow downstream from it depends irregularly on the intensity of the interacting oblique shock [11].

As is seen in Fig. 3, for each number M, there is an oblique shock with an intensity of p_{ss} such that, as it ramifies, the entropy increment for gas particles which have passed the shock λ-configuration under the contact discontinuity is minimal. Curves *7* in Figs. 3a and 3b correspond to the values of the entropy function for $p_{ss} = p_1$ given by Eq. (2) [10]. Thus, curves *7* give insight into entropy production in the shock λ-configuration, which is realized in a two-dimensional problem when a direct shock wave interacts with a turbulent boundary layer.

The other curves in Fig. 3 correspond to the results of calculations for the case of separation in a cone flow (Fig. 1). Here, the net of the curves M = const should be considered as M_{nb} = const, and the value of the abscissa p_{ss} should be considered as the intensity of the oblique shock interacting with the normally incident shock *C*. In Fig. 3a, curve *8* corresponds to $s(\gamma, M_{nb}, p_1)$ for free interaction. Here, p_1 is determined by Eqs. (1) and (2), where M should be replaced by $M_{ns} = M\sin\varphi\,(p_s)$. The Mach number for the undisturbed flow is M = 3.04, $\alpha^\circ \in [12.5^\circ, 30^\circ]$, $M_{ns} \in [1.74; 2.64]$, $M_{nb} \in [1.51, 2.39]$. In Fig. 3a, curves *9*–*11* correspond to the case of restricted interaction, when the slope of the oblique shock is determined by Eq. (3) with $\varepsilon = 46^\circ$, 41°, and 36°, respectively. The use of Eqs. (1) and (2) allows calculations of $s(\gamma, M_{nb}, p_1)$ for various M values. In Fig. 3b, the entropy function is shown for M = (*8*) 3.04, (*9*) 4, (*10*) 5, and (*11*) 6.

The results presented in Fig. 3 support the hypothesis that the principle of minimum entropy production [12] with restriction is realized in the flow formed by the interaction of shocks with a boundary layer. In this case, the states of particles at the entry and exit of the reference volume outside the layers where viscosity and heat conductivity are substantial should be accepted as the stationary states.

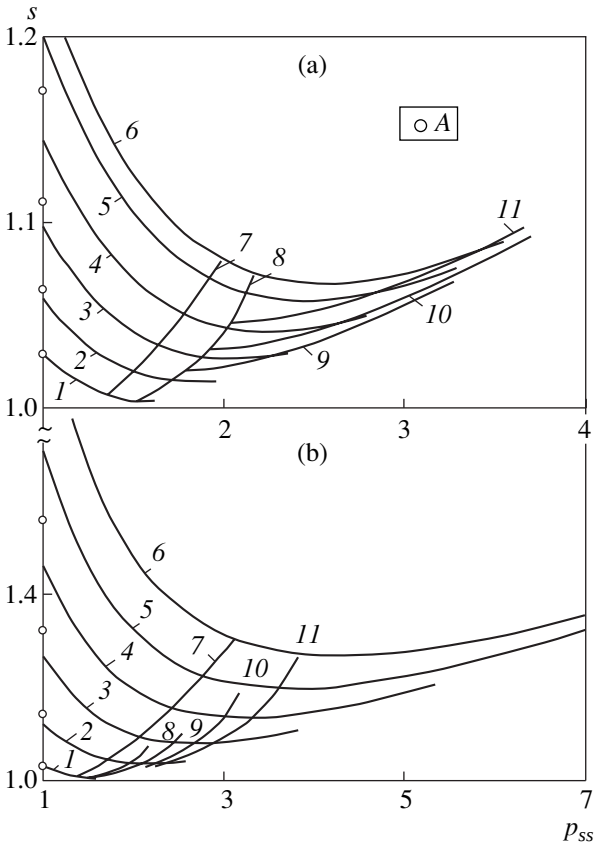

Fig. 3.

Indeed, curves *7* in Fig. 3 indicate that entropy production in the shock λ-configuration is not minimal. In order for it to reach a minimum, a considerable increase of oblique-shock intensity above the separation region is required. This increase is incompatible with available experimental data and the physical meaning of the theoretical results [13]. In other words, the existing spread of experimental data [9] for the pressure plateau in the separation region of a turbulent boundary layer excludes the values $p_{ss} = p_1$ that exceed certain critical values $p_{cr}(M)$ and are close to the minimum points of curves *1*–*6*. This is the essence of the foregoing restriction. At the same time, in the case of a turbulent boundary layer, $p_{cr}(M)$ is large enough to allow the shock λ-configuration to considerably reduce entropy production in contrast to the case of the separation of a laminar boundary layer.

For the free interaction of shocks with a turbulent boundary layer in cone flows, the two-dimensional separation has the foregoing fundamental properties in the plane normal to the separation line. However, an additional degree of freedom, the angle $\varphi(p_s)$ calculated from semiempirical formula (1), arises in the disturbed flow. It is precisely this degree of freedom combined with dependence (2) that makes it possible to choose the value M_{nb} in such a way that the corresponding p_1

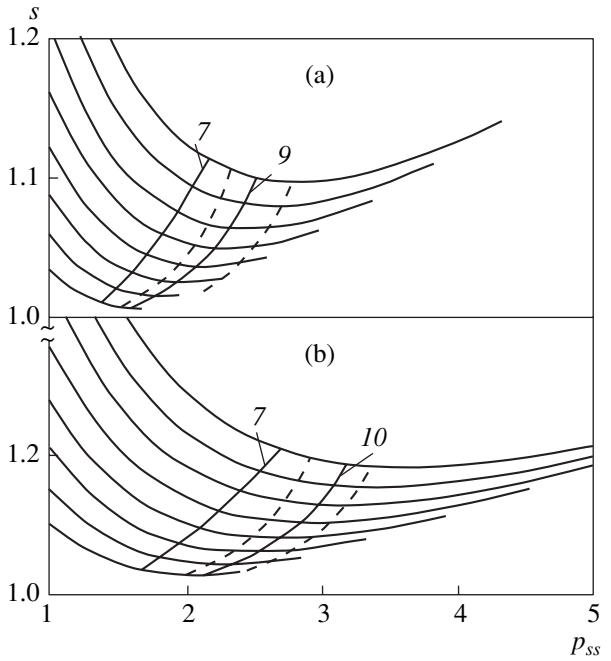

Fig. 4.

value provides the minimum value of $s(\gamma, M_{nb}, p_1)$ (Fig. 3b, curves *8–11*). For restricted interaction, the angle of the oblique shock above the separation region rises linearly with the intensity of incident shock (3), and M_{nb} is virtually unaffected (Fig. 1, curves *1–4*). In this case, the disturbed flow loses one degree of freedom and its equilibrium state becomes further from the state with minimum entropy production (Fig. 3a, curves *9–11*). However, the corresponding increase in the entropy function is small, as was indicated above, when the results for p_2 (Fig. 1) and M_2 (Fig. 2) were discussed.

Under the assumption that the principle of minimum entropy production with restriction is realized for the flows under consideration, it is easy to show that the cone character of a flow for free interaction is the key manifestation of this principle. Indeed, if the disturbed flow were not a cone flow but became a quasi-two-dimensional flow beginning with a certain local Re number, the values of the entropy function in the corresponding region of the shock-wave configuration would lie not in curves *8–11* but in curve *7* (Fig. 3b); i.e., entropy production would increase. The cone character of the flow can only be violated in regions of the laminar–turbulent transition, where $p_{cr}(M)$ changes. This behavior was observed experimentally.

In summary, we conclude that entropy production realized in the shock λ-configuration with the restriction on p_1 is analogous to the attainment of a boundary extremum in optimization problems.

Since Eq. (2) [10] is generally one of the available approximations for the pressure plateau [9], it is instructive to consider the effect of the p_1 value on the results calculated for the entropy-function. Figures 4a and 4b show results for M = 4 and 5, respectively. Curves *7* correspond to the separation in the two-dimensional problem. Curves *9* and *10* correspond to the respective lines in Fig. 3b. The dashed lines bound the regions involving all the pressure plateau values found in various experiments [9]. It is seen that the results of the calculations with the possible spread of $s(\gamma, M_{nb}, p_1)$ values do not change the above conclusions.

In conclusion, we note that the functional corresponding to entropy production can have no minimum because of conditions excluding process-parameter values falling outside the restrictions imposed, as in the above case of the two-dimensional separation, by the properties of the local or global structure of a disturbed flow. As a consequence of these restrictive conditions, which are sometimes difficult to reveal, only a certain boundary extremum for the indicated functional is realized.

ACKNOWLEDGMENTS

This work was supported by the Russian Foundation for Basic Research (project no. 00-01-00234) and the program “Universities of Russia—Fundamental Investigations” (project no. 99-1653).

REFERENCES

1. V. S. Dem’yanenko and V. A. Igumnov, Izv. Sib. Otd. Akad. Nauk SSSR, Ser. Tekh. Nauk, No. 8, 56 (1975).
2. M. A. Zubin and N. A. Ostapenko, Izv. Akad. Nauk SSSR, Ser. Mekh. Zhidk. Gaza, No. 3, 51 (1979).
3. M. A. Zubin and N. A. Ostapenko, *Jet and Detached Flows* (Mosk. Gos. Univ., Moscow, 1979).
4. M. A. Zubin and N. A. Ostapenko, Izv. Akad. Nauk SSSR, Ser. Mekh. Zhidk. Gaza, No. 6, 43 (1983).
5. M. A. Zubin and N. A. Ostapenko, Dokl. Akad. Nauk **368**, 50 (1999) [Dokl. Phys. **44**, 626 (1999)].
6. M. A. Zubin and N. A. Ostapenko, Izv. Akad. Nauk, Ser. Mekh. Zhidk. Gaza, No. 3, 57 (2000).
7. M. A. Zubin and N. A. Ostapenko, Izv. Akad. Nauk SSSR, Ser. Mekh. Zhidk. Gaza, No. 3, 68 (1989).
8. M. A. Zubin and N. A. Ostapenko, Izv. Akad. Nauk, Ser. Mekh. Zhidk. Gaza, No. 2, 137 (1992).
9. G. N. Abramovich, *Applied Gas Dynamics* (Nauka, Moscow, 1976).
10. G. I. Petrov, V. Ya. Likhushin, I. P. Nekrasov, and L. I. Sorkin, *Effect of Viscosity on Supersonic Stream with Compression Shocks*, Preprint No. 224, TsIAM (Tsentral’nyĭ Inst. Aviatsionnykh Motorov, Moscow, 1952).
11. N. A. Ostapenko, Dokl. Akad. Nauk **372**, 181 (2000) [Dokl. Phys. **45**, 225 (2000)].
12. I. R. Prigogine, *Introduction to Thermodynamics of Irreversible Processes* (Interscience, New York, 1968).
13. L. V. Gogish, V. Ya. Neĭland, and G. Yu. Stepanov, in *Itogi Nauki Tekh., Ser.: Gidromekh.* (VINITI, Moscow, 1975), Vol. 8.

Translated by V. Tsarev

Doklady Physics, Vol. 47, No. 3, 2002, pp. 229–232. Translated from Doklady Akademii Nauk, Vol. 383, No. 1, 2002, pp. 57–60.

MECHANICS

Stability of Steady-Flows of Two Ideal Fluids with Different Constant Densities

V. I. Sedenko

Presented by Academician I.I. Vorovich July 4, 2001

Received August 22, 2001

In this paper, the stability of steady flows in the system of two ideal fluids with different constant densities is analyzed with allowance for surface tension at their interface. The analysis is based on the abstract scheme proposed by Arnol'd [1, 2]. The fluids in this system can have free boundaries. It is shown that the well-known Rayleigh–Taylor instability is compensated for certain vortex flows by vorticity and surface tension.

The method reported in [1, 2] was used in [3] to analyze the stability of steady flows of an ideal fluid with a free boundary.

It was shown that, among all fields with the same vorticity, only the velocity fields for steady flows correspond to the critical points of kinetic energy (as well as to the critical points of the momentum and angular momentum functionals if the flow is invariant under translations and rotations, respectively). If the critical point is the nondegenerate maximum or minimum for the connective of integrals at the layer of flows with the same vorticity, the corresponding flow is stable.

1. THE EULER EQUATIONS FOR FLOWS OF AN IDEAL INHOMOGENEOUS FLUID WITH A PIECEWISE CONSTANT DENSITY

Let a time-dependent domain $D(t)$ in the three-dimensional space R^3 have the boundary $\partial D(t) = S_1 \cup S_2(t)$ and be filled with two ideal fluids with the interface $S_3(t)$, where S_1, $S_2(t)$, and $S_3(t)$ at any t consist of a finite number of connected closed disjoint surfaces. Here, S_1 is a set of rigid walls and $S_2(t)$ is the free boundary. The fluid is subjected to the bulk forces with potential $U(x)$ and to the capillary forces with the surface tension $\sigma \geq 0$. Then, velocity $V_i(x, t)$ and pressure $p_i(x, t)$ in the domain $D_i(t)$ for each t value satisfy the Euler equation

$$\rho_i(V_{it} + (V_i, \nabla)V_i) = -\mathrm{grad}(U + p_i), \quad \mathrm{div}V_i = 0; \quad (1)$$

the kinematic boundary conditions

$$\begin{aligned} V_{in}(x, t) &= 0, \quad x \in S_i, \\ V_{in}(x, t) &= \chi_{in}(x, t), \quad x \in S_3(t); \end{aligned} \quad (2)$$

and the dynamic boundary conditions

$$\begin{aligned} p_i(x, t) &= 2\sigma H(x, t), \quad x \in S_2(t), \\ p_i(x, t) &= p_j(x, t) + 2\sigma H(x, t), \\ x &\in S_3(t), \quad i, j = 1, 2. \end{aligned} \quad (3)$$

Here, $H_k(x, t)$ is the average curvature of the surfaces $S_k(t)$ at the point x [the average curvature is expressed in terms of the principal radii of curvature by the relationship $H = 2^{-1}(R_1^{-1} + R_2^{-1})$], χ_{in} denotes the normal component of the velocity of a point at the boundary of domain $D_k(t)$, and the subscript takes the values $k = 2. 3.$

2. CONFIGURATION SPACE

A flow is referred to as steady flow when domains D_i^0 filled with corresponding homogeneous fluids and velocity fields V_i^0, $i = 1, 2$, are independent of time t. Now, we define the configuration space M^0 corresponding to the steady flow $\{(D_i^0, V_i^0): i = 1, 2\}$, the stability of which will be studied. Let M be a manifold formed by sets of pairs $\{(D_i, V_i): i = 1, 2\}$, where D_i is a domain, V_i is a solenoidal vector field in the domain D_i, $i = 1, 2$, and $V_{im}(x) = V_{jn}(x)$, $x \in D_i \cap D_j$. We have $\{(D_i, V_i)\} \in M^0$ if there exists a set of maps g_i, $i = 1, 2$, such that

(1) g_i diffeomorphism of the domain D_i^0 into D_i conserves a volume element;

(2) $g_i S_1 = S_1$;

(3) $g_i S = g_j S$, where $S \subset \partial D_i^0 \cap \partial D_j^0$, $i, j = 1, 2$.

Rostov State University of Economics,
ul. Bol'shaya Sadovaya 69,
Rostov-on-Don, 34400 Russia

1028-3358/02/4703-0229$22.00

3. FUNCTIONALS OF ENERGY, MOMENTUM, AND ANGULAR MOMENTUM

Set (1) with boundary conditions (2) and (3) has the total-energy integral

$$E = \sum_{i=1}^{2} \int_{D_i(t)} \frac{1}{2}\rho_i V_i^2 dx + \int_{D(t)} U dx + \sum_{k=2}^{3} \sigma \oint_{S_k(t)} ds, \quad (4)$$

which is the sum of the kinetic energy, potential energy of the field of bulk forces, and surface energy of capillary forces. For each element $\{(D_i, V_i): i = 1, 2\}$, Eq. (4) determines the energy functional. If the rigid walls are invariant under translations along the OX axis or to rotations about the OX_3 axis, it is possible to define the momentum functional with respect to the OX_1 axis

$$L_1 = \sum_{i=1}^{2} \int_{D_i} \rho_i V_i e_1 dx$$

or the angular momentum functional with respect to the OX_3 axis

$$K_3 \sum_{i=1}^{2} \int_{D_1(t)} \rho_i V_i \times R \cdot e_3 dx, \quad R = (x_1, x_2, x_3),$$

respectively.

4. THE INVARIANT FOLIATION ON M^0

Generalizing the definition from [3], we refer to elements $\{(D_i, V_i)\}$ $\{(D_i', V_i')\}$ as elements with equal vorticity if there exists a set of maps g_i, $i = 1, 2$, such that

(1) g_i diffeomorphism of the domain D_i into D_i' conserves a volume element;

(2) $g_i S_i = S_1$;

(3) $g_i S = g_j S$, where $S \subset \partial D_i \cap \partial D_j$, $i, j = 1, 2$;

(4) the equality

$$\oint_{r_i} V_i dx = \oint_{g_i r_i} V_i' dx, \quad i = 1, 2$$

is satisfied for any closed path γ_i in the domain D_i.

Thus, we define the invariant Helmholtz–Thomson foliation on M^0, i.e., the partition into the classes of equivalence: two elements belong to one layer if and only if their vorticities are equal. The invariance of this foliation for the aforementioned dynamic system is the essence of the Helmholtz–Thomson theorem on the vortex conservation.

Theorem 1. *Let $V_i(x, t)$ satisfy Eqs.* (1)–(3) *in the domain $D_i(t)$ for all $t \in (-\delta$ and $\delta)$ and $x_i(t)$ be the path of a fluid particle. Then,*

$$\{(D_i(0), V_i(x, 0))\} \text{ and } \{(D_i(t), V_i(x, t))\}$$

have equal vorticities, and the map g_i transforms $x_i(0)$ into $x_i(t)$. The subscript takes the values $i = 1, 2$.

5 VARIATIONS OF ELEMENTS FROM M^0 ALONG THE LAYERS OF THE INVARIANT FOLIATION

Let solenoidal vector fields $f_i(x, \tau)$ defined in the neighborhoods of $D_i(0)$ be such that $g_{i\tau}(x_i(0)) = x_i(\tau)$ is a solution of the set of differential equations

$$\frac{dx_i}{d\tau} = f_i(x, \tau), \quad i = 1, 2.$$

The following conditions are satisfied: $f_{in}(x, \tau) = 0$, $x \in S_1$; $f_{in}(x, \tau) = f_{jn}(x, \tau)$; $x \in \partial D_i(\tau) \cap \partial D_j(\tau)$; $i, j = 1, 2$.

Similar to [3], it can be shown that velocity variations have the form

$$\delta V_i = \frac{\partial}{\partial \tau}\bigg|_{\tau=0} V_i(x, \tau) = f_i \times r_i + \text{grad}\alpha_i' + \text{grad}\beta_i^1, \quad (5)$$

$$\delta^2 V_i = \frac{1}{2}\frac{\partial^2}{\partial \tau}\bigg|_{\tau=0} V_i(x, \tau) = \frac{1}{2}[f_i \times \{f_i, r_i\} + \varphi_i \times r_i] + \text{grad}\alpha_i^2 + \text{grad}\beta_i^2. \quad (6)$$

Here, α_i^1 and α_i^2 are determined by the conditions

$$\text{div}\delta V_i = \text{div}\delta^2 V_i = 0, \quad (7)$$

$$\frac{d}{d\tau}\bigg|_{\tau=0} V_i(g_{i\tau}x, \tau) n(g_{i\tau}x, \tau) = 0, \quad (8)$$

$$\frac{d^2}{d\tau^2}\bigg|_{\tau=0} V_i(g_{i\tau}x, \tau) n(g_{i\tau}x, \tau) = 0, \quad (9)$$

where $r_i(x) = \text{curl}V_i(x, 0)$, $\{f_i(x, 0), r_i(x)\}$ is the Poisson bracket for the vector fields $f_i(x, 0)$ and $r_i(x)$; $\varphi_i(x) = \frac{\partial}{\partial \tau}\big|_{\tau=0} f_i(x, \tau)$; and $i = 1, 2$. In Eqs. (8) and (9), $x \in \partial D_i(0)$, and $n(g_{i\tau}x, \tau)$ is the unit vector of the outer normal to $\partial D_i(\tau)$ at the point $g_{i\tau}x$, $i = 1, 2$. In Eqs. (5) and (6), β_i^1 and β_i^2 are harmonic functions in the domain D_i, $i = 1, 2$. At the interfaces between fluid particles of different densities, the following conditions should be satisfied:

$$\begin{aligned} \text{grad}\beta_i^1(x) \cdot n(x) &= \text{grad}\beta_j^1(x) \cdot n(x), \\ \text{grad}\beta_i^2(x) \cdot n(x) &= \text{grad}\beta_j^2(x) \cdot n(x), \end{aligned} \quad (10)$$

where $x \in \partial D_i \cap \partial D_j$ and $n(x)$ is the unit vector of the outer normal to ∂D_i at the point x.

6. VARIATIONAL PRINCIPLES FOR THE ENERGY FUNCTIONAL

Theorem 2. *Let* $\{(D_i^0, V_i^0): i=1, 2\}$ *be a steady flow of an ideal fluid. Then,* $\{(D_i^0, V_i^0): i=1, 2\}$ *is a critical point of the energy functional E at a layer of the invariant foliation; conversely, any critical point of the energy functional corresponds to a steady flow. If the steady flow is invariant under translations along the* OX_1 *axis, this flow is a critical point of the momentum functional* L_1 *at this layer. If the steady flow is invariant under rotations about the* OX_3 *axis, this flow is a critical point of the angular momentum functional* K_3 *at this layer.*

7. THE SECOND VARIATIONS OF ENERGY, MOMENTUM, AND ANGULAR MOMENTUM

Taking into account Theorem 2 and using Eqs. (5)–(10), we derive the following formulas for the second variation of the energy functional:

$$2\delta^2 E = \sum_{i=1}^{2}\int_{D_i}\rho_i[(f_i\times r_i + \operatorname{grad}(\alpha_i^1+\beta_i^1))^2 + V_i\times f_i\cdot\{f_i, r_i\}]dx$$
$$+\sum_{i=1}^{2}\int_{\partial D_i}\Big[\Big(2\rho_i V_i(f_i\times r_i + \operatorname{grad}(\alpha_i^1+\beta_i^1)) + \operatorname{grad}\Big(\rho_i\frac{V_i^2}{2}+U\Big)\cdot f_i\Big)f_{in} + \sigma(\nabla(f_{in}, f_{in}) + (2K-4H^2)(f_{in})^2)\Big]ds$$

and momentum functional

$$2\delta^2 L_1 = \sum_{i=1}^{2}\Big(\int_{D_i}\rho_i e_i\times f_i\cdot\{f_i, r_i\}dx + \int_{\partial D_i}[2\rho_i(f_i\times r_i + \operatorname{grad}(\alpha_i^1+\beta_i^1))\cdot e_1 + \operatorname{grad}(\rho_i V_i e_1)f_i]f_{in}ds\Big),$$

where e_1 is the unit vector of the OX_1 axis.

The formula for $\delta^2 K_3$ is similarly derived and has a similar form.

8. THE STABILITY CRITERION

Theorem 3. *If some linear combination of second variations,*

$$\mu_i\delta^2 E + \mu_2\delta^2 L_1 + \mu_3\delta^2 K_3, \tag{11}$$

taken along the Helmholtz layer at the point $\{(D_i^0, V_i^0): i=1, 2\}$ *corresponding to a steady flow of an ideal fluid with piecewise constant density is a fixed-sign quadratic form of* f_i *and* $\operatorname{grad}\beta_i^1$, $i = 1, 2$, *then the steady flow is stable under small finite perturbations of the velocity* V_i^0, *vortex* r_i^0, *and domain boundary* ∂D_i^0, $i = 1, 2$.

9. STABILITY OF FLOWS IN A TWO-LAYER FLUID

Let us consider a plane-parallel flow in a layer where the straight lines $y = 0$ and $y = a$ correspond to rigid walls and the straight line $y = y_1$ $(0 < y_1 < a)$ is the interface between fluid particles with the densities ρ_1 and ρ_2 and velocity profiles $u_1(y)$ and $u_2(y)$ in the upper and lower layers, respectively. We analyze the stability of this flow under perturbations periodic in x with the period X.

9.1 Flows in a Rigid-Wall Channel with High Surface Tension at the Interface

In this case, the second energy variation has the form

$$2\delta^2 E = \sum_{i=1}^{2}\int_{D_i}\rho_i\Big[\delta(V^0)^2 + \frac{u_i}{u_i''}(\delta r_i^0)^2\Big]dxdy + \int_{y=y_1}\Big[2\rho_1 u_1(y_1)\delta V_{11}^0 f_{12} - 2\rho_2 u_2(y_1)\delta V_{21}^0 f_{22} + \frac{\partial}{\partial y}\Big(\rho_1\frac{u_1^2}{2}\Big)(f_{12})^2 - \frac{\partial}{\partial y}\Big(\rho_2\frac{u_2^2}{2}\Big)(f_{22})^2 + \sigma\Big(\Big(\frac{\partial f_{12}}{\partial x}\Big)^2 + \Big(\frac{\partial f_{22}}{\partial x}\Big)^2\Big)\Big]dx. \tag{12}$$

For Eq. (12) to be positive definite, the condition

$$\frac{u_1(y)}{u_1''(y)} > 0, \quad y\in[0, y_1], \quad \frac{u_2(y)}{u_2''(y)} > 0, \quad y\in[y_1, a]$$

and the following conditions at the $y = y_1$ interface

$$\sigma > C(X; u_i(y_1), u_i''(y_1), \rho_i, i = 1, 2)$$

should be satisfied. If surface tension increases at the interface, we will eventually obtain all flows with profiles minimizing the energy functional in the situation when the interface is replaced by a rigid wall.

9.2. Flows in a Rigid-Wall Channel with High Surface Tension at the Interface

Let us set $\mu_1 = 2$, $\mu_2 = -2c$, and $\mu_3 = 0$ in Eq. (11) assuming that $u_1(y_1) = u_2(y_1) = c$. Then, we have the square form

$$2\delta^2 E - 2c\delta^2 L_1 = \sum_{i=1}^{2} \int_{D_j} \rho_i \left[(\delta V_i^0)^2 + \frac{u_i(y) - c}{u_i'(y)} (\delta_i^0)^2 \right] dx dy + \sigma \int_{y = y_1} \left[\left(\frac{\partial f_{12}}{\partial x} \right)^2 + \left(\frac{\partial f_{22}}{\partial x} \right)^2 \right] dx, \quad (13)$$

which is positive definite if each velocity profile satisfied the conditions

$$\frac{u_i(y) - c}{u_i''(y)} > 0, \quad i = 1, 2.$$

Note that the stability conditions for low surface tension are satisfied only when the velocity is continuous at the interface. Thus, bulk forces that can stabilize a flow with a free boundary [3] cannot stabilize a flow with an interface.

ACKNOWLEDGMENTS

The work was supported in part by the U. S. Civilian Research and Development Foundation for the Independent States of the Former Soviet Union, grant no. RM1-2084. I am grateful to I.I. Vorovich, V.I. Yudovich, and A.B. Morgulis for helpful discussions.

REFERENCES

1. V. I. Arnol'd, Prikl. Mat. Mekh. **29**, 846 (1965).
2. V. I. Arnol'd, Dokl. Akad. Nauk SSSR **162**, 975 (1965).
3. V. I. Sedenko and V. I. Yudovich, Prikl. Mat. Mekh. **42**, 1050 (1978).

Translated by K. Kugel'

Doklady Physics, Vol. 47, No. 3, 2002, pp. 233–237. Translated from Doklady Akademii Nauk, Vol. 383, No. 1, 2002, pp. 61–66.

MECHANICS

New Stationary Solutions to the Problem of Three Vortices in a Two-Layer Fluid

M. A. Sokolovskiĭ* and J. Verron**

Presented by Academician V.V. Kozlov September 4, 2001

Received September 6, 2001

1. The universally integrable problem of three vortices [1, 4–6] has attracted the interest of researchers for over one hundred years [6]. This is not associated only with the vortex problem in itself but also has numerous analogies in the mechanics of solids, astrophysics, the dynamics of superfluid helium, and mathematical biology [1, 5]. A new peak of interest in this problem was stimulated by the discovery of so-called three-polar structures [13], i.e., symmetric triples of vortices $(-\kappa, 2\kappa, -\kappa)$ and by later observation of their spontaneous origin from chaos [12]. In most studies [1, 4–7, 10, 12–15], the dynamics of vortices was analyzed in the framework of the homogeneous-fluid model. At the same time, the geophysical problems (some of them were discussed in [2, 3, 8, 11]) are characterized by noticeable density stratification. In this paper, we analyze the problem of three vortices that exist in a two-layer fluid and have zero total intensity.

2. We take the following assumptions: (i) the upper and lower layers have equal thickness values ($h_1 = h_2 = 1/2$) and the densities ρ_1 and ρ_2 in the layers satisfy the condition $\Delta\rho = \rho_2 - \rho_1 > 0$; and (ii) one vortex with an intensity κ_1^1 corresponds to the upper layer, whereas two vortices with intensities κ_2^1 and κ_2^2 are located in the lower layer. The complex form of equations of motion for three discrete vortices in two immiscible fluid layers rotating with a constant angular velocity (in the presence of a hard cap on the upper surface) is

$$\frac{d\bar{z}_1^1}{dt} = \frac{1}{2\pi i}\sum_{j=1}^{2}\frac{\kappa_2^j}{z_2^j - z_1^1}[1 - \gamma|z_2^j - z_1^1|K_1(\gamma|z_2^j - z_1^1|)], \quad (1)$$

$$\frac{d\bar{z}_2^m}{dt} = \frac{1}{2\pi i}\left\{\frac{\kappa_1^1}{z_1^1 - z_2^m}[1 - \gamma|z_1^1 - z_2^m|K_1(\gamma|z_1^1 - z_2^m|)] + \frac{\kappa_2^{3-m}}{z_2^{3-m} - z_2^m}[1 + \gamma|z_2^{3-m} - z_2^m|K_1(\gamma|z_2^{3-m} - z_2^m|)]\right\}. \quad (2)$$

Here, $z_n^m = x_n^m + iy_n^m$ is the complex coordinate of the mth vortex in the nth layer; the overbar implies complex conjugation; the parameter γ is inversely proportional to the Rossby internal deformation radius

$$\lambda = \left[\frac{g\Delta\rho h_1 h_2}{\rho_0 f^2(h_1 + h_2)}\right]^{1/2};$$

K_k is the kth-order modified Bessel function of the second kind; g is the acceleration of gravity; and f is the Coriolis parameter equal to the double angular velocity of the fluid-plane rotation about a normal to this plane. According to assumption (ii) above, the variable m in Eq. (2) takes the values 1 and 2. Thus, Eqs. (1), (2) are the set of ordinary differential equations that should be complemented by initial conditions for the original coordinates of all three vortices.

The set of Eqs. (1), (2) can be represented in the standard Hamiltonian form with the Hamiltonian

$$H = -\frac{1}{2\pi}\{\kappa_2^2\kappa_2^1[\ln d_{22}^{12} - K_0(\gamma d_{22}^{12})] + \kappa_1^1\kappa_1^1[\ln d_{21}^{11} + K_0(\gamma d_{21}^{11})] + \kappa_1^1\kappa_2^2[\ln d_{21}^{21} + K_0(\gamma d_{21}^{21})]\}, \quad (3)$$

where $d_{kl}^{mn} = |z_l^n - z_k^m|$. In addition to Hamiltonian (3), the original set has the first integrals for the momenta

$$P = \kappa_1^1 z_1^1 + \kappa_2^1 z_2^1 + \kappa_2^2 z_2^2, \quad \bar{P} = \kappa_1^1\bar{z}_1^1 + \kappa_2^1\bar{z}_2^1 + \kappa_2^2\bar{z}_2^2$$

and the angular momentum

$$M = \kappa_1^1|z_1^1|^2 + \kappa_2^1|z_2^1|^2 + \kappa_2^2|z_2^2|^2,$$

whose values are evidently determined by the initial conditions.

* *Water Problems Institute, Russian Academy of Sciences, Novaya Basmannaya ul. 10, Moscow, 107078 Russia*
E-mail: m_sokolovskiy@mail.ru

** *Laboratoire de Geophysique et Industriel Courants, Centre National de la Recherche Scientifique, Grenoble, France*
E-mail: verron@hmg.inpg.fr

1028-3358/02/4703-0233$22.00

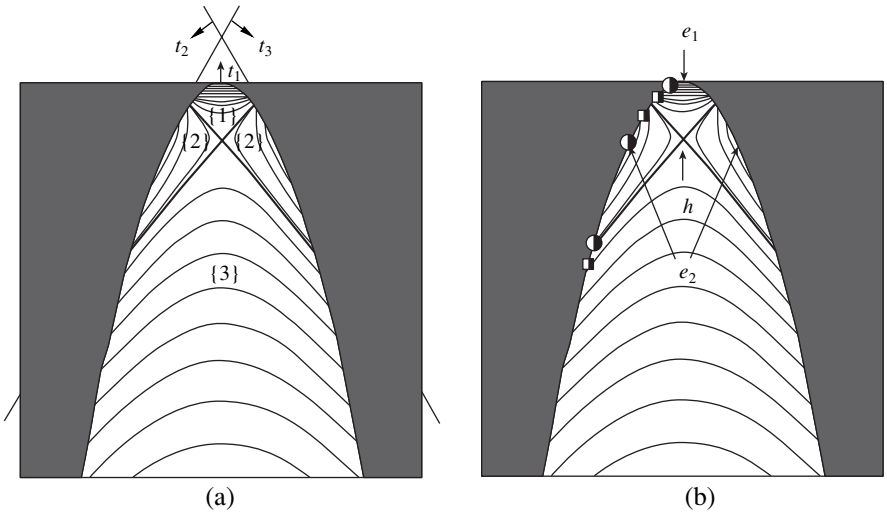

Fig. 1. (a) Phase portrait of the relative motion for a three-vortex system in a two-layer fluid under conditions (4) and $P = 1.7$. Thick lines are separatrices that separate the regions of different types {1}, {2}, and {3} of interactions between the vortices. The dark region is the nonphysical region of the phase plane (axes of trilinear coordinates are also shown). (b) The same as in Fig. 1a with the singular points indicated. Squares and circles on the boundary of the physical region correspond to the coordinates of the representation points in the phase space for the original configurations of the vortices in the numerical calculations presented in Figs. 2 and 3, respectively.

It is easy to verify that the invariants H, M, and $P \cdot \bar{P}$ are in involution, and therefore set (1), (2) always has a regular solution [1, 4].

In what follows, we assume that the total intensity of vortices is zero and

$$\kappa_1^1 = -2\kappa, \quad \kappa_2^1 = \kappa_2^2 = \kappa > 0. \tag{4}$$

Thus, the upper-layer vortex is attributed to the anticyclonic vorticity compensated by the two cyclones in the lower layer.

3. We now assume that $P \neq 0$. In this case, the relative motion can be analyzed in the trilinear coordinates [1, 7, 15]

$$t_1 = -\frac{3\kappa_2^1\kappa_2^2(d_{22}^{21})^2}{P^2}, \quad t_2 = -\frac{3\kappa_1^1\kappa_2^2(d_{21}^{21})^2}{P^2},$$

$$t_3 = -\frac{3\kappa_1^1\kappa_2^1(d_{21}^{11})^2}{P^2},$$

which possess the obvious property

$$t_1 + t_2 + t_3 = 3.$$

In the plane specified by the coordinates t_1, t_2, t_3 (whose meaning is illustrated in Fig. 1a), it is necessary to separate so-called physical regions where the triangle inequality is satisfied. Under condition (4), this implies that

$$12t_1 + (t_2 - t_3)^2 \leq 0 \text{ for } t_1 < 0, \quad t_2 \geq 0, \quad t_3 \geq 0.$$

In the trilinear coordinates, the isolines of Hamiltonian (3) coincide with those of the function

$$W(t_1, t_2, t_3) = \ln\left[\frac{-t_1}{t_2 t_3}\right]$$

$$-2\left[K_0\left(\gamma\sqrt{\frac{-t_1P^2}{3\kappa^2}}\right) + 2K_0\left(\gamma\sqrt{\frac{t_2P^2}{6\kappa^2}}\right) + 2K_0\left(\gamma\sqrt{\frac{t_3P^2}{6\kappa^2}}\right)\right].$$

In essence, these isolines are the phase trajectories for the relative motion of the three-vortex system under consideration and are shown in Fig. 1 for $P = 1.7$.

The basic general properties of the phase curves are the following.

(I) All the phase curves start and finish at the physical-region boundary. Therefore, all relative motions of vortices are periodical, and vortices pass through two collinear positions during a period. From this, it follows that exhaustive information on possible motions of the system of vortices can be acquired from the initial condition for three vortices being located in the same straight line.

(II) Possible motions for the system of three vortices can be classified into three qualitatively different types according to the initial collinear configuration of vortices.

(III) The phase portrait can have singular points of elliptic (e) and hyperbolic (h) types (see Fig. 1b).

(IV) The phase curves are symmetric about the straight line $t_2 = t_3$, because the variables t_2 and t_3 are proportional to the distances squared between the anticyclone of the upper layer and equivalent (with each other) cyclones of the lower layer.

The phase portraits (we present here only one example for a particular value of the system momentum) provide total information on the relative motion of the system of vortices. However, it is known that this analysis does not reveal all characteristic properties of the absolute motion of vortices [5]. Below, the basic features of the vortices are analyzed on the basis of numerical calculations. We also present the trajectories of vortices, indicating (by markers) their synchronous collinear positions additionally marked by segments passing through these positions. Without loss of generality, the original positions of vortices are attributed to the *x*-axis. We take $\bar{x}_1^1 = \bar{x}_2^1 = 0$ (one of the lower-layer vortices is exactly under the upper-layer vortex) and $\bar{x}_2^2 \neq 0$ as the simplest (reference) original positions of the vortices x_1^1, x_2^1, and x_2^2, respectively. In this case, the momentum P of the system of vortices is completely determined by the initial vortex position $\bar{x}_2^2$. At the same time, the sets of coordinates

$$x_1^1 = \bar{x}_1^1, \quad x_2^1 = \bar{x}_2^1 - x_0, \quad x_2^2 = \bar{x}_2^2 + x_0, \qquad (5)$$

conserve the given P value for all x_0. An arbitrary set of numerical experiments with initial conditions (5) for fixed $\bar{x}_2^2$ corresponds to a specific phase portrait (e.g., that presented in Fig. 1). In what follows, we also use the notation $X_0 = \gamma x_0$ and $X_n^m = \gamma x_n^m$ along with x_0 and x_n^m.

The trajectories and vortices (for their collinear positions) are shown in Figs. 2 and 3 by solid lines and triangles for the upper-layer vortex x_1^1, by long dashes and circles for x_2^1, and by short dashes and squares for x_2^2. The size of a marker is proportional to the intensity of the corresponding vortex. We imply the upward translational motion everywhere. In figure captions, the notation $t = (t_1, t_2, t_3)$ is used.

4. Figure 2 shows characteristic examples of motions for each of three types.

For type {1} (see Fig. 2a), the interaction between the lower-layer vortices is predominant. The system of vortices moves in the direction perpendicular to the *x*-axis. In this case, the anticyclonic vortex of the upper layer undergoes small periodic deviations from the rectilinear motion. The lower-layer vortices revolve in the cyclonic direction around a certain center moving translationally so that the vortices change their places in the collinear positions for each half-period.

Motions of type {2} are characterized by dominating interactions between the upper-layer vortex and one of the lower-layer vortices, which was initially located closer to the upper-layer vortex.

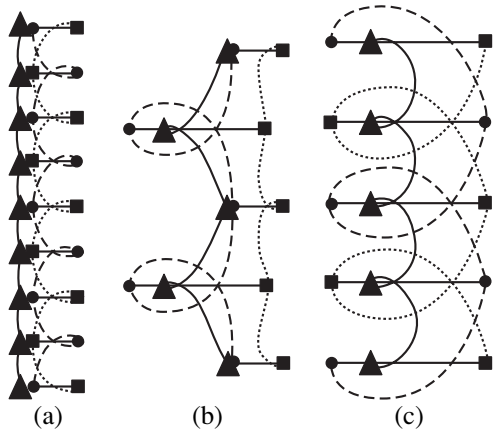

Fig. 2. Trajectories of absolute motion for $P = 1.7$. The initial conditions are specified by Eqs. (5) for $\bar{X}_1^1 = \bar{X}_2^1 = 0$; $\bar{X}_2^2 = 1.7$; X_0 = (a) –0.3, (b) –0.2, (c) 1.1; and (a) t = (–1.2561, 4.0692, 0.1869), (b) (–1.7543, 4.6713, 0.0830), and (c) (–15.7889, 16.2768, 2.5121).

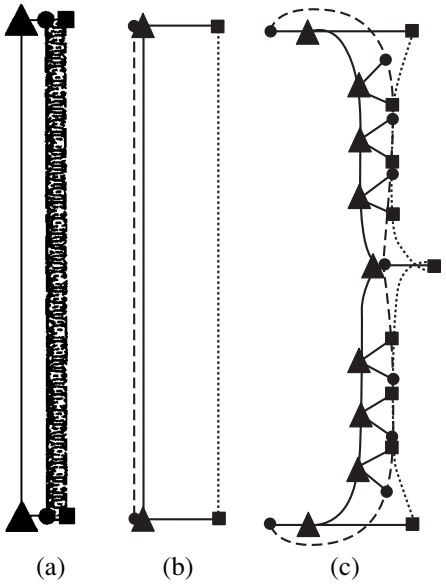

Fig. 3. The same as in Fig. 2, but for (a) X_0 = –0.6, (b) 0.2062, and (c) 0.9611 and (a) t = (–0.2595, 2.5121, 0.7474), (b) (–4.6321, 7.5438, 0.0883), (c) (–13.6197, 14.7020, 1.9177).

According to Fig. 2c, solutions of type {3} are featured by anticyclonic revolutions of all three vortices. This is caused by the defining role of the upper-layer vortex.

The cyclicity periods for vortices in the upper and lower layers relate to each other as 1 : 2 for motions of types {1} and {3}, whereas these periods coincide in the case of type {2}. This difference is explained by the fact that each phase curve of types {1} and {3} is mirror symmetric, whereas the curve of type {2} is asymmetric.

The examples of phase curves presented in Fig. 2 correspond to the conditions when they pass far from the separatrices and singular points. However, the stationary solutions corresponding to singular points are of the most interest.

In the vicinity of the singular point e_1, the lower-layer vortices approach each other at an infinitesimal distance and should orbit a common center with a (theoretically) infinite angular velocity. In this case, interlayer interaction is manifested almost exclusively as the linear displacement of the entire configuration. In essence, the limiting-case structure is equivalent to a two-layer pair of vortices of intensities -2κ and 2κ in the upper and lower layers, respectively. The motion with characteristics close to those described above is exemplified in Fig. 3a, where $\gamma d_{22}^{12} = 0.5$ is not small. (The lower-layer vortices undergo 66 revolutions during the calculation time; to avoid overloading, we mark in the figure only the original and final collinear positions of the vortices.) With a decrease in the original distance between the lower-layer vortices, the pattern becomes less instructive. For this reason, the results of corresponding calculations are not presented.

We now consider a point e_2 belonging to the boundary of the physical region (see Fig. 1b). As is known [1], the collinear three-vortex configurations corresponding to such singular points should revolve around the vorticity center. The presence of these elliptic points under the condition of the zero total intensity of the system is a remarkable (and surprising) property of the two-layer configuration. Since, in this case, the vorticity center moves to an infinitely far point, the collinear configuration of the three vortices, as a pair of vortices, should move uniformly and rectilinearly in the direction normal to the straight line in which vortices lie (a corresponding example is shown in Fig. 3b). This configuration, naturally referred to as a triton, can be the simplest example of the vortex structures referred to as a modon with a raider [9].

A hyperbolic point h apparently corresponds to the unstable solution associated with the translationally moving configuration in the form of an isosceles triangle ($t_2 = t_3$). This configuration is illustrated in Fig. 3c exhibiting trajectories of the vortex-structure motion for which the representation point in the phase plane is originally located at the boundary of the physical region near the separatrix. The markers (positions of vortices) and segments connecting them in this figure indicate not only collinear but also other synchronous intermediate vortex configurations for time intervals during which the representation point resides in the vicinity of the intersection point h of the separatrices. These unstable configurations obviously cannot be long-lived. As is seen in this figure, they periodically rearrange with alternation of the mutual positions of the lower-layer vortices after passing through collinear states.

5. The general conditions for the existence of these stationary solutions for an arbitrary momentum value of the system are the following.

5.1. Triangular configuration. From Eqs. (1) and (2), it is easy to derive the condition for the existence of the rectilinear motion of this vortex structure:

$$\frac{1 + 2L|\cos\varphi|K_1(2L|\cos\varphi|)}{\cos^2\varphi} = 4[1 - LK_1(L)] \quad (6)$$

with $L = \gamma l$, where l is the length of the lateral side of the isosceles triangle, as well as the expression for the velocity of this structure in the y direction parallel to the base of the triangle:

$$V = -\frac{\kappa\gamma\sin\varphi}{8\pi L}[1 - LK_1(L)]. \quad (7)$$

Equation (6) can be treated as a dispersion equation relating the length of the triangle lateral side to the angle φ adjacent the base. Equation (6) has a (unique) solution $L(\varphi)$ only in the interval $|\varphi| < \pi/3$; i.e., the triangle cannot be equilateral (more exactly, the limiting value $|\varphi| = \pi/3$ is an asymptotic one as $L \longrightarrow \infty$ and $|V| \longrightarrow 0$).[1] The velocity of the triangular structure coincides with that of a certain hypothetical pair consisting of vortices located in different layers, having intensities -2κ and 2κ, and spaced by the distance equal to the height of the corresponding isosceles triangle. Figure 4a shows the dispersion curve $L(\varphi)$ and $V(\varphi)$ (7). For $\varphi = 0$, we have $V = 0$, and L takes the value $L_0 = 0.8602$ at which the degenerate (to the segment) symmetric three-vortex configuration is stationary. The extremal values of V are attained for $|\varphi| = 0.82\pi/3$ and $L = 1.874$.

5.2. Collinear configuration. We now denote as A and B, respectively, the quantities X_2^1 and X_2^2 that are proportional to the original distances between the upper-layer vortex (for $X_1^1 = 0$) and its partners from the lower layer. From equations of motion (1), (2), we obtain the following conditions for the uniform motion of the entire configuration as a rigid body along the y axis:

$$\frac{A^2 + AB + B^2}{AB(A + B)} = K_1(A) + K_1(B) + K_1(A + B). \quad (8)$$

This equality can also be treated as a dispersion equation relating the geometric parameters of the solutions in the form of the translational collinear configurations. The translational velocity is expressed as

$$V = \frac{\kappa\gamma}{4\pi}\left[\frac{1}{A} - K_1(A) - \frac{1}{B} + K_1(B)\right]. \quad (9)$$

[1] In the homogeneous fluid [10], a similar stationary state is the configuration in the form of an equilateral triangle with an arbitrary side length.

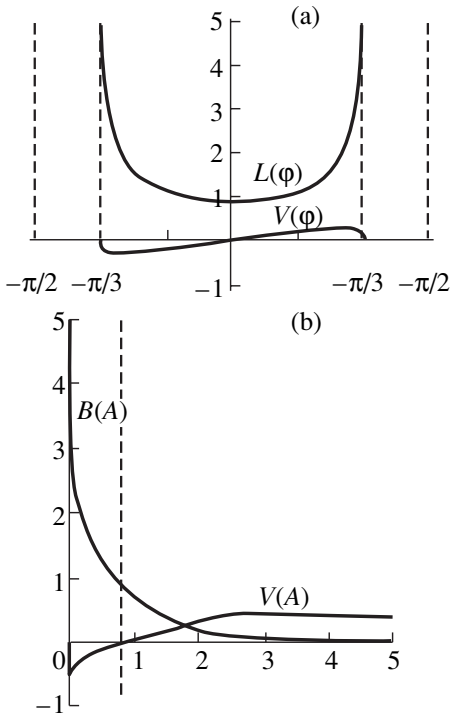

Fig. 4. Geometry parameters characterizing stationary solutions for the (a) triangular and (b) collinear configurations.

Figure 4b demonstrates dispersion curve (8) and vortex-structure velocity (9). In the asymptotic limit as $A \longrightarrow 0$ or $B \longrightarrow 0$, i.e., when the coordinates of a lower-layer vortex coincide with those of the upper-layer vortex, we have, respectively, $B \longrightarrow \infty$ and $A \longrightarrow \infty$. This implies that the second vortex in the lower layer is infinitely far away. The limiting velocity of the configuration also tends to zero but takes extremal values for A/B and $B/A = 0.0075$. The condition $A < B$ ($A > B$) leads to $V < 0$ ($V > 0$). For $A = B$, the velocity reverses its sign. In this case, the conditions $X_2^1 = X_2^2 = L_0$ are satisfied with the same value of L_0, which is observed when the triangular configuration with the symmetric location of the cyclonic vortices degenerates with respect to the upper-layer anticyclonic vortex (see Section 5.1).

6. In conclusion, we emphasize that, in the present study, modes intrinsic to the problem of a system of three vortices in a two-layer rotating fluid with layers of identical thickness values are classified for the case when the total intensity of the system is zero and the lower-layer vortices are equivalent to each other. New stationary solutions are obtained, and general conditions for their existence are found.

ACKNOWLEDGMENTS

We are grateful to V.M. Gryanik, J.B. Flór, V.N. Zyryanov, G.M. Reznik, and Z.I. Kizner for valuable discussions of the results of this study. The work of one of the authors (M.A.S.) was supported by the Russian Foundation for Basic Research (project no. 01-05-64646) and by the Centre National de la Recherche Scientifique, Grenoble, France.

REFERENCES

1. A. V. Borisov and I. S. Mamaev, *Poisson's Structures and Lie Algebras in Hamiltonian Mechanics* (Izd. Dom Udmurtskiĭ Univ., Izhevsk, 1999).
2. V. M. Gryanik, Izv. Akad. Nauk SSSR, Fiz. Atm. Okeana **19**, 227 (1983).
3. V. M. Gryanik, Izv. Akad. Nauk SSSR, Fiz. Atm. Okeana **24**, 1251 (1988).
4. V. V. Kozlov, *General Theory of Vortices* (Izd. Dom Udmurtskiĭ Univ., Izhevsk, 1998).
5. V. V. Meleshko and M. Yu. Konstantinov, *Dynamics of Vortex Structures* (Naukova Dumka, Kiev, 1993).
6. H. Poincaré, *Théorie des turbillions* (Georges Carré, Paris, 1893; Nauchno-Informatsionnyĭ Tsentr: Regulyarnaya i Khaoticheskaya Dinamika, Moscow–Izhevsk, 2000).
7. H. Aref, Phys. Fluids **22**, 393 (1979).
8. X. J. Carton and S. M. Correard, in *Proceedings of International Union of Theoretical and Applied Mechanics, Symposium on Separated Flows and Jets, Lyngby, Denmark, 1997* (Kluwer Acad. Publ., Lyngby, 1997).
9. G. R. Flierl, V. D. Larichev, J. C. McWilliams, and G. M. Reznik, Dyn. Atm. Oceans **5**, 1 (1980).
10. G. J. F. van Heijst, Meccanica **29**, 431 (1994).
11. N. G. Hogg and H. M. Stommel, Proc. R. Soc. London, Ser. A **397**, 1 (1985).
12. B. Legras, R. Santangelo, and R. Benzi, Europhys. Lett. **5**, 37 (1988).
13. C. E. Leith, Phys. Fluids **27**, 1388 (1984).
14. N. J. Rott, Appl. Math. Phys. (ZAMP) **40**, 473 (1989).
15. J. L. Synge, Can. J. Math. **1**, 257 (1949).

Translated by R. Tyapaev

Doklady Physics, Vol. 47, No. 3, 2002, pp. 238–240. Translated from Doklady Akademii Nauk, Vol. 383, No. 1, 2002, pp. 67–70.

MECHANICS

Three-Dimensional Contact Problem for a Layer with Allowance for Friction in an Unknown Contact Area

M. I. Chebakov

Presented by Academician I.I. Vorovich August 30, 2001

Received September 21, 2001

Taking friction forces into account, we investigate the interaction between an elliptic-paraboloid die and a layer. The investigation concerns the effects of the Coulomb friction coefficient, die shape, elastic constants, and layer thickness on contact stresses, the dependence of the vertical die displacement on a pressing force, the dimensions and shape of the contact area, and the displacement of layer-surface points outside the contact area. It is discovered that the contact-area shape and displacements of the surface points are qualitatively different at small and large values of the Poisson ratio.

We investigate the case of the limit equilibrium. Quasistatic die motion along the layer surface can be considered in a moving coordinate system in a similar way. The integral equation derived for the problem is solved by the method of nonlinear boundary integral equations [1, 2].

Friction forces were taken into account in two-dimensional contact problems [3, 4] and three-dimensional ones for a half-space [5–7] and a wedge [8, 9].

Let a rigid die lying on the layer surface $z = h$ be subjected to the normal force P and tangential force T directed along the Ox-axis of the Cartesian coordinate system (x, y, z) with the origin on the lower surface of the layer. Under the assumptions that the friction forces under the die are parallel to the force T, the layer surface $z = 0$ is rigidly fixed, and the die is in the limit-equilibrium state and does not rotate, we arrive at the boundary value problem presented by Lamé equations and the boundary conditions

$$\begin{gathered} w = \delta - f(x, y), \quad \tau_{xz} = \mu\sigma_z, \quad \tau_{yz} = 0, \\ z = h, \quad (x, y) \in \Omega, \\ \sigma_z = \tau_{xz} = \tau_{yz} = 0, \quad z = h, \quad (x, y) \notin \Omega, \\ u = \nu = w = 0, \quad z = 0. \end{gathered} \tag{1}$$

Here, u, ν, and w are the components of the displacement vector along the x-, y-, and z-axes, respectively; σ_z, τ_{xz}, and τ_{yz} are the components of the stress tensor; μ is the friction coefficient; δ is the die displacement; $f(x, y)$ is the shape of the die base; and Ω is the contact area.

In addition, we suppose the conditions of statics

$$P = \iint_\Omega \sigma_z(x, y, 0)\, d\Omega, \quad T = \mu P.$$

Representing the components of the displacement vector in the layer as double Fourier transforms in the coordinates x and y, we obtain the following integral equation for the unknown contact pressure $q(x, y)$ under the die:

$$\begin{gathered} \iint_\Omega q(\eta, \xi) k(x - \eta, y - \xi)\, d\eta\, d\xi = \frac{2\pi G}{1 - \nu}(\delta - f(x, y)), \\ (x, y) \in \Omega, \end{gathered} \tag{2}$$

where G is the modulus of elasticity in shear and ν is the Poisson ratio. The kernel $k(t, \tau)$ can be represented as the difference of two terms

$$k(t, \tau) = k_1(t, \tau) - \varepsilon k_2(t, \tau), \quad \varepsilon = \frac{\mu(1 - 2\nu)}{2 - 2\nu}. \tag{3}$$

Upon simplifying, these terms take the form

$$k_1(t, \tau) = \frac{1}{\sqrt{t^2 + \tau^2}} + \int_0^\infty (L_1(\gamma h) - 1) J_0(\gamma\sqrt{t^2 + \tau^2})\, d\gamma, \tag{4}$$

$$\begin{gathered} k_2(t, \tau) = \frac{1}{t^2 + \tau^2} \\ \times \left[1 + \int_0^\infty (L_2(\gamma h) - 1) J_1(\gamma\sqrt{t^2 + \tau^2})\, d\gamma\right], \end{gathered} \tag{5}$$

$$L_1(u) = \frac{2\kappa \sinh 2u - 4u}{2\kappa \cosh 2u + 4u^2 + 1 + \kappa^2},$$

$$L_2(u) = \frac{2\kappa(\cosh 2u - 1) - 4u^2(1 - 2\nu)^{-1}}{2\kappa \cosh 2u + 4u^2 + 1 + \kappa^2},$$

Institute of Mechanics and Applied Mathematics, Rostov State University, pr. Stachki 200/1, Rostov-on-Don, 344104 Russia

1028-3358/02/4703-0238$22.00

where $J_n(x)$ ($n = 0, 1$) are the Bessel functions, $\gamma = \sqrt{\alpha^2 + \beta^2}$, and $\kappa = 3 - 4\nu$.

We consider an elliptic-paraboloid die elongated along the y-axis. Then the function $f(x, y)$ on the right-hand side of Eq. (2) takes the form

$$f(x, y) = \frac{x^2}{2R_1} + \frac{y^2}{2R_2}, \quad R_2 \geq R_1,$$

where R_1 and R_2 are the radii of die curvature in the planes $y = 0$ and $x = 0$, respectively.

It should be noted that integral equation (2) involving only the kernel $k_1(t, \tau)$ corresponds to the contact problem of the frictionless indentation of a die into a layer [10].

Integral equation (2) with kernels (4) and (5) needs to be complemented not only by the conditions of statics but also by a condition for finding the contact area. This condition will be formulated and realized when solving the equation.

When the layer thickness is $h \longrightarrow \infty$, integral terms in kernels (4) and (5) vanish and Eq. (2) coincides with the integral equation of the similar half-space problem considered in [5].

Integral equations (2) are solved here by the method of nonlinear boundary conditions [1, 2]. This method enables us to simultaneously find the distribution function of contact stresses, the contact area, and the displacements of the layer-surface points outside the die in a certain region containing the contact area.

Omitting the details of the method, we note that it was previously applied to the problems where the die displacement was given, whereas other quantities including forces on the die were sought [1, 2, 8, 9, 11]. Here, we use a more natural modification of the method in which forces applied to the die are given, whereas die displacement is determined by solving the problem.

Certain results of the numerical calculations are presented below. The accuracy of the results was checked by comparing them for different numbers of discretization nodes of the nonlinear integral equation that was taken from [1, 2], equivalent to Eq. (2), and involving a condition for determining the contact area. In addition, the results were compared with the known particular cases for $\mu = 0$ [10, 12].

Our numerical calculations show that the die displacement δ at a given force P is almost independent of the friction coefficient μ but depends strongly on the Poisson ratio ν and other parameters. Table 1 presents the die displacement $\delta^* = \delta \times 10^{-3}$ calculated at $P = 10^7$, $\mu = 0.9$, $R_1 = R_2 = 1.0$, and indicated values of the Poisson ratio ν, shear modulus G, and layer thickness h. We note that variations in P and G such that P/G = const leave the results unchanged. Here and below, dimensional quantities are presented in the International System of Units.

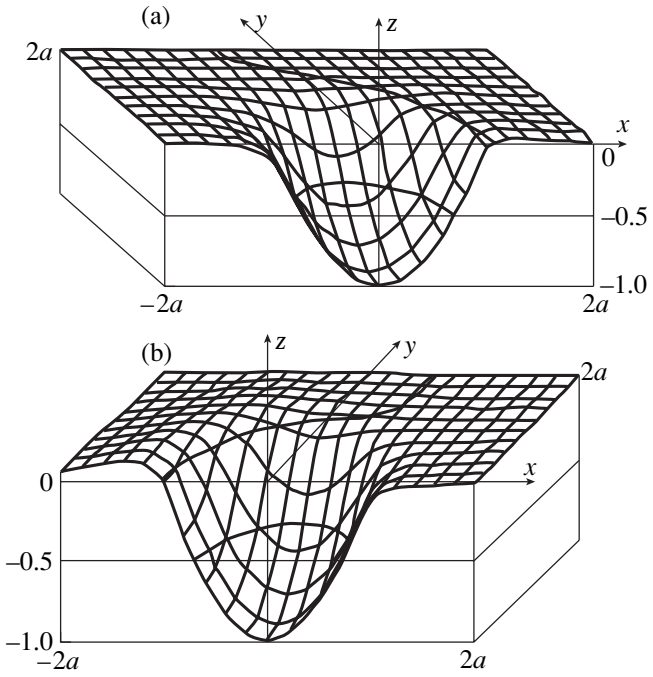

Fig. 1. The deformed surface $z = h$ in the vicinity of the die at $|x| \leq 2a$, $0 \leq y \leq 2a$ for (a) $\nu = 0.1$ and (b) 0.4.

According to Table 1, the die displacement δ calculated at the constant force P decreases as the Poisson ratio ν increases or the layer thickness h decreases.

Table 1

$G \times 10^{-10}$	ν	h				
		0.5	0.2	0.1	0.05	0.02
7.0	0.1	1.29	1.21	1.09	0.907	0.617
	0.3	1.08	1.01	0.912	0.750	0.504
	0.4	0.967	0.906	0.811	0.657	0.430
1.0	0.1	4.52	4.04	3.36	2.55	1.65
	0.3	3.79	3.37	2.79	2.10	1.34
	0.4	3.39	2.99	2.45	1.80	1.10

Table 2

$P \times 10^{-7}$	1.0	2.0	3.0	4.0	5.0
$\delta^*(h = 0.1)$	0.910	1.37	1.73	2.03	2.31
$\delta^*(h = 0.02)$	0.50	0.708	0.864	1.00	1.12
$P \times 10^{-7}$	6.0	7.0	8.0	9.0	10.0
$\delta^*(h = 0.1)$	2.55	2.78	2.99	3.19	3.37
$\delta^*(h = 0.02)$	1.22	1.32	1.41	1.49	1.58

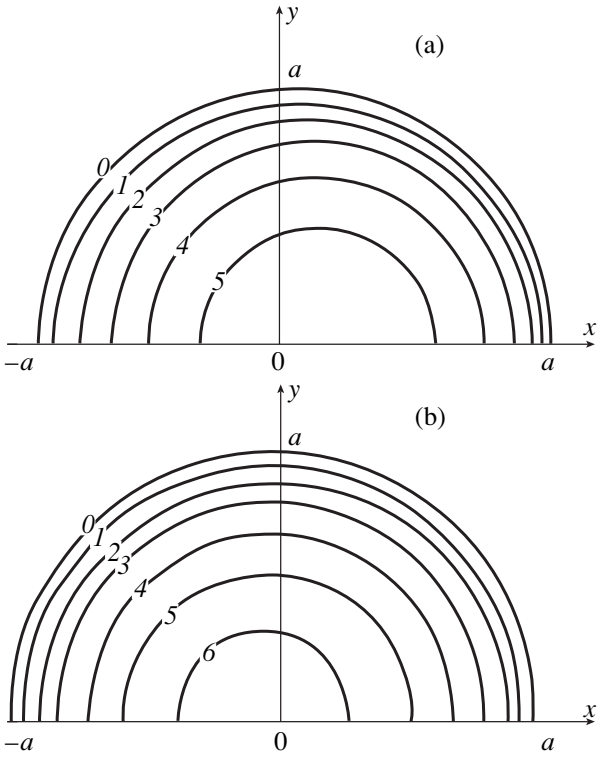

Fig. 2. Contact area and stress contours in it for (a) ν = 0.1 and (b) 0.4.

Table 2 presents the δ* values at ν = 0.3, $G = 7 \times 10^{10}$, μ = 0.9, $R_1 = R_2 = 1.0$, and indicated values of P and h. At other values μ < 1.0 and identical values of the other parameters, the results are the same.

We numerically investigated the vertical displacements of the points of the layer surface $z = h$ and the contact-area shape. These characteristics also depend strongly on the layer thickness h, the coefficient of friction μ, and the Poisson ratio ν. The dependence on the last parameter is the strongest. For Poisson ratios close to zero, layer-surface points in the vicinity of the die at $x > 0$ are less displaced in the direction of the force P than those at $x < 0$. For Poisson ratios close to 0.5, these displacements at $x > 0$ are larger than those at $x < 0$. This difference increases as the relative layer thickness $h^* = h/D$ decreases or the friction coefficient μ increases. In addition, the contact area is displaced in the direction of the force T at small ν and in the opposite direction at large ν, in contrast to the case of μ = 0. The calculations also show that, at small h^*, the layer surface bulges either at $x > 0$ (small ν) or at $x < 0$ (ν close to 0.5). This behavior is illustrated in Figs. 1 and 2.

Figure 1 shows the deformed surfaces in the vicinity of the die and under it at $P = 10^7$, $G = 7 \times 10^{10}$, μ = 0.9, $h = 0.02$, and $R_1 = R_2 = 1$. These surfaces correspond to the function $w^*(x, y) = -\dfrac{w(x, y, 0)}{\delta}$ at $|x| \le 2a$, $0 \le y \le 2a$ for (a) ν = 0.1 ($a = 3.51$) and (b) 0.4 ($a = 2.93$).

For the same parameter values, Fig. 2 shows (curve *0*) the contact-area boundary and (*1–6*) contours of the function $q^*\left(\dfrac{x}{a}, \dfrac{y}{a}\right) = \dfrac{q(x, y)\sqrt{R_2}}{\pi G\sqrt{2\delta}}$ describing the dimensionless contact stresses $q(x, y)$ at $y \ge 0$. The curves numbered by n correspond to the values $q^* = 0.1n$. Maxima of the quantity $q^*(x', y')$ in the contact area are $q^*_{\max} = q^*(0.15, 0) = 0.597$ and $q^*_{\max} = q^*(-0.1, 0) = 0.661$, respectively. The point coordinates x' are presented here with an absolute error less than or equal to $0.05a$. It is noteworthy that the point of the maximum contact stresses is displaced in the direction of the force T at ν = 0.1 and in the opposite direction at ν = 0.4, in contrast to the case of μ = 0.

REFERENCES

1. B. A. Galanov, Prikl. Mat. Mekh. **49**, 627 (1985).
2. B. A. Galanov, Dokl. Akad. Nauk SSSR **296**, 812 (1987) [Sov. Phys. Dokl. **32**, 857 (1987)].
3. L. A. Galin, *The Contact Problems in the Theory of Elasticity and Viscoelasticity* (Nauka, Moscow, 1980).
4. V. M. Aleksandrov, Prikl. Mat. Mekh. **34**, 246 (1970).
5. L. A. Galin and I. G. Goryacheva, Prikl. Mat. Mekh. **46**, 1016 (1982).
6. A. S. Kravchuk, Trenie Iznos **2**, 589 (1981).
7. A. A. Spektor, Prikl. Mat. Mekh. **51**, 76 (1987).
8. D. A. Pozharskiĭ, Dokl. Akad. Nauk **372**, 333 (2000) [Dokl. Phys. **45**, 236 (2000)].
9. D. A. Pozharskiĭ, Prikl. Mat. Mekh. **64**, 151 (2000).
10. I. I. Vorovich, V. M. Aleksandrov, and V. A. Babeshko, *Nonclassical Mixed Problems in the Theory of Elasticity* (Nauka, Moscow, 1974).
11. I. A. Lubyagin, D. A. Pozharskiĭ, and M. I. Chebakov, Prikl. Mat. Mekh. **56**, 286 (1992).
12. A. I. Lur'e, *The Theory of Elasticity* (Nauka, Moscow, 1970).

Translated by Yu. Verevochkin

Doklady Physics, Vol. 47, No. 3, 2002, pp. 241–244. Translated from Doklady Akademii Nauk, Vol. 383, No. 2, 2002, pp. 198–201.

MECHANICS

New Efficient Methods for Controlling Robots through the Internet

I. R. Belousov

Presented by Academician D.E. Okhotsimskiĭ October 18, 2001

Received October 22, 2001

The remote control of robots in the Internet medium is a new promising trend in scientific research, which has important practical importance. However, the progress in this field is restrained by limitations on the data-transmission rate intrinsic to the Internet. The principal problem is the presence of substantial arbitrary time delays in the communication channel. This fact hampers the realization of Internet control and, in the majority of cases, makes it impossible.

The author has developed several new original methods for the efficient control of robots through the Internet. The methods proposed are based on employing a virtual control medium involving a three-dimensional model of a robot with its workspace and representing the robot's current state. The use of control models for both a robot and its operation medium provides a fast response in the system being controlled to the actions of an operator, which minimizes the transmitted-data flow and promotes efficient operation even in the case of substantial delays in the communication channel. A language and a medium for the remote programming of robots through the Internet are developed. The efficiency of the methods proposed was corroborated in numerous experiments with Internet-controlled manipulation robots and mobile robots in which common-use communication channels were employed. The methods developed can be applied to a wide class of systems for the remote control of robots with delays inherent in communication channels. We also present here certain experimental data and discuss domains for possible application of the results of this study.

1. Significant progress achieved in recent years in the field of computer and Internet technologies provided a fast quantitative and qualitative rise in the application of the Internet robotics. The applications of network robotics, which became quite important in practice, are remote education and remote controlled automated production, in particular, in extremal media [1]. However, currently developed systems with robot control based on transmitting video images has certain disadvantages, such as substantial delays in the feedback channel and the control medium that is inconvenient for an operator. In addition to the considerable delays while transmitting video images, their size and quality can hamper the estimate of robot positions and distances between objects in the workspace for an operator.

To overcome these disadvantages, the author has developed new methods for improving the efficiency of controlling robots through the Internet [2–5]. These methods are based on using virtual three-dimensional models of a robot and its workspace in the online (real-time) regime. The idea of this approach consists in the fact that, instead of cumbersome video images, the operator receives a minimum set of parameters unambiguously defining the state of a robot and its operation medium (the set of generalized coordinates of the robot and of an object interacting with this robot). Then, the operation scene is visualized by methods of computer graphics (Fig. 1). This approach makes it possible not only to minimize the delays in the system response to the control actions (by minimizing the data transmitted), but also to provide a comfortable controlling medium for the operator (with the possibility of changing the direction of view, magnifying details of the scene, and using half-transparent images). Application of the computer simulation of the robot and its workspace for the Internet control provided the possibility of an efficient control even for low transmission rates (0.1–0.5 kbyte/s) in the case of employing commonly used communication channels. The corresponding graphic module is realized in the Java3D language.

To minimize the data flow between a server and a client, we developed a special exchange algorithm. Every message involves an instruction code and a set of its associated parameters (integers). For visualizing the robot and the object in their current state, it is necessary to transmit only 80 bytes. This provides a rate of renewal for the three-dimensional image at the operation scene on the order of 12 times per second for the transmission rate of 1 kbyte/s. At the same time, in the case of using video images, the scene renewal takes place with a frequency lower than 1 frame per 5 s.

Keldysh Institute of Applied Mathematics, Russian Academy of Sciences, Miusskaya pl. 4, Moscow, 125047 Russia

1028-3358/02/4703-0241$22.00

Fig. 1. Virtual medium for the robot control.

For this reason, a unique solution for efficient Internet robot control through commonly used communication channels is operation with the three-dimensional computer model of a robot and its workspace. This makes it possible to reduce time delays to an acceptable level and to provide a fast response of the system to operator actions.

2. We have developed an Rcl language (Robot-control language) for the remote programming of robots through the Internet. This language involves instructions setting motion and positions of a robot (points in its workspace) and service commands.

Motion-setting instructions enable an operator to direct the robot grip to points determined *a priori*, to displace the grip at a desired distance from a current position, to rotate it with respect to a chosen axis, etc.

Robot-position instructions make it possible to determine and to change points in the robot workspace.

Service instructions enable a user to control a grip, to calibrate a robot, and also to store on a disk and to load programs and data needed in the course of the current control session.

An important feature of the Rcl language developed for the remote programming of robots is the possibility to program operations in the on-line regime, i.e., in the current robot-control session. Moreover, it turns out to be possible to execute both individual commands and their arbitrary combinations, including those using control constructions in the Rcl language (cycles, conditions, and procedures). For example, the following fragment of the program makes it possible to determine two points in the robot workspace and to organize a displacement of the grip along the given segment:

```
Rcl > here A
Rcl > moves 100 200 300
Rcl > here B
Rcl > proc line {n} {
        global A; global B;
        for {set i 0} {$i < $n} {incr i} {
            gos A; gos B; }
        }
Rcl > line 3.
```

The use of the remote-programming medium enabled us to essentially improve the efficiency of executing repeated actions by an operator. We developed an extension of the Rcl language for programming the motion of mobile robots.

3. Currently, the methods described have no analogs among operating systems. On the basis of these methods, in the Keldysh Institute of Applied Mathematics (KIAM), Russian Academy of Sciences, systems for controlling the RM-01 manipulation robot, the CRS manipulation robot, and the Nomadic XR 4000 mobile robot through the Internet were developed (together with De Montfort University, England; Nantes Institute of Cybernetics [IRCCyN], France; and the Laboratory of Analysis of Systems [LAAS-CNRS], Toulouse, France, respectively).

The purpose of the experiments with the RM-01 robot (Fig. 2) was gripping a rod on the bifilar suspension using a virtual control medium. We performed several experimental runs when the robot established in the KIAM was controlled through the common-use net-

work from various institutions in Moscow, England, France, and South Korea [2–4].

Potentialities of the Internet-control system for the RM-01 robot were shown during the Day of the Faculty of Mechanics and Mathematics in Moscow State University (MSU). The robot was controlled by students from the MSU main building (at a distance of approximately 25 km).

The remote control of the RM-01 robot through the common-use network was successfully demonstrated at the IEEE International Conference on Robotics and Automation ICRA'2001 (Seoul, South Korea, May, 2001). The robot was controlled from the conference hall at a distance of over 10 000 km. Using the virtual controlling medium, an object was gripped in the real-time scale, although a delay in the transmission of video images reached more than 30 s.

Similar experiments were performed with the CRS manipulation robot that gripped parallelepiped-shaped objects [4]. The remote-control system for the CRS robot was demonstrated at the Exposition of digital technologies in Vandee province (Montegue, France). Access to the robot situated at a distance of 50 km from the exposition hall was realized through a conventional telephone line (34800 kbyte/s) and using a mobile phone (9 600 kbyte/ s).

Experiments with the Nomadic robot (Fig. 3) were devoted to developing a platform for mobile telecommunication conferences [5]. The robot was controlled by choosing target points on two-dimensional or three-dimensional maps of its workspace, while the navigation between the chosen positions was realized locally in the automatic regime. The robot was equipped with a set of sensors, a stereoscopic pair of TV cameras, and devices for vocal communication.

4. We have developed methods for the efficient Internet control of robots. The methods are based on using virtual three-dimensional models of a robot and its workspace in the online regime, as well as a medium for the remote programming of robots. This enabled us to overcome a principal problem of the Internet control, namely, the presence of substantial arbitrary time delays in communication channels, to provide a fast response of the system on controlling actions of an operator, and to provide a convenient and efficient control medium.

Our further investigations are focused on developing methods of reconstruction of the three-dimensional model of the robot workspace including processing mobile objects. We intend to develop various technologies for the remote Internet control of robots, which will provide efficient functioning of an operator in the case of various network-connection rates. In particular, it is assumed to analyze events and the workspace state of a robot and to transmit a small data set determining this state to an operator. We develop algorithms for gripping a complicated dynamic object (e.g., a rod at the bifilar suspension) by an Internet-controlled robot.

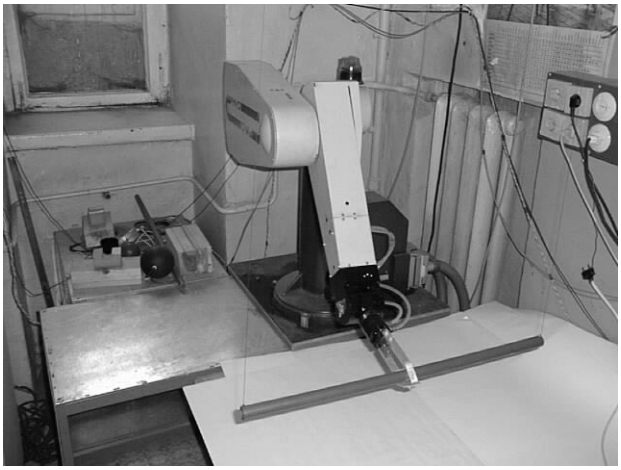

Fig. 2. RM-01 manipulation robot.

Fig. 3. Nomadic XR 4000 mobile robot.

These algorithms are based on both the application of a system of technical vision and the prediction of the object motion on the basis of an adequate dynamic model [6, 7].

Of special interest is the creation of a medium for remote education in the field of robotics and mecha-

tronics on the basis of developing systems for Internet-controlled robots. The principal features of these systems is the possibility to carry out experiments with an actual robot and actual equipment, which is of special interest for universities and other educational institutions having no such device and equipment. The methods developed make it possible to realize the joint use of expensive robotics equipment through the Internet.

ACKNOWLEDGMENTS

This work was supported by the Federal Purposeful Program "Integration of Higher Education and Fundamental Science", the Complex Program of Scientific Research of the RAN Presidium, and the RAN–CNRS Agreement.

REFERENCES

1. P. Backes, K. Tso, J. Norris, *et al.*, in *Proc. IEEE Intern. Conf. on Robotics and Automation, San Francisco, USA, 2000* (San Francisko, 2000), p. 2025.
2. G. Clapworthy, I. Belousov, A. Savenko, *et al.*, in *Confluence of Computer Vision and Computer Graphics* (Kluwer Academic Publisher, Amsterdam, 2000), pp. 215–228.
3. I. R. Belousov, in *Proc. 8th Congress on Theoretical and Applied Mechanics, Perm', Russia, 2001* (Perm', 2001), p. 91.
4. I. R. Belousov, R. Chellali, and G. Clapworthy, in *Proc. IEEE Intern. Conf. on Robotics and Automation, Seoul, Korea, 2001* (Seoul, 2001), p. 1878.
5. R. Alami, I. R. Belousov, S. Fleury, *et al.*, *Proc. IEEE Intern. Conf. on Intelligent Robots and Systems, Takamatsu, Japan, 2000* (Takamatsu, 2000).
6. I. R. Belousov, D. E. Okhotsimskiĭ, V. V. Sazonov, *et al.*, Izv. Akad. Nauk, Mekh. Tverd. Tela, No. 4, 102 (1998).
7. I. R. Belousov, D. E. Okhotsimskiĭ, V. V. Sazonov, *et al.*, Izv. Akad. Nauk, Mekh. Tverd. Tela, No. 1, 194 (2001).

Translated by V. Bukhanov

Doklady Physics, Vol. 47, No. 3, 2002, pp. 245–248. Translated from Doklady Akademii Nauk, Vol. 383, No. 2, 2002, pp. 202–205.

MECHANICS

Self-Similar Solutions to Problems on Compaction and Water Recovery of Clays while Extracting Water from Strata

A. G. Egorov and A. V. Kosterin

Presented by Academician V.P. Myasnikov August 25, 2001

Received October 26, 2001

INTRODUCTION

Infiltration of liquids in a stratum system and the deformation of surrounding rocks are known to be interrelated processes (see, i.e., [1]). In certain cases, such an interrelation is manifested especially clearly and, as a rule, is caused by the presence of insufficiently compacted clay layers contacting a header in use. While boring and exploiting a stratum, water flows in from clay layers compressed by overlying rocks. The softer the clay layer, the greater its strain and, therefore, the larger the ground shrinkage and the water yield from the stratum to the header. These effects were repeatedly observed in the practice of oil production and hydrogeology. Reiterated many-meter shrinkages were observed in the Wilmington [2] and Eckofisk [3] oil fields, in the process of the underground-water extraction in Mexico [2], etc. Balance calculations performed for the Belozerskiĭ water-bearing complex [4] can serve as one more example. These calculations showed that the water inflow into a water-bearing stratum, which had been caused by compressing slightly permeable rocks surrounding the stratum, provides the predominant contribution to the water discharge rate.

Theoretical description of the effects indicated above requires setting and solving combined problems of rock geomechanics and water infiltration in deformable strata. Some of the results of studies of this kind were described in [5–7]. However, the specific nature of the object under consideration, which is presented by a soft clay layer contacting a header, does not allow the results of these papers to be used immediately. In this paper, we propose a new formulation of the problem, which takes into account the key role of the clay layer in the process under study. Additionally, we find an analytical solution to this problem.

Research Institute of Mathematics and Mechanics, Kazan State University, ul. Universitetskaya 17, Kazan, 420008 Russia

1. STATEMENT OF THE PROBLEM

We consider a porous stratum lying on an impermeable rigid base and separated from overlying rocks by a soft clay layer.

Using the conventional infiltration equation for liquid in a layer and considering, as in [5, 6], the superposed rocks as an impermeable elastic plate, we arrive at

$$m\beta\frac{\partial p}{dt} - k\Delta p = \frac{q}{h}, \tag{1}$$

$$D\Delta^2 w = \Gamma. \tag{2}$$

Here, m, β, k, and h are the porosity, compressibility, filtration coefficient, and thickness of the stratum, respectively; q is the overflow of the liquid from the clay layer into the stratum; p is the pressure variation with respect to the initial pressure in the stratum; D is the rigidity modulus for the plate of overlying rocks; Γ is the normal load (per unit area) applied to the lower plate-base surface, i.e., to the boundary with the clay layer; and w is the plate's bending equal to the shrinkage of the clay layer. It is necessary to supplement Eqs. (1) and (2) by relations describing macroscopic rheology of the clay layer. The corresponding conditions should relate the quantities q and Γ entering into the right-hand sides of Eqs. (1) and (2) to pressure p at the base surface of the clay layer and to the layer's shrinkage w. These relations are found by solving the problem on the unidimensional consolidation of a clay layer. One of them,

$$q = \dot{w}, \tag{3}$$

is a consequence of the assumption conventional for the theory of infiltration consolidation [8]. According to this theory, the compressibility of both the liquid and the skeleton nuclei is lower than that of the skeleton by itself. The second relation significantly depends on the deformation model accepted for describing the behavior of the clay-layer porous matrix. Considering insufficiently compacted clays, we accept the ultimate rheological scheme in which the porous matrix is assumed to be force-free deformable only until its strain ϵ has

1028-3358/02/4703-0245$22.00

attained a certain value ϵ_0. The model allows for two main features of the deformation process in insufficiently compacted clays: (a) at the initial-compaction stage, the strain resistance is primarily associated with infiltrating a liquid rather than with stresses in the matrix; and (b) the secondary compaction is small compared to the initial one.

Within the framework of this scheme, solving the unidimensional problem on the consolidation of a clay layer is not difficult and yields the following macroscopic relation:

$$\dot{w} = K\frac{\epsilon_0}{w}(\Gamma - p), \quad w \le w_0 = \epsilon_0 H. \tag{4}$$

Here, K and H are the filtration coefficient and the thickness of the clay layer, respectively. The physical meaning of relation (4) is evident: the filtration flow from the layer into the stratum [the left-hand side of (4)] is determined by the current penetration depth $\frac{w}{\epsilon_0}$ and the pressure drop $(\Gamma - p)$ in the compression wave.

Eliminating Γ and q from (1)–(4), we arrive at the system of two nonlinear parabolic equations with respect to the pressure p and the shrinkage w. After introducing the dimensionless coordinates (p_0 is a characteristic pressure)

$$w \longrightarrow \frac{w}{w_0}, \quad p \longrightarrow \frac{p}{p_0}, \quad t \longrightarrow \frac{t}{t_0}, \quad x \longrightarrow \frac{x}{x_0};$$

$$t_0 = \frac{w_0^2}{p_0 K \epsilon_0}, \quad x_0^2 = \frac{khw_0}{K\epsilon_0},$$

the system can be written out in the form

$$b\varepsilon\frac{\partial p}{\partial t} - \frac{\partial w}{\partial t} = \Delta p, \tag{5}$$

$$p + w\frac{\partial w}{\partial t} = \varepsilon\Delta^2 w, \quad w \le 1. \tag{6}$$

The dimensionless parameters ε and $b\varepsilon$ are determined by the relationships

$$b\varepsilon = \frac{m\beta h p_0}{w_0}, \quad \varepsilon = \frac{Dw_0}{p_0}\left(\frac{K}{khH}\right)^2.$$

The typical values of these parameters are

$$k \sim 10^{-9}\frac{\text{m}^2}{\text{Pa s}}, \quad K \sim 10^{-13}\frac{\text{m}^2}{\text{Pa s}}, \quad h \sim H \sim 10 \text{ m},$$

$$m \sim 1, \quad \epsilon_0 \sim 10^{-1}, \quad p_0 \sim 10^6 \text{ Pa}, \quad D \sim 10^{15} \text{ Pa m}^2.$$

In this case,

$$t_0 \sim 3 \text{ years}, \; x_0 \sim 1 \text{ km}, \; \varepsilon \sim 10^{-3}, \text{ and } b \sim 1.$$

The value of D corresponds to the stratum depth of occurrence and to the Young's modulus on the order of 100 m and of 10^{10} Pa, respectively.

2. ASYMPTOTIC METHOD FOR SOLVING THE PROBLEM

The smallness of the quantity ε implies that studying the asymptotic behavior of solutions to Eqs. (5) and (6) as $\varepsilon \longrightarrow 0$ is the main task to be considered. Indeed, this is the asymptotic solution that describes the process for long intervals (months or years) and, because of this, is of great practical interest. On the other hand, the method proposed is applicable only in this asymptotic region. As we show below, for time intervals on the order of or shorter than a day (i.e., outside the asymptotic region), the size of the disturbed-pressure region in a stratum is smaller than its depth of occurrence. Because of this, the treatment of superposed rocks as an elastic plate becomes inadequate.

It is natural to take the solution to Eqs. (5) and (6) in the case of $\varepsilon = 0$ as a principal term of the corresponding asymptotic solution. From the physical standpoint, the condition $\varepsilon = 0$ implies the following assumptions: (i) the compressibility of the stratum is negligible compared to that of the clay layer and (ii) the rock pressure is constant [1]. In the case of $\varepsilon = 0$, Eqs. (5) and (6) are reduced to a nonlinear steady-state equation with respect to the auxiliary function

$$\mathcal{P}(x, t) = -\int_0^t p(x, t)dt. \tag{7}$$

With regard to the equality

$$p = -\dot{\mathcal{P}} \text{ with } w = \min(1, \sqrt{2\mathcal{P}}), \tag{8}$$

which follows from (6) and (7), we write out the equation mentioned above in the form

$$\min(1, \sqrt{2\mathcal{P}}) - \Delta\mathcal{P} = 0. \tag{9}$$

The boundary conditions for $\mathcal{P}$ are related to those for pressure. The latter are specified by the exploitation regime for the stratum and determine the parametric dependence of the desired function $\mathcal{P}$ on time.

In many cases, the solution to Eq. (9), with p and w subsequently found from (8), describes both the stratum pressure and the clay-layer shrinkage with an accuracy sufficient for practical applications. As a rule, an improvement of the description is needed near the boundaries (boreholes, isobars), where the corresponding shrinkage field, in general, does not satisfy natural boundary conditions. To do this, a boundary layer approximation should be constructed and then sewed with the solution to Eq. (9).

In order to illustrate and estimate capabilities of the asymptotic method proposed, we now consider a stratum being exploited by a gallery of boreholes that may operate either under constant-pressure conditions or constant-yield conditions.

3. THE PRINCIPAL TERM OF THE ASYMPTOTIC SOLUTION

In the cases under consideration, the problem becomes unidimensional and Eq. (9) should be solved in the region $x > 0$ under the boundary condition $\mathcal{P}(\infty) = 0$. The boundary condition at the borehole gallery has a form of either $\mathcal{P}(0) = t$ (constant pressure) or $\mathcal{P}'(0) = -t$ (constant yield). In both the cases, the disturbance propagation velocity is finite, with $\mathcal{P}(x, t) \equiv 0$ for $x > x_*(t)$, and there are two time ranges characteristic for the process. For $0 < t < t_*$, the shrinkage is everywhere smaller than the ultimate value, and the function $\mathcal{P}$ is given by the formula

$$t \le t_*, \quad x < x_*(t): \mathcal{P} = \frac{(x - x_*)^4}{72}. \qquad (10)$$

In the two regimes under consideration, respectively, $t_* = \frac{1}{2}$, with $x_*(t) = (72t)^{1/4}$, and $t_* = \sqrt{\frac{2}{3}}$, with $x_*(t) = (18t)^{1/3}$. At the second stage of the process, an ultimate-shrinkage region $0 < x < x^*(t)$ appears near the gallery and then begins growing. For the two regimes, $x^*(t) = \sqrt{2t - \frac{1}{3}} - \sqrt{\frac{2}{3}}$ and $x^*(t) = t - \sqrt{\frac{2}{3}}$, respectively. In the region mentioned above, the function $\mathcal{P}$ is given by formulas

$$t \ge t^*, x < x^*(t): \mathcal{P} = t + \frac{x(x - x^*)}{2} - \sqrt{\frac{2}{3}}x$$

(constant pressure),

$$t \ge t^*, x < x^*(t): \mathcal{P} = \frac{(t - x)^2}{2} - \frac{1}{6}$$

(constant yield).

In the region $x^*(t) < x < x_*(t)$, the function $\mathcal{P}$ is given, as before, by formula (10), where $x_*(t) = x^*(t) + \sqrt{6}$.

The most important characteristics of the solutions presented above are listed in the table.

In order to estimate the range of applicability of the asymptotic method under consideration, we compared orders of the terms omitted in Eqs. (5), (6) and of the basic terms entering into solution (10). Simple calculations showed that the ratio of these terms for the two regimes are on the order of $\varepsilon t^{-1/2}$ and εt^{-1}, respectively. Therefore, the lower bound for the range of applicability of the asymptotic method is on the order of ε^2 (minutes) and of ε (days), respectively. It is worth noting that in such time intervals the shrinkage-crater size is only on the order of $x_0\varepsilon^{1/2}$ (about 30 m) and of $x_0\varepsilon^{1/3}$ (about 100 m), respectively (see table). As a rule, these values do not exceed the stratum depth of occurrence.

4. THE BOUNDARY LAYER CORRECTION

It is evident that at the first stage of the process the principal term of the asymptotic solution found does not satisfy the natural symmetry conditions

$$x = 0: \quad \frac{\partial w}{\partial x} = \frac{\partial^3 w}{\partial x^3} = 0.$$

This discrepancy is explained by the presence of a boundary layer with the thickness on the order of $\varepsilon^{1/4}$ near the point $x = 0$. Introducing the boundary layer coordinate $y = x\varepsilon^{-1/4}$, we seek the boundary layer corrections to the principal term ($w_0 = \sqrt{2\mathcal{P}}$, and $p_0 = -\dot{\mathcal{P}}$) of the asymptotic solution in the form

$$w = w_0 + \varepsilon^{1/4}w_1(t, y) + \ldots, \; p = p_0 + \varepsilon^{3/4}p_1(t, y) + \ldots. \qquad (11)$$

Basic characteristics of processes when exploiting strata with the help of a borehole gallery

Exploitation regime	Time interval	Pressure $p(0, t)$	Yield $-p'(0, t)$	Shrinkage crater $x_*(t)$	Maximum shrinkage $w(0, t)$
Constant pressure	$t < \frac{1}{2}$	–1	$\left(\frac{8t}{9}\right)^{-1/4}$	$(72t)^{1/4}$	$\sqrt{2t}$
	$t > \frac{1}{2}$	–1	$\left(2t - \frac{1}{3}\right)^{-1/2}$	$\sqrt{2t - \frac{1}{3}} + 2\sqrt{\frac{2}{3}}$	1
Constant yield	$t < \sqrt{\frac{2}{3}}$	$-\left(\frac{2t}{3}\right)^{-1/3}$	1	$(18t)^{1/3}$	$\left(\frac{3}{2}\right)^{1/3} t^{2/3}$
	$t > \sqrt{\frac{2}{3}}$	$-t$	1	$t + 2\sqrt{\frac{2}{3}}$	1

As a result, we find that the function w_1 satisfies the linear equation

$$\frac{\partial}{\partial t}(w_0(0, t)w_1) - \frac{\partial^4 w_1}{\partial y^4} = 0$$

under the following boundary and initial conditions:

$$\left.\frac{\partial w_1}{\partial y}\right|_{y=0} = \left.\frac{\partial w_0}{\partial x}\right|_{x=0}, \quad \left.\frac{\partial^3 w_1}{\partial y^3}\right|_{y=0} = 0,$$
$$w_1|_{t=0} = 0, \quad w_1|_{y=\infty} = 0.$$

Thus, the problem formulated above has the self-similar solutions $w_1 = t^{3/8}W(yt^{-1/8})$ and $w_1 = t^{5/12}W(yt^{-1/12})$ in the two regimes, respectively. The solution to the corresponding ordinary differential equations with respect to W can be found in an explicit form. We here write out only corrections to the maximum shrinkage $w(0, t)$. For the two regimes, they are equal to $-0.5204\varepsilon^{1/4}t^{3/8}$ and $-0.4786\varepsilon^{1/4}t^{5/12}$, respectively. The corrections to pressure and the yields are significantly smaller than those presented above. According to (11), they are on the order of $\varepsilon^{3/4}$ and $\varepsilon^{1/2}$, respectively. Therefore, for typical values of the problem parameters, these corrections can be ignored in contrast to the correction to the shrinkage.

ACKNOWLEDGMENTS

This work was supported by the Russian Foundation for Basic Research, project no. 99-01-00466.

REFERENCES

1. V. N. Nikolaevskiĭ, *Mechanics of Saturated and Cracked Media* (Nedra, Moscow, 1984).
2. V. N. Shchelkachev, *Foundations and Applications of Unsteady Filtering Theory*, Part 2 (Neft' i Gaz, Moscow, 1995).
3. V. Mori, in *Mecanique des roches appliquee aux problemes d'exploration et de production petroliers* (Boussens, 1993; Mir, Moscow, 1994).
4. V. A. Mironenko, in *Proceedings of International Symposium on Engineering and Geological Properties of Clay Rocks and Processes in Them, Moscow, Russia, 1971* (Mosk. Gos. Univ., Moscow, 1972), p. 97.
5. V. N. Nikolaevskiĭ, Prikl. Mat. Teor. Fiz., No. 4, 35 (1968).
6. E. F. Afanas'ev and V. N. Nikolaevskiĭ, Prikl. Mat. Teor. Fiz., No. 5, 113 (1969).
7. V. M. Entov and T. A. Malakhova, Izv. Akad. Nauk SSSR, Mekh. Tverd. Tela, No. 61, 53 (1974).
8. A. G. Egorov, A. V. Kosterin, and É. V. Skvortsov, *Consolidation and Acoustic Waves in Saturated Porous Media* (Izd. Kazan. Univ., Kazan, 1990).

Translated by V. Chechin

Doklady Physics, Vol. 47, No. 3, 2002, pp. 249–253. Translated from Doklady Akademii Nauk, Vol. 383, No. 2, 2002, pp. 206–210.

MECHANICS

Structure of Isobaric Flows in a Gas and in an Ideal Incompressible Fluid

V. E. Shemarulin

Presented by Academician Yu.A. Trutnev April 9, 2001

Received June 4, 2001

Gas or fluid flows in which pressure p is identically constant ($p \equiv \text{const}$) are referred to as isobaric (inertial) flows [1].

In this paper, we study the structural characteristics of isobaric flows in a gas and an ideal incompressible fluid (below, for brevity, isobaric flows). Equations describing isobaric flows are completely integrable. For the first time, formulas for the general solution to these equations were derived in [2, 3] (see also [4], where a more general set of equations was integrated). Chronologically, the first but less successful attempt to study the integrability of equations for isobaric flows was presented in [5]. The general solution found in [2, 3] was written in an implicit form as a set of functional equations for the components of the velocity vector, which involve a certain number of arbitrary functions. In this connection, the problem arises to present a simpler and more constructive description of the entire variety of flows being determined by implicit formulas concerning the general solution. This problem is partially solved in the present paper. Namely, we propose here an explicit geometrical description of the structure of three-dimensional steady-state and two-dimensional unsteady-state flows. The case of two-dimensional steady-state flows is rather trivial and is not considered here. Indeed, it is easy to show that all such isobaric flows (even in the assumption that they are determined only locally) are of a shear type in any connected domain. This implies that the flow paths are parallel. The problem concerning the explicit description of three-dimensional unsteady-state flows is still open.

1. LOCAL CLASSIFICATION OF ISOBARIC FLOWS ACCORDING TO THEIR RANK [2, 3]

In Euler variables, the isobaric flows are described by the following set of equations for the velocity field $\mathbf{u} = \mathbf{u}(\mathbf{x}, t)$ [1]:

$$\begin{aligned} \mathbf{u}_t + (\mathbf{u} \cdot \nabla)\mathbf{u} &= 0, \\ \operatorname{div}\mathbf{u} &= 0. \end{aligned} \tag{1}$$

Here, $\mathbf{u} = (u, v, w)$, $\mathbf{x} = (x, y, z)$ [for two-dimensional flows, we have $\mathbf{u} = (u, v)$ and $\mathbf{x} = (x, y)$]. Let $\boldsymbol{\xi} = (\xi, \eta, \zeta)$ be the Lagrangian coordinates of gas (fluid) particles: $\boldsymbol{\xi} = \mathbf{x}(0)$. From the first equation in (1), it follows that $\mathbf{u} = \mathbf{u}(\boldsymbol{\xi})$, and the condition of divergence-free flow implies that the function $\mathbf{u}(\boldsymbol{\xi})$ satisfies a set of three equations obtained by putting to zero the invariants of the Jacobian matrix $J = \dfrac{\partial \mathbf{u}}{\partial \boldsymbol{\xi}}$ [1–3]. In particular, we have

$$\det J = \begin{vmatrix} u_\xi & u_\eta & u_\zeta \\ v_\xi & v_\eta & v_\zeta \\ w_\xi & w_\eta & w_\zeta \end{vmatrix} = 0. \tag{2}$$

We restrict our analysis to the consideration of the local structure of isobaric flows, assuming that everywhere in the domain under study the flow is smooth and the rank $\operatorname{rk} J$ of the Jacobian matrix has a constant value. Based on equation (2), we can classify the isobaric flows according to their rank:

(i) $\operatorname{rk} J \equiv 0$. In this case, $\mathbf{u} = \text{const}$ and the flow is uniform.

(ii) $\operatorname{rk} J \equiv 1$. In this case, two components of the velocity vector are functions of the third component. The flow is referred to as a simple wave [2] or a flow of rank 1.

(iii) $\operatorname{rk} J \equiv 2$. For such a flow, one component of the velocity vector is a function of two other components. The flow is referred to as a double wave [2] or as a flow of rank 2.

2. BASIC CLASSES OF THREE-DIMENSIONAL ISOBARIC STEADY-STATE FLOWS

In our terminology, basic classes are three classes composed of the following isobaric flows:

All-Russia Research Institute of Experimental Physics, pr. Mira 17, Sarov, Nizhni Novgorod oblast, 607190 Russia

1028-3358/02/4703-0249$22.00

(I) shear flows, i.e., flows occurring in parallel planes and along parallel straight lines in each plane;

(II) conic (conic-type) flows, i.e., flows occurring along families of half-planes tangential to arbitrary convex conic surfaces, and, in each half-plane, moving along straight lines parallel to the generatrix of the conic surface belonging to this half-plane;

(III) tangential (tangential-type) flows, i.e., flows occurring along families of half-planes tangential to the so-called tangential surfaces (the surfaces formed by tangents to arbitrary three-dimensional curves). These surfaces obey certain conditions of convexity (ensuring the absence of intersections between the tangential half-planes). In each half-plane, the flows move along straight lines parallel to the generatrix of the tangential surface belonging to this half-plane.

In the general case, for all aforementioned flows, gas (fluid) flows with its own velocity along each straight line (streamline).

The shear flows are well known [6]. In the steady-state case, they are specified by the following explicit formulas in the coordinate system with the *Oz*-axis orthogonal to the flow planes

$$\begin{gathered} u = -\beta\varphi(\alpha x + \beta y, z), \\ v = \alpha\varphi(\alpha x + \beta y, z), \\ w = 0, \end{gathered} \qquad (3)$$

$$\alpha = \alpha(z), \quad \beta = \beta(z), \quad \alpha^2(z) + \beta^2(z) \equiv 1.$$

Here, α and φ can be arbitrary functions. In the case of vector fields $\mathbf{u}$ of form (3), equations (1) for the steady-state flows,

$$(\mathbf{u}\cdot\nabla)\mathbf{u} = 0, \qquad (4)$$

$$\operatorname{div}\mathbf{u} = 0, \qquad (5)$$

are satisfied in a trivial way.

We now describe in more detail the structure of conic-type isobaric flows. Let K be an arbitrary convex conic surface in space $\mathbf{R}^3(x, y, z)$ with the vertex O and a directing curve γ, $\mathbf{r} = \mathbf{r}(t)$ be the vectorial parametric equation for γ, $\boldsymbol{\tau}(t) = \dfrac{d\mathbf{r}(t)}{dt}$ be a vector tangent to γ, π_t be a plane tangent to the surface K at the point $\mathbf{r}(t)$, $l_t = \pi_t \cap K$ be the generatrix of the surface K lying in π_t, and π_t^+ and π_t^- be half-planes for which the straight line l_t divides the π_t plane and which contain vectors $\boldsymbol{\tau}(t)$ and $-\boldsymbol{\tau}(t)$, respectively. A conic flow of the general form related to the surface K (and determined by it or, more precisely, by families $\{\pi_t^+\}$ and $\{\pi_t^-\}$) is constructed in the following manner. We choose one from two families of tangent half-planes. For definiteness, let it be $\{\pi_t^+\}$. In each half-plane π_t^+, we define a vector field $\mathbf{u}$ parallel to the generatrix $l_t \subset \pi_t^+$ and depending on a single parameter d, which is the distance between the application point of the vector $\mathbf{u}$ and the straight line l_t. Imposing the requirement that $\mathbf{u}$ smoothly depends on t and d, we obtain a smooth vector field $\mathbf{u} = \mathbf{u}(x, y, z)$ defined in domain $G = \bigcup_t \pi_t^+$. The convexity of curve γ ensures the absence of intersections of the half-planes from the chosen family and, hence, the uniqueness of the field $\mathbf{u}$ in G. For the field $\mathbf{u}$ constructed in such a manner, Eq. (4) is satisfied automatically and the validity of equation (5) is verified by direct calculations. This implies that such an arbitrary field $\mathbf{u}$ is the velocity field of the eventual steady-state isobaric flow. We refer to each pair $(\mathbf{u}|_{G'}, G')$, where G' is a subdomain of G, as a conic-type flow. In the most general situation for domain G', we can admit flows with discontinuities along the lined surfaces consisting of paths (streamlines), as well as to start and terminate the paths, thereby allowing the existence of surface sources and sinks.

In a similar manner, we can construct isobaric flows of the tangential type determined by the tangential surface T with the directrix three-dimensional curve γ. In this case, generatrices l_t of the surface T are tangents to γ, whereas the tangent half-planes π_t^+ and π_t^- of the surface T coincide with the half-planes into which l_t divides the osculating plane π_t of the curve γ. Half-planes π_t^+ and π_t^- differ from each other, because one of them contains vector $\mathbf{v}(t)$ of the main normal to the directrix curve γ and the other half-plane contains the opposite vector $-\mathbf{v}(t)$. Similar to the case of conic flows, t is the parameter of motion along the curve γ.

3. LOCAL STRUCTURE OF THREE-DIMENSIONAL ISOBARIC STEADY-STATE SIMPLE WAVES

Without the loss of generality, we can write for the simple wave

$$u = \varphi(w), \quad v = f(w). \qquad (6)$$

Here, $w \neq 0$ and $\nabla w \neq 0$ everywhere within the range of the definition of the flow. To analyze the structure of steady-state simple waves, we can use the general expression implicitly describing the class of three-dimensional isobaric flows of rank 1 [2, 6]. If relationships (6) are met, then this expression has the form

$$\xi = \varphi'(w)\zeta + \lambda(w, \eta - f'(w)\zeta), \qquad (7)$$

where $\varphi(w)$, $f(w)$, and $\lambda(\alpha, \beta)$ are arbitrary smooth functions. The passage from representation (7) to the representation in Eulerian variables is performed using the equations

$$x = \xi + ut, \quad y = \eta + vt, \quad z = \zeta + wt. \qquad (8)$$

On the other hand, in such an analysis, we can use relationships (6) directly substituting them into equations (4)

and (5) and then find an equivalent (in the case under study) system of two scalar quasilinear equations

$$\varphi(w)w_x + f(w)w_y + ww_z = 0, \quad (9)$$

$$\varphi'(w)w_x + f'(w)w_y + w_z = 0. \quad (10)$$

These equations describe simple waves in terms of the velocity-vector third component.

Let

$$\pi_w = \{(x, y, z) \in \mathbf{R}^3: w(x, y, z) = w = \text{const}\}$$

be the level surface of the velocity field **u**.

Proposition 1. *For isobaric three-dimensional steady-state simple waves* (6)*, surfaces* π_w *are cylindrical* (*in particular, they can be planar and even degenerate to straight lines). Generatrices of these surfaces are streamlines of the field* **u**, *which are determined by equations* (8) [*characteristics of equation* (9)]. *The range of definition for a simple wave can be divided into subdomains such that for each of them one of the following properties takes place.*

(A) *Everywhere, characteristics of equations* (9) *and* (10) *coincide. In this case, these characteristics are parallel and the simple wave corresponds to the flow along parallel straight lines.*

(B) *Everywhere, characteristics of equations* (9) *and* (10) *are different; in this case, all surfaces* π_w *are planar* (*and, hence, form a one-parameter family*); *each surface* π_w *is a combination* (*family*) *of streamlines passing through various points of a certain characteristic of equation* (10). *Below, the simple wave is referred to as the flow in a one-parameter family of planes* $\{\pi_w\}$.

Based on Proposition 1 and using the well-known classification of one-parameter families of planes [7, 8], we can prove the following theorem.

Theorem 1. *An arbitrary isobaric three-dimensional steady-state simple wave is locally a flow of one of the following four types: flows along parallel straight lines* (*special shear motion*) *with different* (*in the general case*) *velocity values for each streamline, as well as shear, conic, and tangential flows. For shear flows, the flow is constant in each plane* π_p *of the corresponding parallel bundle, whereas for conic and tangential flows the flow is constant in each tangent half-plane* $\pi_t^{\pm}$ *corresponding to the conic or tangential surface. In the general case, the velocity in each plane* π_p *and the absolute value of the velocity in each half-plane* $\pi_t^{\pm}$ *are different.*

4. LOCAL STRUCTURE OF ISOBARIC THREE-DIMENSIONAL STEADY-STATE DOUBLE WAVES

The formulas implicitly specifying the general solution of rank 2 for equations that describe isobaric flows in the Eulerian coordinates have the following form [2, 3]:

$$\begin{gathered} G(u_1, u_2, u_3) = 0, \quad \nabla G \neq \mathbf{0}, \\ \sum_{i=1}^{3} (x_i - tu_i)\frac{\partial G}{\partial u_i} = H(u_1, u_2, u_3), \\ \sum_{i,j=1}^{3} (x_i - tu_i)(x_j - tu_j)\frac{\partial^2 G}{\partial u_i \partial u_j} \\ -2\sum_{i=1}^{3} (x_i - tu_i)\frac{\partial H}{\partial u_i} = \Sigma(u_1, u_2, u_3), \end{gathered} \quad (11)$$

where $\mathbf{u} = (u_1, u_2, u_3)$, $\mathbf{x} = (x_1, x_2, x_3)$, $\mathbf{u} = \mathbf{u}(\mathbf{x}, t)$; G, H, and Σ are arbitrary smooth functions for which set of equations (11) is solvable with respect to u_1, u_2, and u_3. Without the loss of generality, we can assume that everywhere in the definition range of the solution **u** under study the following conditions are met

$$u_3 \neq 0, \quad \frac{\partial G}{\partial u_3} \neq 0.$$

For the steady-state solutions $\mathbf{u} = \mathbf{u}(\mathbf{x})$, set (11) becomes "split" with respect to t. As a result of such a splitting, we obtain a system of functional equations implicitly describing isobaric three-dimensional steady-state double waves

$$\begin{gathered} G(u_1, u_2, u_3) = 0, \quad \nabla G \neq \mathbf{0}, \\ \sum_{i=1}^{3} x_i\frac{\partial G}{\partial u_i} = H(u_1, u_2, u_3), \\ \sum_{i=1}^{3} u_i\frac{\partial G}{\partial u_i} = 0, \\ \sum_{i,j=1}^{3} x_i x_j\frac{\partial^2 G}{\partial u_i \partial u_j} - 2\sum_{i=1}^{3} x_i\frac{\partial H}{\partial u_i} = \Sigma(u_1, u_2, u_3), \\ \sum_{i,j=1}^{3} x_i u_j\frac{\partial^2 G}{\partial u_i \partial u_j} - \sum_{i=1}^{3} u_i\frac{\partial H}{\partial u_i} = 0, \\ \sum_{i,j=1}^{3} u_i u_j\frac{\partial^2 G}{\partial u_i \partial u_j} = 0. \end{gathered} \quad (12)$$

The following set of equations plays an important role in the analysis of the structure characteristic of the double waves

$$\lambda_2 = f(\lambda_1),$$

$$-f'(\lambda_1)(x_1 - \lambda_1 x_3) + (x_2 - \lambda_2 x_3) = h(\lambda_1, \lambda_2),$$

$$-f''(\lambda_1)(x_1-\lambda_1 x_3)^2-2(x_1-\lambda_1 x_3)\frac{\partial h}{\partial \lambda_1} \qquad (13)$$

$$-2(x_2-\lambda_2 x_3)\frac{\partial h}{\partial \lambda_2} = \Sigma_1(u_1, u_2, u_3),$$

$$\lambda_1 = \frac{u_1}{u_3}, \quad \lambda_2 = \frac{u_2}{u_3},$$

where f, h, and Σ_1 can be arbitrary smooth functions for which Eq. (13) is solvable with respect to u_1, u_2, and u_3. All such functions f, h, and Σ_1 are referred to as admissible.

Theorem 2. *Arbitrary set* (12) *as a set of equations with respect to variables u_1, u_2, u_3 is equivalent to a certain set of form* (13). *The entire variety of isobaric three-dimensional steady-state double waves is described by solutions of rank* 2 *to sets* (13) *with various admissible functions f, h, and Σ_1.*

From Theorem 2, it follows that level surfaces π_λ of the vector function $\boldsymbol{\lambda} = (\lambda_1, \lambda_2)$ play the main role in the local classification of isobaric steady-state double waves.

Proposition 2. *For any isobaric three-dimensional steady-state flow of rank* 2 *in a domain, where $u_3 \neq 0$, the surface π_λ is a part of the plane π_λ^* determined by first two equations of set* (13). *If a certain streamline l of the velocity field* **u** *has a common point with a certain surface π_{λ_0}, then $l \subset \pi_{\lambda_0}$. All streamlines* (*even if they are defined only locally*) *lying in any fixed surface π_{λ_0} $\boldsymbol{\lambda}_0 = (\lambda_1^0, \lambda_2^0)$ are parallel, and the vector $\boldsymbol{\lambda}_0^* = (\lambda_1^0, \lambda_2^0, 1)$ plays the role of a directrix.*

Theorem 3. *If in the set of equations* (13), *function $f \equiv f(\lambda_1)$ is linear, then an isobaric three-dimensional steady-state flow determined by this set is of the shear type. In the case of nonlinear function f* [*it is assumed that $f''(\lambda_1) \neq 0$ everywhere within the definition range of the solution*], *the one-parameter family of planes π_λ^** (*see formulation of Proposition* 2) *containing surfaces π_λ has an envelope which is either a conic or tangential surface. Hence, in this case, the isobaric flow determined by the set of equations* (13) *is a flow of either the conic or tangential type.*

The following classification theorem is a consequence of Theorems 1–3.

Theorem 4. *An arbitrary isobaric three-dimensional steady-state flow is a combination of domains for shear flows, conic flows, and tangential flows.*

5. LOCAL STRUCTURE OF ISOBARIC TWO-DIMENSIONAL UNSTEADY-STATE FLOWS

We now put in correspondence an unsteady-state vector field $\mathbf{u} = \mathbf{u}(x, y, t)$ in $\mathbf{R}^2(x, y)$ to the steady-state vector field $\mathbf{u}_1 = \mathbf{u}_1(x, y, t) = \mathbf{u} + \mathbf{k}$, where $\mathbf{k}$ is the unit vector of the time axis Ot in space $\mathbf{R}^3(x, y, t)$. The field $\mathbf{u}$ satisfies the set of equations (1) if and only if the field $\mathbf{u}_1$ satisfies equations (4) and (5), where

$$\nabla = \mathbf{i}\frac{\partial}{\partial x} + \mathbf{j}\frac{\partial}{\partial y} + \mathbf{k}\frac{\partial}{\partial t}, \quad \mathrm{div}\mathbf{u} = u_x + v_y + w_t.$$

By virtue of this fact, a new theorem immediately follows from Theorem 4.

Theorem 5. *An arbitrary two-dimensional unsteady-state isobaric flow considered as a steady-state flow in $\mathbf{R}^3(x, y, t)$ is a combination of domains for shear, conic, and tangential flows of rank* 1, *for which the third component w* (*along the Ot-axis*) *of the velocity vector $\mathbf{u}_1 = (u, v, w)$ is identically equal to unity ($w \equiv 1$). In an arbitrary given streamline of the field $\mathbf{u}_1$, both components, u and v, are uniquely determined from the condition $w \equiv 1$. The case of "flow" in $\mathbf{R}^3(x, y, t)$ along parallel straight lines is excluded, as it corresponds to the constant flow in $\mathbf{R}^2(x, y)$.*

6. EXAMPLES

Theorems 4 and 5 yield a constructive method for determining all three-dimensional steady-state and two-dimensional unsteady-state isobaric flows. Below, we present two examples of isobaric flows constructed according to this method.

Example 1. Let K be a conic surface specified by the equation $d \equiv x^2 + y^2 - r^2 z^2 = 0$, $r > 0$, $G = \{(x, y, z): d > 0\}$. As the directrix of surface K, we take circle $\gamma = \{(x, y, 1): x^2 + y^2 = r^2\}$. If the point $P = (x, y, z) \in G$, then half-planes $\pi_P^\pm$ tangent to K and passing through P contact γ at points $\xi^\pm = r\dfrac{rxz \mp y\sqrt{d}}{x^2 + y^2}$, $\eta^\pm = r\dfrac{ryz \pm x\sqrt{d}}{x^2 + y^2}$. Consequently, vector fields $\mathbf{u}^\pm = (\xi^\pm, \eta^\pm, 1)$ are velocity fields for two conic axisymmetric flows of rank 1, which are defined in G and are associated with K.

Example 2. Flows with singularities. Let K be a conic surface specified by the equation $d \equiv z^2 - 4xy = 0$. As the directrix γ of the surface K, we take the ellipse obtained by intersecting K by the plane $x + y = 1$. If $P = (x, y, z)$ is a point belonging to the outer part of the conic surface K (i.e., to the domain $d > 0$), then coordinates $\xi^\pm$, $\eta^\pm$, $\zeta^\pm$ of points contacting the curve γ for the half-planes $\pi^\pm$ passing through P satisfy the following relationships

$$\xi^\pm = \zeta^\pm\frac{z \mp \sqrt{d}}{4y}, \quad \eta^\pm = \zeta^\pm\frac{z \pm \sqrt{d}}{4x}, \quad \xi^\pm + \eta^\pm = 1.$$

Hence, the formulas

$$u^{\pm} = \frac{z \mp \sqrt{d}}{4yd}, \quad v^{\pm} = \frac{z \pm \sqrt{d}}{4xd}, \quad w^{\pm} = d^{-1} \qquad (14)$$

specify velocity fields for two conic-type flows of rank 2 associated with K. Domain $G = \{(x, y, z): d > 0, xy \neq 0\}$, which is outer with respect to K, is a common part of the definition range for these flows. We assume that

$$\pi_1 = \{(x, y, z): y = 0, z < 0\},$$
$$\pi_2 = \{(x, y, z): y = 0, z > 0\},$$

where π_1^d and π_2^d are the half-planes supplementary to π_1 and π_2, respectively. The first flow [upper signs in (14)] is extended by continuity to π_1^d and π_2^d (excluding the Oz-axis), whereas at π_1 and π_2 it has second-order discontinuities. The second flow [lower signs in (14)] is extended by continuity to π_1 and π_2 (excluding the Oz-axis), whereas it has the second-order discontinuities at π_1^d and π_2^d.

Note 1. It can be shown that the steady-state axisymmetric isobaric flows described in [3, 9, 10] are conic-type flows of rank 2 (in the general case) in $\mathbf{R}^3(x, y, z)$, whereas the two-dimensional (planar) unsteady-state isobaric flow described in [2] is the axisymmetric conic-type flow of rank 1 in $\mathbf{R}^3(x, y, t)$, which is obtained from the flow corresponding to the velocity field $\mathbf{u}^+$ from the Example 1, if we put in it $r = 1$ and $z = t - 1$. Hence, the cone K_1 characteristic of the flow described in [2] is obtained from the cone K of Example 1 (at $r = 1$) by shifting this cone upward by 1 along the z axis.

Note 2. Using the constructions suggested in the present paper, it is possible to construct flows of ideal incompressible fluid even with nonzero pressure gradient as a superposition of isobaric flows. By a method similar to that under discussion here, it is also possible to construct unsteady-state three-dimensional isobaric flows. In this case, it is necessary to consider single-parameter families $\{\mathbf{R}^3_\lambda: \lambda \in \mathbf{R}^1\}$ of hyperplanes in $\mathbf{R}^4(x, y, z, t)$.

REFERENCES

1. L. V. Ovsyannikov, *Lectures on Gas-Dynamics Foundations* (Nauka, Moscow, 1981).
2. L. V. Ovsyannikov, Differ. Uravn. Ikh Primen. **30**, 1792 (1994).
3. Yu. A. Bondarenko, Voprosy Atomnoĭ Nauki i Tekhniki, Ser. Mat. Simulation of Physical Processes, No. 3, 41 (1994).
4. A. P. Chupakhin, Dokl. Akad. Nauk **352**, 624 (1997) [Phys. Dokl. **42**, 101 (1997)].
5. A. S. Zil'bergleĭt, Dokl. Akad. Nauk **328**, 564 (1993) [Phys. Dokl. **38**, 61 (1993)].
6. V. V. Aleksandrov and Yu. D. Shmyglevskiĭ, Dokl. Akad. Nauk SSSR **274**, 280 (1984) [Sov. Phys. Dokl. **29**, 22 (1984)].
7. A. V. Pogorelov, *Differential Geometry* (Nauka, Moscow, 1969).
8. M. Ya. Vygodskiĭ, *Differential Geometry* (Gostekhteorizdat, Moscow, 1949).
9. Yu. D. Shmyglevskiĭ, Zh. Vych. Mat. Mat. Fiz. **30**, 1833 (1990).
10. Yu. D. Shmyglevskiĭ, *Analytical Study of Gas and Fluid Dynamics* (Editorial URSS, Moscow, 1999).

Translated by K. Kugel'

Doklady Physics, Vol. 47, No. 3, 2002, pp. 254–255. Translated from Doklady Akademii Nauk, Vol. 383, No. 3, 2002, pp. 343–345.

MECHANICS

On the Flutter of a Plate

S. D. Algazin* and I. A. Kiĭko**

Presented by Academician D.M. Klimov November 20, 2001

Received November 22, 2001

1. INTRODUCTION

The first systematic investigation of the flutter of a plate dates back to Movchan [1] in 1956. He studied the vibrations and stability of a rectangular plate under the condition that the velocity vector of a flow be parallel to a plate side. For aerodynamic-interaction pressure, the "plunger-theory" formula was used. This special formulation was used in almost all the studies published before the survey [2]. The conventional methods of solving particular problems, for example, the finite-element method or the difference method, being the methods with saturation [3] turned out to be inefficient [4]. The reliability of the frequently used Bubnov–Galerkin method is not definitively clarified as to the plate configuration and the type of boundary conditions; this fact was pointed out in [2]. In the generalized formulation [5, 6], this paper discusses the flutter of a plate with an arbitrary contour given in a parametric form. For this case, we develop the saturation-free method previously proposed in [4]. We present the results of calculations for the rectangular and elliptic plates in the case of an arbitrary direction of the flow-velocity vector.

2. FORMULATION OF THE PROBLEM

Let a plate occupy the region K with the piecewise smooth contour ∂K in the plane xy. A gas flow with the velocity vector $\mathbf{v} = \{v\cos\theta, v\sin\theta\}$, $v = |\mathbf{v}|$, density ρ_0, and pressure p_0 (parameters of a unperturbed state) pass over one side of this plate. As usual, the plate deflections $w(x, y, t)$ are assumed to be $w(x, y, t) = \varphi(x, y)\exp(\omega t)$. In this case, we obtain the eigenvalue problem in the generalized formulation [5, 6]:

$$D\Delta^2\varphi - \beta(\mathbf{v}, \operatorname{grad}\varphi) = \lambda\varphi, \tag{2.1}$$

$$\varphi|_{\partial K} = 0, \tag{2.2}$$

$$L(\varphi)|_{\partial K} = 0. \tag{2.3}$$

Here, D is the torsional rigidity of the plate, $\beta = \dfrac{kp_0}{c_0}$, $c_0^2 = \dfrac{kp_0}{\rho_0}$, k is the polytropic index, and L is the differential operator known from the theory of plates. The parameter λ is related to the vibration frequency by the expression $\rho h\omega^2 + \beta\omega + \lambda = 0$, where ρ and h are the density of the plate and its thickness, respectively.

The plate vibrations are stable and unstable when $\operatorname{Re}\omega > 0$ and $\operatorname{Re}\omega < 0$, respectively. The boundary between these regions in the complex plane λ is the stability parabola

$$\beta^2\operatorname{Re}\lambda = \rho h(\operatorname{Im}\lambda)^2. \tag{2.4}$$

If all λ values are inside the parabola, the motion is stable; if at least one eigenvalue is outside the parabola, the motion is unstable. It is proven [7] that $\operatorname{Re}\lambda > 0$ for the boundary conditions of fixing and simply supporting, all λ are real for $v = 0$, and certain eigenvalues become complex with increasing v. Therefore, the problem is to find such a v value at a given θ for which a certain the eigennumber first falls on parabola (2.4). This flow velocity v_{cr} is taken as the critical velocity of flutter.

To solve problem (2.1)–(2.3) under condition (2.4), we developed a numerical–analytical method without saturation in two modifications. The first modification [4] is used when the analytical (relatively simple formula-specified) conformal mapping of the region K onto the unity circle is known. Here, this restriction is removed (the second modification): when the contour ∂K of the region is given by parametrical equations, the conformal mapping is constructed numerically according to the procedure described in [8].

The algorithm of solving boundary value problem (2.1)–(2.3) is as follows. Upon the double conversion of the Laplace operator, Eq. (2.1) changes to an integral equation and boundary conditions (2.2) and (2.3) are satisfied exactly and approximately, respectively. For numerical solution, we use the interpolation formula [3] providing the method without saturation. The software package realizing this calculation was reported in [9].

* *Institute for Problems in Mechanics, Russian Academy of Sciences, pr. Vernadskogo 101, Moscow, 117526 Russia*

** *Moscow State University, Vorob'evy gory, Moscow, 119899 Russia*

1028-3358/02/4703-0254$22.00

3. RESULTS OF PARTICULAR CALCULATIONS

In the calculations, we used the following parameter values: $p_0 = 1.0133 \times 10^5$ Pa, $\rho_0 = 1.2928$ kg/m^3, $\mu = 0.33$, $k = 1.4$, $E = 6.867 \times 10^{10}$ Pa, $\rho = 2.7 \times 10^3$ kg/m^3, and relative plate thickness $h = 0.003$ (the ratio of plate thickness to a half-length along the x-axis). The other parameters were made dimensionless, as in [4].

3.1. Rectangular simply-supported plate occupying the region K: $\{|x| \le 1, |y| \le b\}$. Boundary conditions (2.3) have the form

$$\left.\frac{\partial^2\varphi}{\partial x^2}\right|_{|x| = 1} = 0, \quad \left.\frac{\partial^2\varphi}{\partial y^2}\right|_{|y| = b} = 0. \qquad (3.1)$$

Let H be the matrix of the discrete Laplace operator with boundary condition (2.2). In this case, the matrix of the discrete biharmonic operator with boundary condition (3.1) is H^2. This fact enables us to relatively simply perform the discretization of spectral problem (2.1), (2.2), (3.1). This procedure is described in detail in [10]. The results of calculations are presented in the third column of the table (eigenvalue numbers are indicated in parentheses).

3.2. Elliptic simply-supported plate. The contour of the region K is given parametrically by the equations $x = \cos t$ and $y = b\sin t$; the ellipse is inscribed into the rectangle from the above example. The simply-supporting condition requires that the bending moment vanishes; therefore, we have

$$L(\varphi)|_{\partial K} \equiv \frac{\partial^2\varphi}{\partial n^2} + \mu\left(\frac{\partial^2\varphi}{\partial s^2} + \kappa\frac{\partial\varphi}{\partial n}\right)\Bigg|_{\partial K} = 0$$

instead of Eq. (2.3). Here, μ is the Poisson ratio and κ is the curvature. The calculations were carried out using numerical conformal mapping according to the procedure from [8]; the results are presented in the second column of the table. For comparison, the fourth column presents the results calculated for the rectangular plate by the Bubnov–Galerkin method.

4. DISCUSSION OF THE RESULTS

The table demonstrates that the dependence $v_{cr}(\theta)$ is nonmonotonic. First, v_{cr} increases with θ, and this increase is more rapid in the region $\theta \in \left(\frac{\pi}{4}, \frac{3\pi}{8}\right)$. Near the point $\theta = \frac{15\pi}{32}$, $v_{cr}(\theta)$ has a maximum. Finally, v_{cr} decreases slightly when θ approaches $\frac{\pi}{2}$. It is characteristic and very interesting that the plate-motion form is modified near the point $\max v_{cr}$ so that the second eigenvalue first falls onto the stabilization parabola.

Table

θ	Elliptic plate	Rectangular plate	Bubnov–Galerkin method
0	0.4029 (1)	0.3546 (1)	0.3042
$\frac{\pi}{8}$	0.4221 (1)	0.3737 (1)	0.3307
$\frac{\pi}{4}$	0.4868 (1)	0.4346 (1)	–
$\frac{5\pi}{16}$	0.5404 (1)	0.4801 (1)	0.4207
$\frac{3\pi}{8}$	0.6012 (1)	0.5235 (1)	–
$\frac{15\pi}{32}$	0.6124 (2)	0.5275 (2)	0.4022
$\frac{\pi}{2}$	0.6108 (2)	0.5257 (2)	0.4121

The presence of $\max v_{cr}$ near the point $\theta = \frac{15\pi}{32}$ is the so-called effect of stabilization of the plate vibrations against the fluctuations of the flow-velocity direction near the point $\theta = \frac{\pi}{2}$. It should be noted that this effect was previously discovered in the problem of the flutter of an infinite strip.

REFERENCES

1. A. A. Movchan, Prikl. Mat. Mekh. **20**, 231 (1956).
2. Yu. N. Novichkov, Itogi Nauki Tekh., Ser. Mekh. Deform. Tverd. Tela **11**, 67 (1978).
3. K. I. Babenko, *Principles of Numerical Analysis* (Nauka, Moscow, 1986).
4. S. D. Algazin and I. A. Kiĭko, Prikl. Mat. Mekh. **60**, 171 (1997).
5. A. A. Il'yushin and I. A. Kiĭko, Vestn. Mosk. Univ., Ser. 1: Mat., Mekh., No. 4, 40 (1994).
6. A. A. Il'yushin and I. A. Kiĭko, Prikl. Mat. Mekh. **58**, 167 (1994).
7. S. D. Algazin and I. A. Kiĭko, Izv. Akad. Nauk, Mekh. Tverd. Tela, No. 1, 170 (1999).
8. É. P. Kazandzhan, Preprint No. 82, IPM AN SSSR (Inst. of Applied Mathematics, Academy of Sciences of USSR, 1979).
9. S. D. Algazin and I. A. Kiĭko, Preprint No. 684, IPMekh RAN (Inst. of Applied Mechanics, Russian Academy of Sciences, 2001).
10. S. D. Algazin, Zh. Vychisl. Mat. Mat. Fiz. **35**, 400 (1995).

Translated by V. Bukhanov

Doklady Physics, Vol. 47, No. 3, 2002, pp. 256–259. Translated from Doklady Akademii Nauk, Vol. 383, No. 3, 2002, pp. 346–349.

MECHANICS

On Rolling and Sliding of a Cylinder along a Perfectly Plastic Half-Space with Allowance for Contact Friction

R. I. Nepershin

Presented by Academician A.Yu. Ishlinskiĭ November 28, 2001

Received November 29, 2001

Rolling of a rigid cylinder along a viscoelastic half-space was considered in [1, 2]. When a contact arc between the cylinder and a plastic domain is small, the problem of rolling a smooth cylinder along the rigid-plastic half-space was solved in [3] by the small parameter method. In this study, we consider the problem of rolling and sliding a cylinder along the boundary of a perfectly plastic half-space with allowance for contact friction. The limiting values of forces and a contact arc for steady plastic flow are obtained.

Figure 1a shows a steady plastic domain arising in the process of rolling and sliding a cylinder along the boundary of an incompressible perfectly plastic half-space [3]. We assume that the cylinder axis is fixed and the half-space moves with a unit velocity $V = 1$. Along the boundary *OEDB*, the velocity is continuous. In the case of a stationary plastic flow, the boundaries *AB* and *OA* are streamlines, the tangents to which at the points *B* and *O* are directed along the half-space boundary. Therefore, the lower point *O* lies on the half-space boundary $y = 0$.

For a cylinder of a radius *R* rolling with an angular velocity ω without slipping, we have a relationship $\omega R = 1$ at its contact point *O* with the rigid domain. At the other points of the contact arc, the plastic material slides from the point *O* to the point *A* and tangential stresses of friction appear on the contact surface and form a positive moment *M*. This is the case for rolling the cylinder with the sliding it forward along the contact arc. If the angular velocity ω is equal to zero or is so small that the plastic material slides from the point *A* to the point *O* in the entire contact arc, the contact-friction stresses and the moment *M* reverse their signs. This is the case for rolling while sliding at the point *O* or sliding the cylinder backwards without rolling in the contact arc *OA*. If the cylinder is smooth, the plastic domain is independent of ω and is the same for both forward and backward slide.

We measure stresses in the units of double the shear-flow stress, and lengths, in the units of the contact arc *OA*. Stresses and velocities in the plastic domain satisfy hyperbolic equations of the plane plastic flow in the sliding lines ξ and η [4]:

$$\frac{dy}{dx} = \tan\varphi \text{ for } \xi \text{ and } \frac{dy}{dx} = -\cot\varphi \text{ for } \eta, \quad (1)$$

$$d\sigma - d\varphi = 0 \text{ in } \xi, \quad d\sigma + d\varphi = 0 \text{ in } \eta, \quad (2)$$

$$\begin{aligned} dV_\xi - V_\eta d\varphi &= 0 \text{ in } \xi, \\ dV_\eta + V_\xi d\varphi &= 0 \text{ in } \eta, \end{aligned} \quad (3)$$

where σ is the mean stress, φ is the slope angle of the

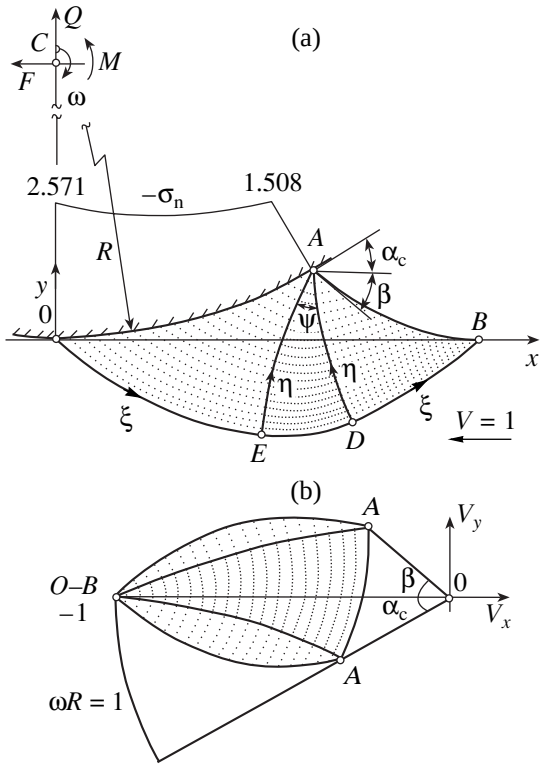

Fig. 1. (a) Field of sliding lines and the normal-pressure distribution at the contact boundary and (b) hodograph of velocities in the process of rolling a cylinder with forward sliding for $\alpha_c = 0.5236$ and $\tau_c = 0.2$ at the point *A*.

Moscow State Academy of Instrumentation Engineering and Informatics, ul. Stromynka 20, Moscow, 107846 Russia

1028-3358/02/4703-0256$22.00

tangent to the sliding line ξ and V_ξ and V_η are the components of the velocity vector in the directions ξ and η.

For a steady plastic flow, the boundary *AB*, which is free of external stresses and coincides with the direction of the second principal stress, is a streamline:

$$\tan\left(\varphi - \frac{\pi}{4}\right) = \frac{V_y}{V_x}, \quad \sigma = -\frac{1}{2} \text{ in } AB, \tag{4}$$

where V_x and V_y are the velocity-vector components related to V_ξ and V_η as

$$V_x = V_\xi \cos\varphi - V_\eta \sin\varphi, \quad V_y = V_\xi \sin\varphi + V_\eta \cos\varphi. \tag{5}$$

Along the rigid plastic boundary *O–B*, velocities are continuous: $V_x = -1$ and $V_y = 0$. From Eqs. (5), we find

$$V_\xi = -\cos\varphi, \quad V_\eta = \sin\varphi \text{ in } O\text{–}B. \tag{6}$$

Since the contact arc *OA* is taken as the characteristic dimension, the cylinder radius *R* and the contact angle α_c are related as $R\alpha_c = 1$. The surface velocity of the cylinder can vary in the range $0 \le \omega R \le 1$. The shear stresses τ_c of contact friction appear at the boundary *OA*, and the sliding lines intersect this boundary at the angle:

$$\theta = \frac{1}{2}\arccos 2\tau_c, \quad 0 \le \tau_c \le \frac{1}{2}. \tag{7}$$

For forward sliding, $\omega R > V_c$, where V_c is the velocity of the material at the contact boundary and θ is the angle between the sliding line η and the tangent to *OA*. For backward sliding, $\omega R < V_c$, the direction of τ_c changes, and θ is the angle between the sliding line ξ and the tangent to *OA*. Therefore, the angle φ specifying the direction of sliding lines with respect to *OA* is determined as

$$\varphi = \alpha + \theta - \frac{\pi}{2} \text{ if } \omega R > V_c \tag{8}$$

for forward sliding or as

$$\varphi = \alpha - \theta \text{ if } \omega R < V_c \tag{9}$$

for backward sliding. For a smooth cylinder, $\tau_c = 0$, it follows from Eq. (7) that $\theta = \frac{\pi}{4}$ and Eqs. (8) and (9) yield the same $\varphi = \alpha - \frac{\pi}{4}$ value at the boundary *OA*.

Since the velocity normal to the cylinder is equal to zero, kinematic boundary conditions at *OA* have the form

$$V_\xi = V_\eta \tan\theta, \quad V_\xi = V_\eta \cot\theta \tag{10}$$

for forward and backward sliding cases, respectively. For a smooth cylinder, Eqs. (10) both yield the equality $V_\xi = V_\eta$.

Thus, for a smooth cylinder, the boundary conditions for stresses and velocities are independent of the direction of the material sliding along the contact boundary *OA*. In this case, the fields of stresses and velocities in the plastic region are independent of the rotation of the cylinder and are the same for forward and backward slides.

The angle ψ of the centered fan of the sliding-line field at the point *A* is determined by the expressions

$$\psi = \frac{3\pi}{4} - (\alpha_c + \beta + \theta) \text{ if } \omega R > V_c \tag{11}$$

for forward sliding or

$$\psi = \frac{\pi}{4} + \theta - (\alpha_c + \beta) \text{ if } \omega R < V_c \tag{12}$$

for backward sliding, where

$$\beta = -\arctan\left(\frac{V_y}{V_x}\right)_A \tag{13}$$

is the slope angle of the tangent to the boundary *AB* at the point *A*.

The mean stress at the point *O* is found from the first of Eqs. (2) for ξ of the sliding line *O–B* and boundary conditions (8) and (9) at $\alpha = 0$:

$$\sigma_0 = -\frac{1}{2}\left(1 + \frac{3\pi}{2}\right) + \theta \tag{14}$$

for forward sliding or

$$\sigma_0 = -\frac{1}{2}\left(1 + \frac{\pi}{2}\right) - \theta \tag{15}$$

for backward sliding, where θ is determined by Eq. (7).

Expression (14) shows that, for forward sliding, the bearing capacity of a rigid wedge at the point *O* is valid if $\tau_c = 0$ $\left(\theta = \frac{\pi}{4}\right)$ at this point. Therefore, the plastic domain shown in Fig. 1a can be formed only if the contact-friction stress varies and equals zero at the point *O*. Experimental data on rolling corroborate that stress vanishes at the point of the outlet of a workpiece from the contact with the roll [5]. In this study, we assume that τ_c varies linearly and is maximal at the point *A*. For backward sliding, the bearing capacity of a rigid wedge at the point *O* is valid for each value of τ_c that is assumed to be constant in *OA*.

The mean value of σ decreases in magnitude along *OA* and, at the point *A*, takes the following value depending on the angle ψ,

$$\sigma_A = -\frac{1}{2}(1 + 2\psi). \tag{16}$$

If the distribution of σ along the contact arc *OA* is known, it is possible to determine the normal pressure

on the cylinder

$$-\sigma_n = -\left(\sigma - \frac{1}{2}\sin 2\theta\right), \quad (17)$$

and the forces and moment with allowance for the relationship $R\alpha_c = 1$ are found in the form

$$Q = \frac{1}{\alpha_c}\int_0^{\alpha_c}[(-\sigma_n)\cos\alpha \pm \tau_c \sin\alpha]d\alpha, \quad (18)$$

$$F = \frac{1}{\alpha_c}\int_0^{\alpha_c}[(-\sigma_n)\sin\alpha \mp \tau_c \cos\alpha]d\alpha, \quad (19)$$

$$M = \pm\frac{1}{\alpha_c}\int_0^{\alpha_c}\tau_c d\alpha, \quad (20)$$

where the upper and lower signs correspond to the forward and backward sliding cases, respectively, and

$$-\sigma_n = -\left(\sigma - \frac{1}{2}\right) \text{ and } M = \tau_c = 0$$

for a smooth cylinder.

For a rough cylinder and linearly varying τ_c, Eq. (20) yields $M = \frac{1}{2}(\tau_c)_A$ and $-\tau_c$ for forward and backward sliding cases, respectively.

The above equations show that the problem of rolling and sliding a cylinder calls for the joint consideration of stress and velocity fields. The solution to the problem can be found by the following way.

Taking into account known values (14) and (15) at the point *O*, we set a continuous distribution of σ at the boundary *OA* and an initial approximation for the angle β. Then, σ and the boundary conditions (8) and (9) define the Cauchy data for Eqs. (1) and (2) and the field of sliding lines in the domain *OAE*. In the domain *AED*, the field of sliding lines is found by solving the Goursat problem with given σ and φ in *AE* and at the singular point *A* with the angle ψ specified by Eqs. (11) and (12). In the domain *ABD*, we solve the inverse Cauchy problem with given σ and φ in *AD* and conditions

$$\sigma = -\frac{1}{2}, \quad \frac{dy}{dx} = \tan\left(\varphi - \frac{\pi}{4}\right)$$

at the unknown boundary *AB*. As a result, we find the free boundary *AB* and the rigid plastic boundary *O–B*. Next, we find the field of velocities in the plastic domain by solving the mixed boundary value problem for Eqs. (3) with boundary conditions (6) and (10). If steady-flow condition (4) is satisfied at the boundary *AB*, the distribution of σ over *OA* is the solution to the problem. Since the sequence of solving the boundary value problems for Eqs. (1)–(3) determines the field of sliding lines with the boundary *AB* and the velocity field dependent on the distribution of σ over *OA*, Eq. (4) is the determining equation for the unknown distribution of σ over *OA*.

The fields of sliding lines and velocities for a given distribution of σ over the boundary *OA* were calculated numerically by using a finite-difference approximation of differential equations (1)–(3). The boundary *AB* free of external stresses is obtained by solving the sequence of the elementary inverse Cauchy problems starting worth the an initial point *A*. The coordinates of these boundary points are found from the differential equation of the *AB* contour $\frac{dy}{dx} = \tan\left(\varphi - \frac{\pi}{4}\right)$ and differential equation (1) for the ξ-line. The velocities at the boundary *OA* are obtained by solving the elementary mixed problems for differential equation (3) along the η-line with allowance for boundary conditions (10). Since differential equations (2) and (3) are linear, the finite-difference equations are also linear. For this reason, the calculation of a detailed network of sliding lines and the field of velocities for a σ distribution given at 20 nodes at the boundary *OA* takes a fraction of a second on a Pentium-133 computer.

Let $\boldsymbol{\sigma}$ be the vector of unknown σ values at the *N* nodes at the boundary *OA* and $\mathbf{f}$ be the vector of the differences between the slope angles of tangents to the boundary *AB* and velocity vector at the *N* nodes of this boundary. These differences are the errors of stationary condition (4) for given $\boldsymbol{\sigma}$. The procedure of computing the fields of sliding lines and velocities provides a continuous $\mathbf{f}$–$\boldsymbol{\sigma}$ dependence, and condition (4) takes the form of the *N*-dimensional nonlinear vector equation

$$\mathbf{f}(\boldsymbol{\sigma}) = \mathbf{0}. \quad (21)$$

Equation (21) is solved by the Broyden method [6], in which the iterative process does not require the evaluation of derivatives. Taking the initial approximation for the angle β, we specify the initial approximation $\boldsymbol{\sigma}^0$ by a linear distribution over *OA* from the value specified by Eqs. (14) and (15) at the point *O* to value (16) at the point *A*. The functional matrix $\frac{\partial \mathbf{f}_i}{\partial \boldsymbol{\sigma}_j}$ at the initial point $\boldsymbol{\sigma}^0$ is found via solving *N* problems for the variations of $\boldsymbol{\sigma}^0$ by the finite-difference method. Equation (21) is solved in several iterations with an accuracy of $|f_i|_{\max} \le 10^{-4}$, $i = 1, 2, \ldots, N$. The condition $y = 0$ at the point *B* is satisfied with an accuracy of 10^{-6}.

Figure 1 shows (a) the field of sliding lines with distribution of the contact pressure and (b) the hodograph of velocities for rolling a rough cylinder without slippage at the point *O* ($\omega R = 1$) for the contact angle $\alpha_c = 0.5236$ for forward sliding with the maximum value $\tau_c = 0.2$ at the point *A*. For this case, we obtain $\beta = 0.703$, $\psi = 0.55$, $Q = 2.03$, $F = 0.394$, and $M = 0.1$. With increasing the contact angle α_c, the centered-fan angle ψ vanishes, the domain *AED* in the physical plane contracts to a line, the velocity at the singular point *A*

becomes single-valued, and the corresponding arc *A*–*A* at the hodograph of velocities tends to the fixed point *O*. Thus, along the free boundary *AB*, the velocity of a material particle decreases from 1 at the point *B* to 0 at the point *A* when $\psi \longrightarrow 0$ Then, the velocity increases from 0 to 1 when the particle moves along the cylinder boundary from the point *A* to the point *O*. For $\tau_c = 0.2$, we find the ultimate contact angle $\alpha_c^* = 0.65$ at which a steady plastic flow with the forces $Q = 1.828$ and $F = 0.427$ is possible. An increase in friction for forward sliding leads to increasing both the angle ψ and the ultimate contact angle α_c^* as $\psi \longrightarrow 0$.

The ratio $\frac{F}{Q}$ can be treated as the coefficient of rolling friction caused by the asymmetry of the plastic domain about the *y*-axis coinciding with the axis of the cylinder. In the case of forward sliding for given τ_c values, it is possible to find the contact angles α_c for which the force $F = 0$. This is the limiting case of rolling a thick workpiece without penetrating plastic deformations into its depth; i.e., when only the surface layer is plastically deformed.

Figure 2 shows (a) the field of sliding lines with the contact-pressure distribution and (b) the hodograph of velocities for rolling and sliding a cylinder with backward sliding at the contact boundary *OA* for $\alpha_c = 0.2$ and $0 \le \omega R < 0.59$ and the contact-friction stress $\tau_c = 0.2$. In this case, we have $\beta = 0.364$, $\psi = 0.801$, $Q = 2.03$, $F = 0.39$, and $M = -0.2$. An increase in friction for backward sliding leads to decreasing the angle ψ, a limiting contact angle α_c^*, and normal pressure on the cylinder. Moreover, this pressure is distributed more uniformly than pressure for rolling the cylinder with forward sliding.

At $\omega = 0$, we obtain the sliding of a round die ahead of which a steady plastic domain depending on the vertical force *Q* and the contact friction τ_c is formed. This problem also describes the process of drawing a thick workpiece between circular matrices when only the surface layer undergoes plastic deformation. As $\tau_c \longrightarrow 0.5$ (for backward sliding), $\alpha_c \longrightarrow 0$ vanishes, the plastic region *ABDE* degenerates into the point *A*, and the domain *OAE* degenerates into a shear line with the uniform pressure $-\sigma_n = 0.5 + \frac{\pi}{4}$ at the boundary *OA*. This is the case of sliding an absolutely rough plane die along the boundary of a plastic half-space.

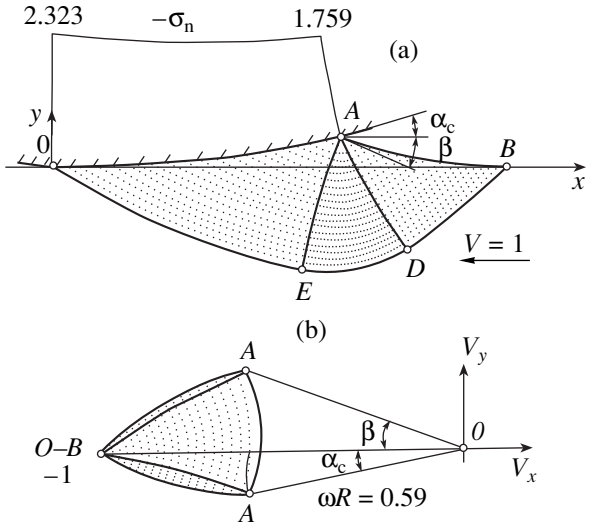

Fig. 2. The same as in Fig. 1, but for the process of rolling a cylinder with backward sliding for $\alpha_c = 0.2$ and $\tau_c = 0.2$.

REFERENCES

1. A. Yu. Ishlinskiĭ, Prikl. Mat. Mekh. **3**, 245 (1939).
2. A. Yu. Ishlinskiĭ, *Applied Problems of Mechanics*, Vol. 1: *Mechanics of Viscoplastic and Elastic Solids* (Nauka, Moscow, 1986).
3. E. A. Marshall, J. Mech. Phys. Solids **16**, 243 (1968).
4. D. D. Ivlev, *Theory of Ideal Plasticity* (Nauka, Moscow, 1966).
5. A. I. Tselikov, *Foundations of Rolling Theory* (Metallurgiya, Moscow, 1965).
6. J. E. Dennis and R. B. Shnabel, *Numerical Methods for Unconstrained Optimization and Nonlinear Equations* (Prentice-Hall, Englewood Cliffs, N. J., 1983; Mir, Moscow, 1988).

Translated by Yu. Vishnyakov